INSCRIPTION OF LARGE APERTURE CIRCULAR GRATINGS AND THE SURFACE PLASMON RESONANCE RESPONSE IN THE OPTICAL REGIME

A study on polarization dependence of Surface Plasmon coupling over small curvature circular gratings

INSCRIPTION DE RÉSEAUX CIRCULAIRES À GRANDE OUVERTURE ET RÉPONSE À LA RÉSONANCE PLASMONIQUE DE SURFACE DANS LE RÉGIME OPTIQUE

Étude de la dépendance de la polarisation du couplage des plasmons de surface sur des réseaux circulaires à faible courbure

A Thesis Submitted to the Division of Graduate Studies
of the Royal Military College of Canada
by

Eoin Dawson, BSc

In Partial Fulfillment of the Requirements for the Degree of
Master of Science in Physics
March, 2024

Acknowledgements

I would like to give my thanks to Dr. Ribal Georges Sabat and the research team at RMC for always accepting me as a member of the team even when I wasn't a great teammate. Specifically, to Dr. Ribal Georges Sabat, thank you for your undying patience towards me, to see this project through; to Dr. Mahyar Mazloumi for embracing me as a collaborative author and for setting a great example as a professional researcher; to Mr. Peter Snell for his technical mastery, for without his work in manufacturing of the CDGs and various optical elements/fixtures none of this work could have been done; to Dr. Paul Rochon for our brief but inciteful discussions; to Justin Macdonald for his help with the odd fixture; and to Jamie Leibold and our discussions about his previous work.

An endless appreciation for my mother and brother, Terry Mitten-Dawson and Luke Madsen, for the encouragement when it was needed most. Thanks to all my family who were brave enough to ask questions about my Nano-Thesis, and bold enough to ask for a name drop. To all my friends who had more belief in me than I could ever attain by myself, you are the true heroes.

Abstract

Interference lithography was used on an Azo-Glass thin film to inscribe large aperture circular surface relief gratings, with groove depth (50-70 nm) and pitch varied among three pitch values, for use in surface plasmon resonance coupling and intensity transmission measurements. A theory exploiting the rotational symmetry of a circular grating's-grating vector and its relationship to the coupling requirement of the surface plasmon mode; by separating the coupling and non-coupling components of the field and assuming complete suppression over the non-coupling component, an intensity profile of the coupling field can be resolved. Normalized transmission spectrums were measured with linear and 'unpolarized' light sources, with amplification factors ranging from (1.8-3.6) and (2.3-4.2) respectively. Potential lensing effects were observed under a linearly polarized beam with a diameter matched aperture. Under full illumination, the gratings' surface plasmon response was $\sim$43% of the amplification as was under 'half-illumination' along the direction of polarization. We are led to hypothesize a destructive interference of the counter propagating SPR modes under linear polarization.

Résumé

La lithographie par interférence a été utilisée sur un film mince d'Azo-Glass pour inscrire des réseaux circulaires à relief de surface à grande ouverture, avec une profondeur de rainure (50-70 nm) et un pas variant entre trois valeurs de pas, pour une utilisation dans les mesures de couplage de résonance plasmonique de surface et de transmission d'intensité. Une théorie exploitant la symétrie de rotation du vecteur de réseau d'un réseau circulaire et sa relation avec l'exigence de couplage du mode de plasmon de surface ; en séparant les composantes de couplage et de non-couplage du champ et en supposant une suppression complète de la composante de non-couplage, un profil d'intensité du champ de couplage peut être résolu. Les spectres de transmission normalisés ont été mesurés avec des sources lumineuses linéaires et non polarisées, avec des facteurs d'amplification allant respectivement de (1,8-3,6) et (2,3-4,2). Des effets de lentille potentiels ont été observés sous un faisceau polarisé linéairement avec une ouverture de diamètre adapté. Sous pleine illumination, la réponse plasmonique de surface des réseaux était $\sim$43% de l'amplification comme c'était le cas sous "demi-illumination" le long de la direction de polarisation. Nous sommes amenés à émettre l'hypothèse d'une interférence destructive des modes SPR se propageant en sens inverse sous polarisation linéaire.

Contents

List of Tables

List of Figures

List of Acronyms

SPP	Surface Plasmon Polariton
SP	Surface Plasmon
EM	Electromagnetic
TM	Transverse magnetic
TE	Transverse electric
SPW	Surface Plasma Wave
TIR	Total internal reflection
LSPP	Localized Surface Plasmon Polariton
SRG	Surface relief grating
SOP	State of Polarization
CVB	Cylindrical vector beam
LP	Linear polarizer
TNLC	Twisted nematic liquid crystal
LC	Liquid crystal
CG	Circular grating
RCWA	Rigourous Coupled Wave Analysis
PDE	Partial Differential Equation
HG	Hermite-Gaussian
LG	Laguerre-Gaussian
BG	Bessel-Gaussian
OAM	Orbital angular momentum
SAM	Spin angular momentum
HOPS	Higher-Order Poincaré Spheres
CDG	Circular diffraction grating generator
SPR	Suface Plasmon Resonance
GV	Grating vector
LCTF	Liquid Crystal Tunable Filter
RPC	Radial Polarization Converter
TN	Twisted nematic
FFT	Fast fourier transform
AFM	Atomic Force Microscope
RHCP	Right Handed Circular Polarization

List of Symbols

Greek Symbols

Symbol	Description	Definition (units)
α	Auxilliary angle of the ratio of max field amplitudes in a set projection	
γ	Frequency of collisions	(s^{-1}/Hz)
δ	A phase difference of two interfering light rays	
ϵ	Dielectric permittivity of a material	($F \cdot m^{-1}$)
ϵ_0	Dielectric permittivity of free space	$\sim 8.854 \times 10^{-12} F \cdot m^{-1}$
ϵ_r	Relative permittivity of a material	$\frac{\epsilon}{\epsilon_0}$
ϵ'	Mathematically real part of the electric permittivity of a material	
ϵ"	Mathematically imaginary part of the electric permittivity of a material	
$\epsilon_{(m,d)}$	Electric permittivity of a metal(m) and dielectric(d) material	
θ_m	The angle of diffraction for the m-th mode under coherent monochromatic light	
θ_i	The angle of incidence of beam with respect to the sample normal	

Symbol	Description	Definition (units)
θ_{cdg}	Nominal angle of the 'Circular Diffraction Grating Generator (CDG)'	(degrees)
θ	Rotation of physical polarizer away from the vertical axis	(degrees)
λ, λ_I	Wavelength of light, Laser inscription wavelength	(nm), (488nm,510nm,532nm)
λ_{SP}	Surface plasmon wavelength	(nm)
λ_{SP}	Surface plasmon wavelength	(nm)
μ	Magnetic permeabililty of a material	($\mathrm{N{\cdot}A^{-2}}$)
μ_0	Magnetic permeabilility of free space	$\sim 1.257 \times 10^{-6}$ $\mathrm{N{\cdot}A^{-2}}$
ν	Frequency of light	($\mathrm{s^{-1}}$)
ξ	Ray angle with respect to the x-axis	(radians/degrees)
ρ_f	Free charge density	($\mathrm{C{\cdot}m^{-3}}$)
σ	Conductivity of a material	$\mathrm{S{\cdot}m^{-}}1$
τ	Condensed field argument	
τ_c	Characterstic collision time of electrons in a general conducting media	
ϕ	Phase difference of orthogonal field components	
χ_e	Electric susceptibility tensor	
ψ	Auxillary angle of the ratio of the two ellipse axes	

Symbol	Description	Definition (units)
ω	Angular frequency of light	(radians$\cdot$s^{-1})
ω_p	Plasmon frequency in a general conducting media	
∇	The gradient vector from Multivariable Calculus	$[\frac{\partial}{\partial x}, \frac{\partial}{\partial y}, \frac{\partial}{\partial z}]$
Λ	Grating pitch	(nm)

Roman Symbols

Symbol	Description	Definition (units)
c	Speed of light	$\sim 3 \times 10^8$ m/s
E	Electric field vector	
H	Auxilliary Magnetic vector	
k	Wavenumber	$k_{vacuum}=\frac{2\pi}{\lambda}(m^{-1})$
r	Position vector	$[r_x,r_y,r_z]$
n	refractive index of a material	
S	Stokes polarization vector	$[S_0,S_1,S_2,S_3]$
i	The imaginary unit	$i=\sqrt{-1}$
P	Polarizablity Tensor	
K	Grating wavenumber	$\frac{2\pi}{\Lambda}$
$\mathbf{K}_G$	Grating wavevector	$[K_r,K_\theta]$
I	Irradiance	$(W\cdot m^{-2})$
s	Poynting vector (energy flux density)	$(W\cdot m^{-2})$

Additional Notation

Symbol	Description
A	Scalar
$\mathbf{A}$	Vector
$\tilde{\mathbf{A}}$	Complex vector
$\bar{\mathbf{A}}$	Complex valued matrix
$\hat{\mathbf{A}}$	Unit vector
$A_{(x,y,z)}$	(x,y,z) - component of the vector $\mathbf{A}$
$A_{(r,\theta)}$	(r,θ) - component of the vector $\mathbf{A}$ with resepct to a defined origin
A'	Real value of A
A"	Imaginary vaule of A
A_d	Value of A in a dielectric
A_m	Value of A in a metal
$\langle A \rangle$	Time-averaged value of A

1 Introduction

A Surface Plasmon Polariton (SPP) is a quasiparticle produced by coupling a Photon (Electromagnetic Wave) and a Surface Plasmon (SP) mode at a dielectric-metal interface[1]. The SP mode's Electromagnetic (EM) field is periodic on the surface and evanescent normal to the surface[2]. The SP mode is produced by a charge density oscillation at the dielectric-metal interface, specifically in the form of the conducting electrons in the active media [2]. In a classical approach, the conducting electrons form a free electron gas inducing a polarization of the incident EM wave, coupling the photon with the free charge in the active media, creating a SPP.

1.1 Historical Context

At the turn of the 20th century, R.W.Wood measured the spectrum of an 'anomalous diffraction grating', producing unexpectedely high monochromatic intensity in the first order diffraction spectra as seen in Fig. 1.1 [3]. Wood discovered that the incident polarization of light determined the presence of the anomalous diffraction spectrum, where the maximum intensity occured when the electric field was orthogonal to the grating grooves (Transverse Magnetic) and minimum when parallel (Transverse Electric). Rayleigh first attempted a theoretical description of the diffraction anomalies, approaching the problem with the tool of Hyugen's wave propagation principle. Rayleigh hypothesized the 'passing off' of the tangential momentum of a diffraction order from a groove constructively interfering with the orders of the next groove, occuring at a singular wavelength dependent on the groove period [4]. Rayleigh's interpretation was not the direct cause of the anomalous spectrum seen by Wood. The first accurate interpretation of Wood's results came in 1941 when Fano first described 'Quasi-Stationary Waves' on the surface of a grating, arising from the sign change in the discontinuity of the refractive index of the dielectric and the metal grating[5]. The 'Quasi-Stationary Waves' have since been termed as Surface Plasma Waves (SPW) [6][7] and colloquially referred to as SPPs today.

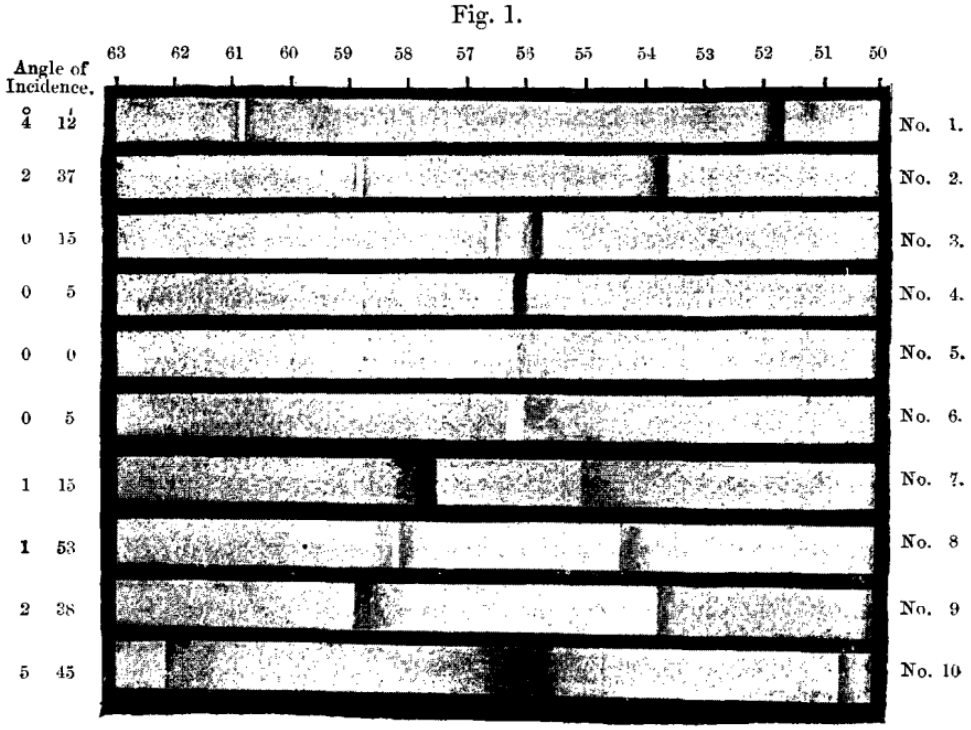

Figure 1.1: Sourced figure from Wood's seminal discovery with spectra of the first order reflection diffraction mode of a ruled grating at various angles of incidence[3]

1.2 Methods of SPP Excitation

Light (with frequency less than the plasma frequency: $\omega < \omega_p$) directed onto a surface capable of supporting a SP, with a negative real component of the dielectric permittivity, always has a momentum vector smaller than the SP mode. Hence, radiative modes need a momentum boost at the surface to allow for phase matching and coupling[1].

There are two distinct methods in which SPPs have been excited: total internal reflection (TIR) and diffraction, each with various geometries involved.

The Otto and Kretschmann methods utilize the evanescent fields that occur under TIR in a prism, where photons capable of tunneling from the reflected beam couple into an SPP on the metal surface adjacent to the TIR [6][7]. Otto confirmed non-radiative modes by measuring the reflectivity at various angles of incidences and wavelengths of light, where the configuration used an air gap between the prism and metal surface. The Kretschmann configuration utilizes a thin metal layer in direct contact with the plane of reflection as seen in Fig. 1.2, however the metal thickness needs to be controlled, allowing penetration of the SP fields

through the metal while also providing a sufficient bulk media for coupling[8].

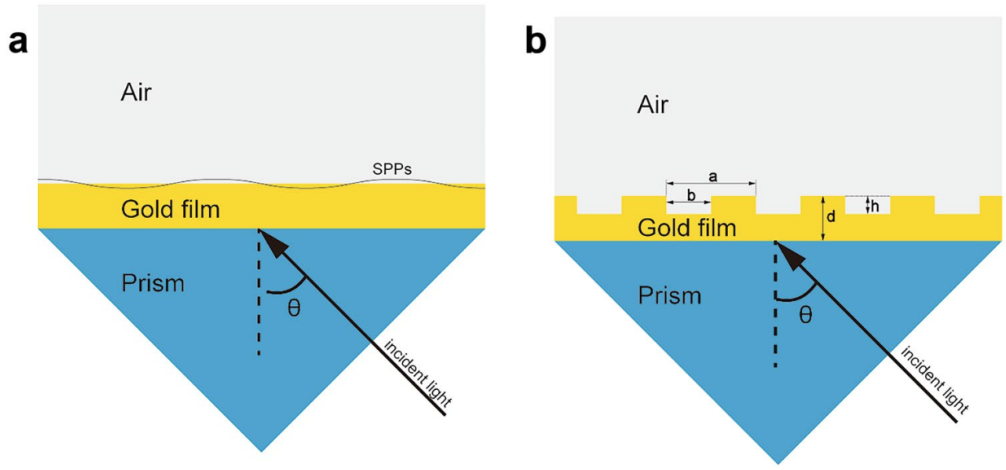

Figure 1.2: Sourced figure showing diagrams of a classic Kretschmann configuration (a) and a hybrid grating configuration (b)[9]

The second of the methods, is the excitation by diffraction at the dielectric-metal surface[10]. The diffraction of a wave creates evanescent modes with identical temporal frequency as the incident light with increased momentum. Diffraction of the waves can be caused by various surface features. Early experiments on thin films of metal found plasma resonance absorption via a surface plasmon mode [11] where the radiation was observed in only two directions from the incident plane wave(Transmitted and Reflected). Theoretical work later hypothesized that the observed scattered radiation at the plasma frequency was caused by a small amount of surface roughness, inducing surface currents characterized by small dipole producing surface currents [12]. The use of dipoles for currents were also used much earlier to describe Mie's solutions to Maxwell's equations around a spherical metallic particle in an oscillating electric field[13]. Mie's solutions lead to conditions to excite Localized Surface Plasmon Polaritons (LSPPs) within metallic particles. Enhanced transmission was first observed by Kelly and collaborators[14]. In general, it's been found that subwavelength holes or protrusions on a metallic film will allow for the coupling to an SP mode[15].

Counter to the LSPP in metallic nanoparticles and the stationary nature of the quasi-particle, a propagating SPP can be created with incident light on a diffraction grating of appropriate periodicity and depth[16]. One of the more important features a diffraction grating has over the previous methods is the ability to both efficiently couple to the SP mode, and reversely couple the SP mode into the radiative mode for enhanced transmission at the coupling wavelength[17][18].

1.3 Azopolymer Photo-Interference Lithography

Fabrication of nanostructured surfaces with amorphous azopolymer films has been of significant interest. The photo-isomerization reaction between the *trans-* and *cis-* forms of the chemical structure as depicted in Fig. **??**, and the coperative molecular motions within the polymer structure relative to the incident field polarization give rise to mesoscopic and macroscopic molecular motion respectively. Azopolymers have been used to fabricate novel photonic elements by utilizing the movement associated with the photo-isomerization, including tunable diffractive surfaces [19] polarization splitting bifocal lenses[20], polarization sensing films [21], and plasmonic sensing devices [22].

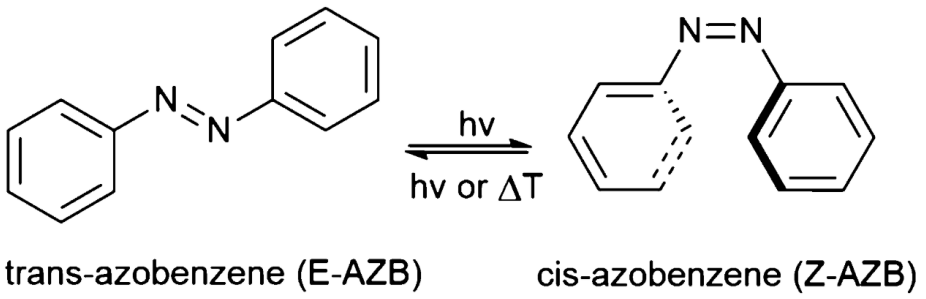

Figure 1.3: Sourced figure depciting the chemical structure of the two azobenzen isomers [23]

In particular, an azopolymer film under a laser interference pattern of suitable incident wavelength, first observed by Rochon and Natansohn[24], form surface relief gratings (SRGs) that are polarization and intensity dependent [25]. The dominant source of the molecular processes inscribing the SRGs are still not agreed upon, however the fabrication of many complex surfaces using the interference lithographic technique have been used in creating diffractive and plasmonic devices[26][27][28][29][30].

1.4 Cylindrical Vector Beams and Generating Methods

For centuries the process of polarizing light came in the form of isolating vectoral components of an incident light source via TIR and birefringence, an impassable optical element such as a wire grid, or simply polarization by means of scattering. These methods produce a spatially homogenous state of polarization (SOP), in

which the surface of constant phase is the transverse plane. This plane wave solution is the most trivial to the Helmholtz's equation.

There are more complex modes of a paraxial beam, one which possess a rotational symmetry around the axis of propagation, a spatially inhomogenous SOP[31]. The Laguerre-Gaussian and Bessel-Gaussian modes are called Cylindrical Vector Beams (CVB's) because of their polarization symmetry around the center. The angular symmetry of polarization in the CVBs are a product of a helical phase wave front centered around a phase singularity[31][32]. Interest in CVBs has been revitalized due to many of their attributes, such as the non-vanishing longitudinal electric and magnetic fields under tight-focusing, in the radially and azimuthally polarized beams respectively. The former allows focusing beyond the diffraction limit[33] and has been used in machining processes[34], plasmonic focusing[35], and molecular orientation measurements[36] among other things. The degrees of accessible polarization modes in the class of CVBs is also of great interest in the communications field[37], where metasurfaces have recently been utilized to multiplex/demultiplex CVB modes with high transmission rates[38].

There are two approaches when generating CVBs – active and passive. Active generating methods of CVBs involve intracavity devices of the laser, such as using an axial birefringent component as done first by D.Pohl[39], and later improved on when interest in CVBs was renewed[40]. Other methods such as a circular multilayer-polarizing grating end mirrors were used to actively generate CVBs[41]. Higher order CVBs have been also generated using uniaxial crystals[42].

Passive methods for generating CVBs make use of the interrelation of the phase and the polarization of the light passing through the conversion component, such as using multiple spatial light modulators [43][44], binary multi-sector phase plates[45], and q-plates[46]; or interferomeric techniques external to the laser cavity [47][48]. As seen in Fig. 1.4, a segmented q-plate with variable retardances were used in an optical system to generate various CVBs; analysing the intensity distributions using a back linear polarizer (LP) at varying angles.

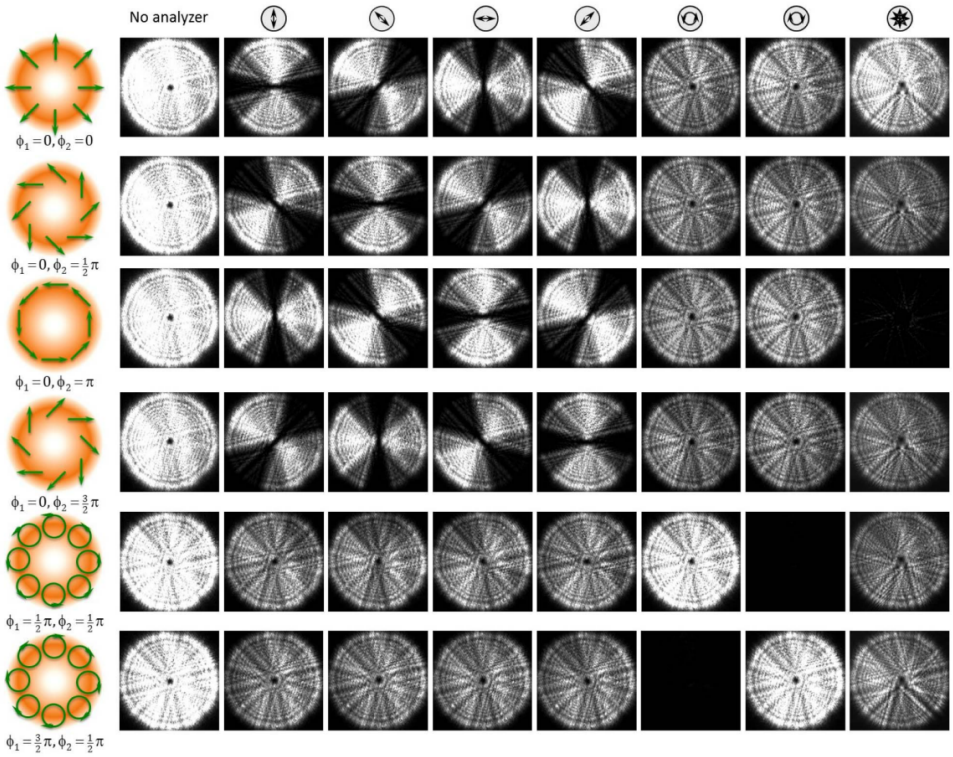

Figure 1.4: Sourced figure showing the transmission profile through a q-plate, using a linear polarizer as an analyzer with varying polarizing angles at the top of the figure[46]

Twisted Nematic Liquid Crystals (TNLC) have been used as a method in creating CVBs. When a nematic LC is fixed in a twisted state, applying a voltage across the dielectric ends drives a re-orientation along the twisting axis, varying transmissive properties through the LC[49]. With precise rubbing in the fabrication process of the TLNC, the potential of these devices to convert axially symmetric polarizations of different orders has been discussed[50]. A TNLC can continuously convert a linear polarized beam into an axially symmetric polarized state corresponding to the geometric twisting of the LCs. This has been demonstrated both in lab[51][52], and as a market device[53]. The TLNC devices differ from q-plates, by the continuous partioning of the linear retardance gradient, where as in the q-plates shown in Fig. 1.4, the discrete partitioning is easily seen.

1.5 Surface Plasmon Polaritons and Polarization

The polarization of a field is an important characteristic of any EM field, providing information about the emitting source, if observed directly, or the media in which

the field is travelling through by some polarization conversion. The coupling relationship between an SPP and the incident field corresponds to the geometry and method of the coupling surface[1]. In the case of prism coupling there is a singular transverse polarization which excites the SPP mode, whereas in the LSPP configurations the Mie resonances can occur along multiple axes of transverse polarizations due to the symmetries of the particles involved in coupling[13][54]. Similarly, an SPP only couples via a grating if the projection of the polarized field along the grating vector is nonzero[1]. The relationship between the polarization of an incident field and the generation, characteristics and applications of the excitation of the corresponding SPPs is an active area of research[55][56][57][58].

Phase gratings such as those manufactured using the photo-interference methods creating SRGs have been used to create cross gratings[59], fourier SRG structures for plasmonic images[60], and non linear gratings[61][62][63]. The polarization conversion of the incident light induced by cross gratings is not fundamentally understood, but has been observed to create high sensitivity plasmonic sensors used for bio-detection of E-Coli[28] and refractive index changes[64]. Nonlinear 2-dimensional gratings with a nano-aperture have been studied as plasmonic devices and have been found to be similar in the transmission spectra of analogous linear gratings; up to a blueshift caused by LSPPs excited by defects in the aperture[65].

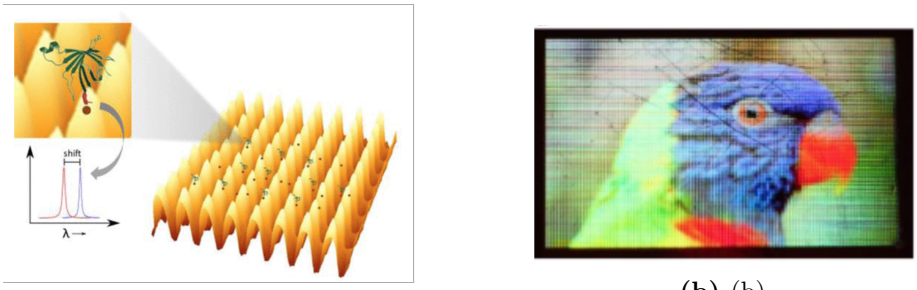

(a) (a)

(b) (b)

Figure 1.5: (a) Diagram of cross grating with surface organelle substrate molecules and the measurable resonance shift in the spectrum from a change in the refractive index [28] (b)Image produced from an SPR irradiation on a Fourier inscribed gratings using interference lithography[60]

Curved concentric gratings with varying symmetries as seen in Fig. 1.6, have been observed as plasmonic lenses for linearly polarized light[66]. It is important to note that the double-sided curved gratings seen in Fig. 1.6 were purposely simulated to have the ridges of one side of the grating line up with the grooves of the other (asymmetry). The result of directing linearly polarized light at these asymmetrical grating structure was an intense region in the center of the structure. Without this asymmetry the fields from the two curved gratings would have de-

structively interfered[66]. Moreover, non-linear grating structures have also acted as radial/azimuthal polarizers[67].

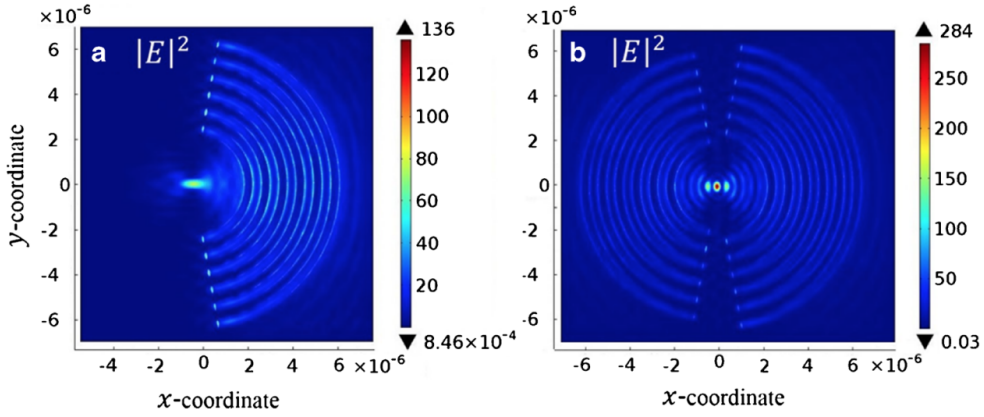

Figure 1.6: Sourced figure showing the simulation of the intensity of single curved grating (left) and an assymetric double-sided curved grating(right) [66]

1.6 Thesis Statement

1.6.1 Interface

The goal of this project is to utilize interference lithography to inscribe large aperture circular SRGs, for observation of the surface plasmon resonance and its dependency on the polarization of the coupling radiation. The properties of a non-linear grating's coupling ability to an SP mode is studied, and its similarities to a linear grating is contrasted. Moreover, the wavelength dependent SPR polarization conversion holds for circular gratings. Finally the field enhancement from the SPR response on circular gratings under radially polarized light is observed.

1.7 Thesis Structure

This Thesis will introduce the theory, needed for a thorough understanding of the following discussion in Chapter 2. This will include a discussion on the primary principles of EM, polarization and SP theory, followed by an approximation of the field SP transmission through a large aperture circular grating. Chapter 3 will discuss the experimental setups, measurement and software tools used throughout the project. Chapter 4 will contain and discuss the results of the experiments, including the observation of the SPR transmission signal and polarization conversion through a cross polarizer setup. The conclusion in Chapter 5 will summarize the results, and discuss future work understanding the limits of

interference lithography under non-linear inscription environments, exictations of SP fields on large aperture circular gratings and their responsiveness to varying incident polarizations.

2 Theory

In this chapter a mathematical framework is introduced to cover EM theory from which a novel SPR intensity-mapping theory will be presented to analyze and discuss the experimental results.

The discussion will begin with an overview of Maxwell's equations, the existence of EM waves, and their polarization properties. Following the fundamentals of EM waves, the inscription of EM gratings using interference on a photoreactive azopolymer film will be outlined, along with the classical Drude theory of metals and the necessary parameters required for the existence of a SP mode. Additionally, the excitation of a SPP via the coupling of photons and the SP mode on the inscribed metallic-layered SRG and the corresponding field polarization is presented. Subsequently, an intensity mapping of the SPR field on the circular grating (CG) is hypothesized and further explored under varying polarization environments. Lastly, the rigorous coupled wave analysis (RCWA) algorithm is introduced for completeness in justifying simulation results for various gratings.

For the remainder of this chapter, bold cased lettering describes a vector and additionally , $\tilde{\mathbf{X}}$, represents a complex valued vector. $\bar{\mathbf{X}}$ will represent a matrix, and scalars will have standard cased font.

2.1 Light as EM Waves

Maxwell's equations, originally written as a set of integral equalities, were highly criticised for their abstract nature and ill-practical use. However, they have been shown to have great use in theoretical and experimental sectors of science and remain a standard of theoretical physics[68]. The following section will explore the derivation of EM waves and their properties applied throughout this thesis.

2.1.1 Maxwell's Equations in Generality

The differential form of Maxwell's equations shown below are obtained through the use of Gauss's divergence and Stoke's Theorem[68]:

$$\nabla \cdot \mathbf{E} = \frac{\rho_f}{\epsilon} \tag{2.1.1}$$

$$\nabla \cdot \mathbf{H} = 0 \tag{2.1.2}$$

$$\nabla \times \mathbf{E} = -\mu \frac{\partial \mathbf{H}}{\partial t} \tag{2.1.3}$$

$$\nabla \times \mathbf{H} = \mathbf{J}_f + \epsilon \frac{\partial \mathbf{E}}{\partial t} \tag{2.1.4}$$

where $\mathbf{E}$ is the electric vector field, $\mathbf{H}$ is the vector magnetic field, and ρ_f and $\mathbf{J}_f$ are the total free charge and current density respectively, both reducing to zero in a vacuum. ϵ is the electric permittivity, $\omega = 2\pi\nu$, where ν is simply the frequency of the electric field with unit s^{-1}. This function reduces to the constant electric permittivity of free space (ϵ_0) in a vacuum. For the remainder of the thesis, only non-magnetic materials will be considered with the permeability of free space $\mu = \mu_0$.

2.1.2 EM Waves in a Vacuum

Maxwell's equations in a vacuum reduce to Eq.'s 2.1.5 - 2.1.8:

$$\nabla \cdot \mathbf{E} = 0 \tag{2.1.5}$$

$$\nabla \cdot \mathbf{H} = 0 \tag{2.1.6}$$

$$\nabla \times \mathbf{E} = -\mu_0 \frac{\partial \mathbf{H}}{\partial t} \tag{2.1.7}$$

$$\nabla \times \mathbf{H} = \epsilon_0 \frac{\partial \mathbf{E}}{\partial t} \tag{2.1.8}$$

Taking the curl of both Eq. 2.1.7 and Eq.2.1.8, and substituting Eq. 2.1.5 and Eq. 2.1.6 into the operator identity $\nabla \times (\nabla \times) = \nabla(\nabla \cdot) - \nabla^2$:

$$\nabla^2 \mathbf{E} = \mu_0 \epsilon_0 \frac{\partial^2 \mathbf{E}}{\partial t^2}, \quad \nabla^2 \mathbf{H} = \mu_0 \epsilon_0 \frac{\partial^2 \mathbf{H}}{\partial t^2} \tag{2.1.9}$$

A set of partial differential equations (PDEs) is found in Eq. 2.1.9, only considering the 'forward' propagating plane-wave solutions of the electric and magnetic fields in Eq. 2.1.10. It is important to note the solutions of the PDE are complex valued in general, where the real component (Re{}) of the fields are the constituents of the measurable 'observables'.

$$\tilde{\mathbf{E}}(\mathbf{r}, t) = Re\Big\{\tilde{\mathbf{E}}_0 e^{i(\mathbf{k}\cdot\mathbf{r} - \omega t)}\Big\}, \quad \tilde{\mathbf{H}}(\mathbf{r}, t) = Re\Big\{\tilde{\mathbf{H}}_0 e^{i(\mathbf{k}\cdot\mathbf{r} - \omega t)}\Big\} \tag{2.1.10}$$

where $\mathbf{k} = \frac{2\pi}{\lambda}\hat{\mathbf{k}}$ is the wave vector in a vacuum, λ is the wavelength of the fields, $\hat{\mathbf{k}}$ is the unit vector in the direction of the propagation of the wave front and $\mathbf{r}$ is a vector pointing to a position in space. Note the amplitudes are independent of time for a monochromatic wave.

Substituting Eq.'s 2.1.10 back into Eq.'s 2.1.9,

$$|\mathbf{k}|^2\tilde{\mathbf{E}}_0 = \omega^2\mu_0\epsilon_0\tilde{\mathbf{E}}_0, \tag{2.1.11}$$

by elimination, $\omega = c|\mathbf{k}|$, where $c = 1/\sqrt{\mu_0\epsilon_0}$ is the speed of light in a vacuum. If it's presupposed that the plane waves described in Eq. 2.1.10 are travelling in the z-direction with constant phase wave fronts in the xy-plane then by Eq.'s 2.1.5, 2.1.6, it is necessary that,

$$(\tilde{E}_0)_z = (\tilde{H}_0)_z = 0 \tag{2.1.12}$$

it can be seen from Eq. 2.1.12 that EM waves are transverse in a vaccum since the magnetic and electric fields oscillate in a plane perpendicular to the propagation direction of the wave. Moreover by Eq. 2.1.7, the magnetic field is mutually orthogonal to the electric field and the direction of propagation as seen in Eq. 2.1.13:

$$\tilde{\mathbf{H}}_0 = \frac{1}{c\mu_0}(\hat{\mathbf{z}} \times \tilde{\mathbf{E}}_0). \tag{2.1.13}$$

Electric and magnetic fields travelling in an arbitrary direction in space can be represented then as follows in Eq. 2.1.14 and Eq. 2.1.15,

$$\tilde{\mathbf{E}}(\mathbf{r}, t) = Re\Big\{\tilde{E}_0 e^{i(\mathbf{k}\cdot\mathbf{r}-\omega t)}\Big\}\hat{\mathbf{n}}, \tag{2.1.14}$$

$$\tilde{\mathbf{H}}(\mathbf{r}, t) = Re\Big\{\tilde{H}_0 e^{i(\mathbf{k}\cdot\mathbf{r}-\omega t)}\Big\}\hat{\mathbf{k}} \times \hat{\mathbf{n}} = \frac{1}{c\mu_0}\hat{\mathbf{k}} \times \tilde{\mathbf{E}}, \tag{2.1.15}$$

where $\hat{\mathbf{n}}$ is the unit vector defined by the direction of the electric field vector which will later be addressed as the direction of polarization. It is important to note that only the real part of the fields are measureable.

2.1.3 Energy and Intensity

Electromagnetic radiation is quantized in quantum particles known as photons with energy proportional to the frequency of the field oscillation. In a classical environment where a large number of photons are used in practice, the total energy becomes statistical and the energy of a classical wave is resolved.

Poynting's Theorem proves that the energy flux of an electromagnetic system is defined by the Poynting vector in Eq. 2.1.16:

$$\mathcal{S}(t) \equiv \tilde{\mathbf{E}}(\mathbf{r}, t) \times \tilde{\mathbf{H}}(\mathbf{r}, t), \tag{2.1.16}$$

A single measurement of the frequency of optical light ($\sim 5\times10^{10}$ Hz) will often encompass many oscillations, therefore the periodic term in the energy density equation is time-averaged using integration over a complete cycle and divided by the period of oscillation. The brackets $\langle - \rangle$ are used to denote the time-averaged vector over a single cycle in a periodic system. Substituting the expressions of the fields in Eq's. 2.1.14, 2.1.15 into Eq. 2.1.16, the following expression for the Poynting vector of a monochromatic plane wave is shown, where the observable (real) components of the field are given by the identity $Re\{a\} = (a + a^*)/2$ where * denotes the complex conjugate:

$$\begin{aligned}
\mathcal{S}(t) =& Re\Big\{\tilde{E}_0 e^{i(\mathbf{k}\cdot\mathbf{r}-\omega t)}\Big\} Re\Big\{H_0 e^{(\mathbf{k}\cdot\mathbf{r}-\omega t)}\Big\}\hat{\mathbf{n}}\times(\hat{\mathbf{k}}\times\hat{\mathbf{n}}) \\
=&\Big(\frac{1}{2}(\tilde{E}_0 e^{i(\mathbf{k}\cdot\mathbf{r}-\omega t)} + \tilde{E}_0^* e^{-i(\mathbf{k}\cdot\mathbf{r}-\omega t)})\frac{1}{2}(\tilde{H}_0 e^{i(\mathbf{k}\cdot\mathbf{r}-\omega t)} + \tilde{H}_0^* e^{-i(\mathbf{k}\cdot\mathbf{r}-\omega t)})\Big)\hat{\mathbf{n}}\times(\hat{\mathbf{k}}\times\hat{\mathbf{n}}) \\
=&\frac{1}{2}\Big(\frac{1}{2}(\tilde{E}_0\tilde{H}_0^* + \tilde{E}_0^*\tilde{H}_0) + \frac{1}{2}(\tilde{E}_0\tilde{H}_0 e^{2i(\mathbf{k}\cdot\mathbf{r}-\omega t)} + \tilde{E}_0^*\tilde{H}_0^* e^{-2i(\mathbf{k}\cdot\mathbf{r}-\omega t)})\Big)\hat{\mathbf{n}}\times(\hat{\mathbf{k}}\times\hat{\mathbf{n}}) \\
=&\frac{1}{2}\Big(Re\Big\{\tilde{E}_0\tilde{H}_0^*\Big\} + Re\Big\{\tilde{E}_0\tilde{H}_0 e^{2i(\mathbf{k}\cdot\mathbf{r}-\omega t)}\Big\}\Big)\hat{\mathbf{n}}\times(\hat{\mathbf{k}}\times\hat{\mathbf{n}}) \\
=&\frac{1}{2}\Big(Re\Big\{\tilde{E}_0\tilde{H}_0^*\Big\} + Re\Big\{\tilde{E}_0\tilde{H}_0 e^{2i(\mathbf{k}\cdot\mathbf{r}-\omega t)}\Big\}\Big)\hat{\mathbf{k}}, \qquad (2.1.17)
\end{aligned}$$

where the vector identity $\mathbf{n}\times(\mathbf{k}\times\mathbf{n}) = (\mathbf{n}\cdot\mathbf{n})\mathbf{k} - (\mathbf{n}\cdot\mathbf{k})\mathbf{n}$ is used from $\mathbf{n}\cdot\mathbf{k} = 0$.

The time-cycle average of the Poynting Vector in Eq. 2.1.17 can be calculated using the linearity of the intergal, the cancellation of a harmonic cycling of the period, and the fact that in a vacuum the wave vector ($\mathbf{k}$) is independent in time.

$$\begin{aligned}
\langle\mathcal{S}\rangle =& \frac{1}{T}\int_0^T \tilde{\mathbf{E}}(\mathbf{r},t)\times\tilde{\mathbf{H}}(\mathbf{r},t)dt \\
=& \frac{1}{T}\int_0^T \frac{1}{2}\Big(Re\Big\{\tilde{E}_0\tilde{H}_0^*\Big\} + Re\Big\{\tilde{E}_0\tilde{H}_0 e^{2i(\mathbf{k}\cdot\mathbf{r}-\omega t)}\Big\}\Big)dt\hat{\mathbf{k}} \\
=& \frac{1}{2}Re\Big\{\tilde{E}_0\tilde{H}_0^*\Big\}\hat{\mathbf{k}} = \frac{1}{2}Re\Big\{\tilde{\mathbf{E}}_0\times\tilde{\mathbf{H}}_0^*\Big\}, \qquad (2.1.18)
\end{aligned}$$

Eq. 2.1.18 for the time-averaged Poynting vector can be simplified even further, defined as the Irradiance of an EM wave in a vacuum:

$$|\langle\mathcal{S}\rangle| = \frac{1}{2}c\epsilon_0 {E_0}^2 = \frac{1}{2}c\epsilon_0\langle\tilde{\mathbf{E}}\cdot\tilde{\mathbf{E}}\rangle \equiv I, \qquad (2.1.19)$$

where the equlity, $1/c\mu_0 = c\epsilon_0$,and the inner product in the complex vector field, $\mathbf{a}\cdot\mathbf{b} \equiv \sum_j a_i b_j^*$ has been used.

2.1.4 Interference of Electromagnetic Waves

The PDEs in Eq. 2.1.9 are linear, thus the superposition of two solutions is also a solution. Meaning, if two waves are superimposed on a single point in space

the fields are summed. Assuming the frequency of each field are identical the following interference profile can be derived:

$$\mathbf{E}_1 = \mathbf{E}_{01}e^{i(\mathbf{k}_1\cdot\mathbf{r}_1-\omega_1 t)}, \quad \mathbf{E}_2 = \mathbf{E}_{02}e^{i(\mathbf{k}_2\cdot\mathbf{r}_2-\omega_2 t-\delta_0)}, \tag{2.1.20}$$

$$\mathbf{E}_{r'} = \mathbf{E}_1 + \mathbf{E}_2, \tag{2.1.21}$$

where δ_0 is a phase shift with respect to the interfering field. Substituting Eq. 2.1.21 into Eq. 2.1.19 results in the following Eq. 2.1.22 for the intensity,

$$\begin{aligned} I_{r'} &= \frac{1}{2}c\epsilon_0\langle\tilde{\mathbf{E}_{r'}}\cdot\tilde{\mathbf{E}}_{r'}\rangle \\ &= \frac{1}{2}c\epsilon_0\langle(\tilde{\mathbf{E}}_1+\tilde{\mathbf{E}}_2)\cdot(\mathbf{E}_1+\mathbf{E}_2)\rangle \\ &= \frac{1}{2}c\epsilon_0(\langle\tilde{\mathbf{E}}_1\cdot\tilde{\mathbf{E}}_1\rangle + \langle\tilde{\mathbf{E}}_2\cdot\tilde{\mathbf{E}}_2\rangle + \langle\tilde{\mathbf{E}}_1\cdot\tilde{\mathbf{E}}_2\rangle + \langle\tilde{\mathbf{E}}_2\cdot\tilde{\mathbf{E}}_1\rangle) \\ &= \frac{1}{2}c\epsilon_0(E_{01}^2 + E_{02}^2 + \langle\tilde{\mathbf{E}}_1\cdot\tilde{\mathbf{E}}_2\rangle + \langle\tilde{\mathbf{E}}_2\cdot\tilde{\mathbf{E}}_1\rangle), \end{aligned} \tag{2.1.22}$$

where $\tilde{E}_{01} = \sum_j \tilde{E}_{01,j}\tilde{E}^*_{01,j}$ and $\tilde{E}_{01,j}$ are the components of the vector $\tilde{\mathbf{E}}_{01}$; $\tilde{\mathbf{E}}_{02}$ follows in structure.

$$\langle\tilde{\mathbf{E}}_1\cdot\tilde{\mathbf{E}}_2\rangle = Re\Big\{\Big(\sum_j \tilde{E}_{01,j}\tilde{E}^*_{02,j}\Big)\langle e^{i(\Delta\mathbf{k}\cdot\mathbf{r}-\Delta\omega t+\delta_0)}\rangle\Big\}, \tag{2.1.23}$$

where $\Delta\mathbf{k} = \mathbf{k}_1-\mathbf{k}_2, \Delta\omega = \omega_1-\omega_2$. If we consider an interference of two frequency matched monochromatic waves with identical amplitudes, then $\Delta\omega = 0$. With this assumption Eq. 2.1.23 is written:

$$\begin{aligned} &\langle\tilde{\mathbf{E}}_1\cdot\tilde{\mathbf{E}}_2\rangle + \langle\tilde{\mathbf{E}}_2\cdot\tilde{\mathbf{E}}_1\rangle = Re\Big\{\Big(\sum_j \tilde{E}_{12,j}\Big)\langle e^{i\delta}\rangle\Big\} + Re\Big\{\Big(\sum_j \tilde{E}_{21,j}\Big)\langle e^{-i\delta}\rangle\Big\} \\ =&\frac{1}{2}\Big(\sum_j \tilde{E}_{12,j}\langle e^{i\delta}\rangle + \sum_j \tilde{E}^*_{12,j}\langle e^{-i\delta}\rangle\Big) + \frac{1}{2}\Big(\sum_j \tilde{E}_{21,j}\langle e^{-i\delta}\rangle + \sum_j \tilde{E}^*_{21,j}\langle e^{i\delta}\rangle\Big), \end{aligned} \tag{2.1.24}$$

where $\tilde{E}_{12,j} = \tilde{E}_{01,j}\tilde{E}^*_{02,j}$, $\tilde{E}_{21,j} = \tilde{E}_{02,j}\tilde{E}^*_{01,j}$ and $\delta = \Delta\mathbf{k}\cdot\mathbf{r}-\delta_0$. It can be easily seen that $\tilde{E}^*_{12,j} = \tilde{E}_{21,j}$ for all components. Using this identity the following simplification is made:

$$\begin{aligned} \langle\tilde{\mathbf{E}}_1\cdot\tilde{\mathbf{E}}_2\rangle + \langle\tilde{\mathbf{E}}_2\cdot\tilde{\mathbf{E}}_1\rangle =& \sum_j \tilde{E}_{12,j}\langle e^{i\delta}\rangle + \sum_j \tilde{E}^*_{12,j}\langle e^{-i\delta}\rangle \\ =& 2Re\Big\{\sum_j \tilde{E}_{12,j}\langle e^{i\delta}\rangle\Big\} \\ =& 2Re\Big\{\sum_j \tilde{E}_{12,j}e^{i\delta}\Big\}, \end{aligned} \tag{2.1.25}$$

where the final step, removing the time-cycle averaging operator around the phasor is justified since the argument in the exponential is independent of time. Specifically Eq. 2.1.25 shows a phase dependence arising from the interference of the two wavevectors ($\Delta\mathbf{k}$). Abstracting Eq. 2.1.25 by generalizing the value $\sum_j \tilde{E}_{12,j} = \tilde{E}_{12} = E'_{12} + iE''_{12}$, and transforming the complex value:

$$\begin{aligned} \tilde{E}_{12} =& |\tilde{E}_{12}|e^{i\varphi} \\ |\tilde{E}_{12}| = ((E'_{12})^2 + (E''_{12})^2)^{\frac{1}{2}} \qquad & \varphi = \texttt{atan2}(E''_{12}, E'_{12}) \end{aligned} \tag{2.1.26}$$

Where the $\texttt{atan2}(x, y)$ function is defined in Appendix 1. Eq. 2.1.26 is substitued into the expression in Eq. 2.1.25:

$$\begin{aligned} 2Re\Big\{\sum_j \tilde{E}_{12,j}e^{i\delta}\Big\} =& 2Re\Big\{\tilde{E}_{12}e^{i\delta}\Big\} \\ =& 2|\tilde{E}_{12}|Re\Big\{e^{i(\delta+\varphi)}\Big\} \\ =& 2|\tilde{E}_{12}|\cos(\delta+\varphi) \end{aligned} \tag{2.1.27}$$

Substituting Eq. 2.1.27 into the expression in Eq. 2.1.22 the following expression for the Intensity of interferring identical monochromatic is obtained:

$$I_{r'} = c\epsilon_0\Big(\frac{1}{2}(E_{01}^2 + E_{02}^2) + |\tilde{E}_{12}|\cos(\delta+\varphi)\Big) \tag{2.1.28}$$

It can be seen by inspection of Eq. 2.1.25that if the electric field vector of the interfering beams are identical, then the Intensity pattern is given by the following:

$$I_{r'}(E_{01}, E_{01}) = c\epsilon_0 E_{01}^2(1+\cos\delta) \tag{2.1.29}$$

Therefore under coherent conditions of an interfering beam with an identical electric field vector amplitude, then the Intensity would oscillate, between the closed bounds $[0, 2c\epsilon_0 E_{01}^2]$, with period ($\lambda_I$) defined by the wavevector:

$$\lambda_I = \frac{2\pi}{\Delta\mathbf{k}\cdot\mathbf{r}} \tag{2.1.30}$$

2.1.5 Polarization and its Representations for a Monochromatic Wave

By convention, the polarization is defined by the direction of the electric field vector over a complete cycle. There are two widely used polarization representations shown below.

Jones Representation

A plane wave is linearly polarized when the electric field oscillates along a single dimension as shown in Eq. 2.1.31 where a plane wave described is propagating in the positive z-direction and oscillating along the x-direction:

$$\tilde{\mathbf{E}}(z,t) = E_0 e^{i(kz-\omega t+\phi)}\hat{\mathbf{x}}, \tag{2.1.31}$$

where ϕ is a phase shift. If two orthogonal linearly polarized electric fields with identical frequencies interfere, the resulting polarization is determined by the phase difference of the summed fields:

$$\begin{aligned}\mathbf{E}_T(z,t) &= E_{0x}e^{i(kz-\omega t+\phi_1)}\hat{\mathbf{x}} + E_{0y}e^{i(kz-\omega t+\phi_2)}\hat{\mathbf{y}} &(2.1.32)\\ &= (E_{0x}e^{i\phi_1}\hat{\mathbf{x}} + E_{0y}e^{i\phi_2}\hat{\mathbf{y}})e^{i(kz-\omega t)} &(2.1.33)\end{aligned}$$

Extracting the harmonic component in Eq. 2.1.33 results in a simplification of the expression as shown in Eq. 2.1.36,

$$\begin{aligned}\mathbf{E}_s &= E_{0x}e^{i\phi_1}\hat{\mathbf{x}} + E_{0y}e^{i\phi_2}\hat{\mathbf{y}} &(2.1.34)\\ &= E_{0x}e^{i\phi_1}\begin{bmatrix}1\\0\end{bmatrix} + E_{0y}e^{i\phi_2}\begin{bmatrix}0\\1\end{bmatrix} &(2.1.35)\\ &= \begin{bmatrix}E_{0x}e^{i\phi_1}\\E_{0y}e^{i\phi_2}\end{bmatrix}, &(2.1.36)\end{aligned}$$

where Eq. 2.1.36 is called the Jones vector and represents 2D polarization states with components being complex in general.

When the phase difference ($\Delta\phi$), as defined in Eq. 2.1.37

$$\Delta\phi = \phi_2 - \phi_1 \equiv \phi, \tag{2.1.37}$$

is equivalent to an odd multiple of $\frac{\pi}{2}$ ($m\pi/2$; $m = \mathbb{Z}_{odd}$) and the amplitudes of the two components are equivalent, the resulting electric field will be circularly polarized.

A superposition of two normalized fields with an identical frequency is represented as an addition of their corresponding Jones vector. As shown in Fig. 2.1, a superposition of oppositely handed circular polarizations will interfere and will generate a LP beam.

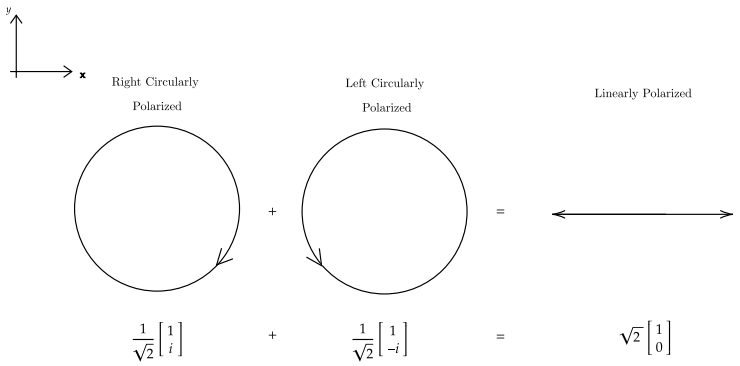

Figure 2.1: Normalized Jones vector addition with a graphic representation with a coordinate reference frame

A Jones matrix $\bar{\mathbf{J}}$ often thought of as a transfer function representing a polarization transformation due to, in general, the anisotropy of the refractive index of the optical element[69]. When a field passes through a non-attenuative optical element, the state of the field and its corresponding polarization will be transformed and is represented by a 2x2 matrix as shown in Eq. 2.1.38

$$\bar{\mathbf{J}} = \begin{bmatrix} a_{11} & a_{12} \\ a_{21} & a_{22} \end{bmatrix} \tag{2.1.38}$$

A rotation of a Jones matrix by an angle θ is represented mathematically by Eq. 2.1.39, where the set of unitary rotation matrices are shown in Eq. 2.1.40:

$$\bar{\mathbf{J}}' = \bar{\mathbf{R}}(\theta)\bar{\mathbf{J}}\bar{\mathbf{R}}^{-1}(\theta) \tag{2.1.39}$$

$$\bar{\mathbf{R}} = \begin{bmatrix} \cos\theta & -\sin\theta \\ \sin\theta & \cos\theta \end{bmatrix} \qquad \bar{\mathbf{R}}^{-1} = \begin{bmatrix} \cos\theta & \sin\theta \\ -\sin\theta & \cos\theta \end{bmatrix} \tag{2.1.40}$$

Stokes Parameters and Poincaré Sphere

Jones vectors can only represent fully polarized fields, as unpolarized EM fields do not have a statistically preferential polarization direction over a single or multiple cycles. A more complete polarization space can be fully realized using a set of parameters (Stokes Parameters) which can be derived from a normalized ellipsoid space and coordinately transformed into a natural spherical coordinate system (Poincaré Sphere).

Without loss of generality, polarized EM fields can be represented as a polarization ellipse, characterized by the field amplitudes and a phase difference of the orthogonal field components similar to the Jones formulation,

$$E_x = E_{0x}\cos(\tau + \phi_1) \qquad E_y = E_{0y}\cos(\tau + \phi_2), \tag{2.1.41}$$

with a change of variables given by Eq. 2.1.42:

$$\tau = kz - \omega t \tag{2.1.42}$$

Through some manipulation, the set of parametric equations in Eq. 2.1.41 are reformulated into Eq.'s 2.1.43, 2.1.44 using the angle-sum identity ($\cos(\alpha+\beta) = \cos(\alpha)\cos(\beta) - \sin(\alpha)\sin(\beta)$):

$$\frac{E_x}{E_{0x}} = \cos(\tau)\cos(\phi_1) - \sin(\tau)\sin(\phi_1) \tag{2.1.43}$$

$$\frac{E_y}{E_{0y}} = \cos(\tau)\cos(\phi_2) - \sin(\tau)\sin(\phi_2) \tag{2.1.44}$$

Where through cancellation and use of the angle-difference identity the following equations are derived:

$$\frac{E_x}{E_{0x}}\sin(\phi_2) - \frac{E_y}{E_{0y}}\sin(\phi_1) = \cos(\tau)\sin(\phi_2 - \phi_1), \tag{2.1.45}$$

$$\frac{E_x}{E_{0x}}\cos(\phi_2) - \frac{E_y}{E_{0y}}\cos(\phi_1) = \sin(\tau)\sin(\phi_2 - \phi_1). \tag{2.1.46}$$

Squaring and adding Eq. 2.1.45 and Eq. 2.1.46, the unique form of a conic section ($Ax^2 + Bxy + Cy^2 = D$) with respect to the polarization components is formed,

$$(\frac{E_x}{E_{0x}})^2 - 2\frac{E_x}{E_{0x}}\frac{E_y}{E_{0y}}\cos(\phi) + (\frac{E_y}{E_{0y}})^2 = \sin^2(\phi), \tag{2.1.47}$$

where ϕ is defined by Eq. 2.1.37. Since the discriminant ($B^2 - 4AC$) of Eq. 2.1.47 is negative the polarization equation uniquely forms an ellipse[70]. In general the ellipse axes will not fall directly on the coordinate axes, therefore special care of this case is shown, where the field vectors are defined in terms of the orientation of the principal axes of the ellipse shown in Fig. 2.2.

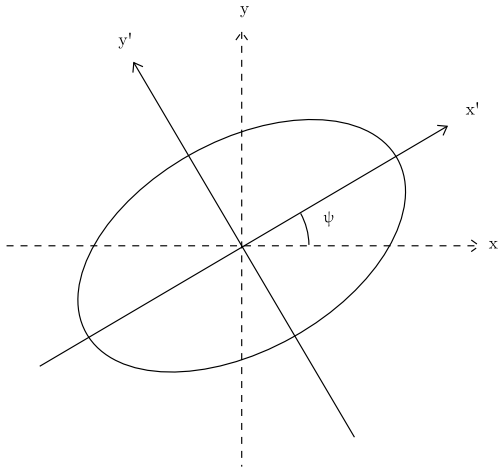

Figure 2.2: 2D cross section of an off-axes orientated ellipse

The polarization fields in Eq. 2.1.41 can be rotated around the out of plane axis as shown in Eq. 2.1.48:

$$E_{x'} = E_x \cos(\psi) + E_y \sin(\psi) \qquad E_{y'} = -E_x \sin(\psi) + E_y \cos(\psi), \tag{2.1.48}$$

The set of parametric equations in Eq. 2.1.49 uniquely represent the general ellipse on condition that $E_{0x'} \geq E_{0y'}$:

$$E_{x'} = E_{0x'} \cos(\tau + \phi_0) \qquad E_{y'} = \pm E_{0y'} \sin(\tau + \phi_0) \tag{2.1.49}$$

Some more manipulation of these set of independent equations describing a rotated ellipse in Eq.'s 2.1.48, 2.1.49 can be seen in Appendix B; using familiar sum and difference-trigonometric identities the following equalities are obtained[70]:

$$E_{0x'}^2 + E_{0y'}^2 = E_{0x}^2 + E_{0y}^2 \tag{2.1.50}$$

$$\tan 2\psi = \tan(2\alpha)\cos(\phi) \tag{2.1.51}$$

$$\sin 2\chi = \sin(2\alpha)\sin(\phi) \tag{2.1.52}$$

where α, χ are auxillary angles defined by Eq. 2.1.53:

$$\tan\alpha = \frac{E_{0y}}{E_{0x}} \qquad \tan\chi = \mp\frac{E_{0y'}}{E_{0x'}} \tag{2.1.53}$$

Polarization was mathematically defined by G.G.Stokes when first trying to understand intensity measurements with unpolarized light. A set of parameters in

Eq. 2.1.54 first defined by G.G. Stokes fully describe 2D polarization states of a plane wave[71].

$$\begin{aligned} S_0 &= E_{0x}^2 + E_{0y}^2 \\ S_1 &= E_{0x}^2 - E_{0y}^2 \\ S_2 &= 2E_{0x}E_{0y}\cos(\phi) \\ S_3 &= 2E_{0x}E_{0y}\sin(\phi) \end{aligned} \tag{2.1.54}$$

The stokes parameters ,S_0, S_1, S_2, S_3, are proportional to the total intensity, horizontally linearly polarized intensity, intensity of linearly polarized light at 45^o from horizontal, and right circularly polarized intensity of the plane wave respectively. S_0 is dependent on the three other parameters(S_1, S_2, S_3), $S_0^2 = S_1^2 + S_2^2 + S_3^2$, unique to a construction of a 3D sphere with the Euclidean norm shown in Fig. 2.3. The spherical relationship is precisely defined by a change of variables given by Eq. 2.1.55[70]:

$$\begin{aligned} S_1 &= S_0\cos 2\chi\cos 2\psi \\ S_2 &= S_0\cos 2\chi\sin 2\psi \\ S_3 &= S_0\sin 2\chi \end{aligned} \tag{2.1.55}$$

where ψ defines the angle of orientation of the ellipse in the plane as shown in Fig. 2.2 and χ describes the ellipticity by the magnitude ($|\chi| = \pi/4$ circularly polarized light, $0 < |\chi| < \pi/4$ represents elliptical polarizations), and the handedness by the sign (-:left-handedness,+:right-handedness). Handedness is the descriptor of the rotation direction around the axis of propagation when observing from the direction of the beam, where right-handed and left-handed light would have an electric field moving in the clockwise direccction and counter-clockwise direction respectively.

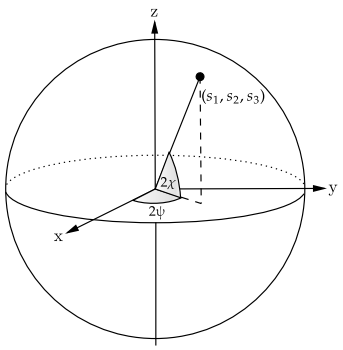

Figure 2.3: Figure of the Poincaré sphere

2.1.6 Radial and Azimuthal Polarization

The Helmholtz equation, $(\nabla^2 + k^2)E = 0$, has an infinite set of solutions in the paraxial approximation (assuming rays make a small angle from the optical axis) given by Eq. 2.1.56,

$$E = u(x, y, z)e^{i(kz-\omega t)}, \tag{2.1.56}$$

where the plane wave solution in Eq. 2.1.10 is characterized by a constant spatial amplitude $u(x, y, z) = E_0$. More classes of solutions are derived by substitution of Eq. 2.1.56 into the Helmholtz equation, assuming separation of variables ($u(x, y, z) = u(x)u(y)u(z)$), and the slowly-varying envelope approximation (SVEA), where the SVEA simply assumes that the amplitude of the electric field oscillates slowly:

$$|\frac{\partial^2 u}{\partial z^2}| << |k\frac{\partial u}{\partial z}|, \qquad |\frac{\partial^2 u}{\partial z^2}| << |k^2 u| \tag{2.1.57}$$

In other words, the inequality in Eq. 2.1.57 allows for the higher order derivatives of the field in the direction of propagation to be neglected, and the following simplification of the Helmholtz PDE shown in Eq. 2.1.58:

$$\nabla_\perp^2 u + 2ik\frac{\partial u}{\partial z} = 0, \tag{2.1.58}$$

where $\nabla_\perp = \partial^2/\partial x^2 + \partial^2/\partial y^2$

Under cartesian coordinates the class of solutions are called the Hermite-Gaussian (HG) modes with symmetries along the x and y axes. Whereas cylindrical coordinate systems ($u \to u(r, \phi, z)$) generate a couple of classes of solutions, including the Laguerre-Gaussian (LG) modes which have a 'vortex' term ($e^{il\phi}$) and the Bessel-Gaussian (BG) modes which are independent of the azimuthal angle ($u \to u(r, z)$).These cylindrical coordinate beams are naturally called CVBs

and have been applied frequently, especially in regards to the LG modes' $e^{il\phi}$ term where l is directly linked with the presence of angular momentum in a photon[72].

CVBs and their corresponding polarization states have been rigourously studied for their angular momentum and focal point compression properties. Using vectorally inclusive theories derived from Maxwell's Equations,$\nabla \times \nabla \times \mathbf{E} - k^2\mathbf{E} = 0$, it's known that the first LG modes have radial and azimuthal polarization states[31].

Higher Order Poincaré Sphere

In the past decade a theoretical framework of observable Stokes'-like parameters for beams with orbital angular momentum (OAM). Specifically a model framework for generalizing a CVB's Stokes vector via a change in basis of polarization including both the spin angular momentum (SAM) of circular polarization and orbital angular momentum from the phase singularitites associated with a helical phase front of the electric field[73]. Geometric phases have been introduced through the lens of a higher-order Poincaré sphere (HOPS) models and geodesics traced from transformations of stokes parameters. This framework has been shown to be exploited in intracaivity devices where the alteration of the geometric phase allows for pure excitation of laser beams with OAM[74].

2.1.7 Gratings and Interference Lithography

Gratings create a periodic variation in a media utilizing the diffractive properties of a wave, splitting the far field intensity into a wavelength dependent spatial period defined by Eq. 2.1.59:

$$\Lambda(\sin\theta_m \pm \sin\theta_i) = m\lambda; \qquad m = 0, \pm 1, \pm 2, ... \tag{2.1.59}$$

Λ is the period of the grating, θ_m is the angle of the m-th diffractive mode and θ_i is the angle of incidence onto the grating from the normal surface.

The intensity-polarization response of an azopolymer film enables the creation of SRGs via an interference lithographic configuration and a coherent light source with wavelength λ_{beam}. If the inscribing beam is collimated and centered on a truncated conic mirror (circular diffraction grating generator (CDG)), concentric rings of periodic intensity with a constant period given in Eq. 2.1.60 will be produced at the plane of interference shown in Fig. 2.4:

$$\Lambda = \lambda_{beam} \csc 2\theta_{cdg} \tag{2.1.60}$$

where θ_{cdg} is the nominal angle of the cone shown in Fig. 2.4.

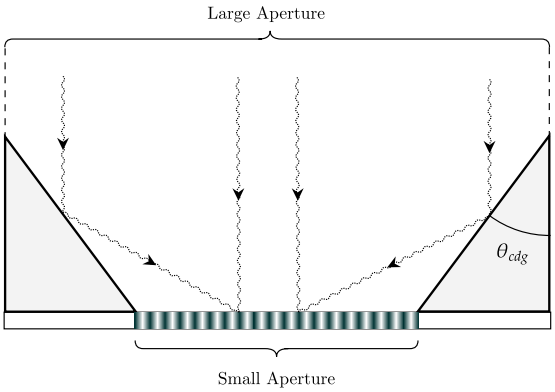

Figure 2.4: Cross section of the CDG

Adding a lens prior to the CDG produces chirped SRGs. The chirped pitch decreases from the center when the focal point lies ahead of the interference plane (diverging) and increases from the center when the focal point lies behind the interference plane (converging). The chirped pitch equation is transcendental including parameters such as the location of the focal point (s), width of the small aperature (m) and the distance from the center(δ_c). The pitch prediction can be solved numerically through ray tracing simluations[61].

In Appendices 1.A, a novel proof of Eq. 2.1.60 is shown, where Eq. 2.1.30 is used to derive the periodic relationship in Eq. 2.1.60. This approach condenses the original proof and follows a similar wavevector approach shown previously in work with linear gratings on Lloyd mirror setups[75]. The wavevector approach allows an analysis of the interference pattern on varying planes of interference.

2.2 EM Fields in Linear Media

A material's free charge carriers (electrons) characterize the materials ability to polarize an electric field, either static or transient.

In a homogeneous, isotropic, and linear dielectric media, the polarizability of a material in a static elecric field is defined by:

$$\mathbf{P} = \epsilon_0 \chi_e \mathbf{E}, \qquad \chi_e = 1 - \epsilon_r, \tag{2.2.1}$$

where χ_e is the electric susceptibility and $\epsilon_r = \epsilon/\epsilon_0$ is the relative permittivity. In a changing electric field, as is the case with electrogmagnetic radiation, a general time-dependent formulation of the polarizibility is given as a convolution:

$$\mathbf{P}(t) = \epsilon_0 \int_{-\infty}^{t} \chi_e(t - t')\mathbf{E}(t')dt'. \tag{2.2.2}$$

In a linear system, the fourier transform of Eq. 2.2.2, by the convolution theorem, is given by:

$$\mathbf{P}(\omega) = \epsilon_0 \chi_e(\omega)\mathbf{E}(\omega). \tag{2.2.3}$$

As shown in Eq. 2.2.1, the electric susceptibility is related to the relative permittivity (ϵ_r). Therefore it is noted that the permittivity is frequency dependent, represented as a phase shift or simply a complex function dependent on the angular frequency:

$$\epsilon = \epsilon' + i\epsilon'' = \epsilon' + i\frac{\sigma}{\omega}, \tag{2.2.4}$$

where i is the imaginary unit and σ is the conductivity of the material.

In lossless dielectrics, the imaginary part of the dielectric permittivity is negligible ($\sigma/\omega << 1$) and the polarization of the field is determined by Eq. 2.2.1. In a classical conductor the imaginary part of the dielectric permittivity is non-negligible ($\sigma/\omega >> 1$) and represented as a complex number in Eq. 2.2.4.

2.2.1 Drude Theory of Metals

The Drude theory of metals is a classical description of free non-interacting charged particles in a matrix of fixed oppositely charged massive particles. Collisions cause a damping force on the electrons represented in Eq. 2.2.5,

$$F_e = F_{Driving} + F_{Damping} \Longrightarrow m_e\langle\dot{\mathbf{v}}\rangle = -e\mathbf{E} - m_e\gamma\langle\mathbf{v}\rangle, \tag{2.2.5}$$

where $\gamma = \frac{1}{\tau_c}$, m_e is the mass of the electron, e is the elementary charge, τ_c is the average time between collisions, $\mathbf{v}$ and $\dot{\mathbf{v}}$ is the velocity and its time derivative (acceleration) of the electrons respectively. The electric field can be expressed as $\mathbf{E} = Re(\mathbf{E}_0(\omega)e^{-i\omega t})$ and substituted into Eq. 2.2.5:

$$m_e(\langle\dot{\mathbf{v}}\rangle + \frac{1}{\tau}\langle\mathbf{v}\rangle) = -e\mathbf{E} \Longrightarrow \langle\dot{\mathbf{J}}\rangle + \frac{1}{\tau}\langle\mathbf{J}\rangle = \frac{Ne^2}{m_e}\mathbf{E} \tag{2.2.6}$$

Equation 2.2.5 is rearranged and multiplied by Ne to both sides in Eq. 2.2.6, where N is the number of electrons in the system. The result is a differential equation of the current density($\langle\mathbf{J}\rangle = Ne\langle\mathbf{v}\rangle$), where $\mathbf{J}$ has the same frequency as the driving electric field as expressed in Eq. 2.2.7:

$$\mathbf{J} = Re(\mathbf{J}_0 e^{-i\omega t}) \tag{2.2.7}$$

Substituting Eq. 2.2.7 into Eq. 2.2.6 and isolating for the current density the following expression is found,

$$\mathbf{J}(\omega) = \frac{Ne^2/m_e}{1/\tau - i\omega}\mathbf{E}, \tag{2.2.8}$$

where by use of Ohm's law the conductivity is further obtained in Eq. 2.2.9:

$$\sigma(\omega) = \frac{Ne^2\tau_c/m_e}{1 - i\omega\tau_c} \tag{2.2.9}$$

2.2.2 Plasma Frequency and Dispersion in a Drude Metal

The wave front propagation and its dependency on the frequency of the propagative mode is referred to as the disprsion relationship of a material. Assuming all coordinate axes for interferring beams are congruent, then the defining characteristics of a propagative mode are $\mathbf{k}$, ω and the polarization which determine the space-time evolution of the EM field.

The complex dielectric function for a Drude metal is derived using Eq. 2.1.4 and Eq. 2.2.9,

$$\epsilon = (\epsilon_B - \frac{\omega_p^2\tau_c^2}{1+\omega^2\tau_c^2}) + i(\frac{\omega_p^2\tau_c^2}{\omega\tau_c + \omega^3\tau_c^3}), \tag{2.2.10}$$

where ϵ_B is the dielectric contribution from bound electrons and $\omega_p^2 = \frac{Ne^2}{\epsilon_0 m_e}$ is the bulk plasma frequency. When $\omega\tau_c >> 1$ Eq. 2.2.10 is approximated by the following expression:

$$\epsilon \approx \epsilon_B - \frac{\omega_p^2}{\omega^2} \tag{2.2.11}$$

If $\frac{\omega_p^2}{\omega^2} >> 1$ and $|\epsilon_B| \sim O(1)$ then $\epsilon' < 0$.

Helmholtz's equation and its solutions enforce the equality, $\omega^2\epsilon_r = c^2k^2$. Substituting Eq. 2.2.11 into the preceeding equality and rearranging gives the dispersion relationship for bulk plasmons,

$$\omega = \epsilon_B^{-1/2}\sqrt{\omega_p^2 + c^2k^2}, \tag{2.2.12}$$

where $\epsilon_r = \epsilon/\epsilon_0$ is the relative permittivity.

2.3 Surface Plasmons and Photon Coupling

Drude metals have been shown to have a negative real component of the electric permittivity in the optical and infrared regime. Physically, this represents a reflection of the photons at the surface caused by the free electrons in the metal. The imaginary component in the dielectric function represents the attenuation of the photons in the bulk metal. Bound modes of the EM field can occur at the surface of a metal-dielectric interface, subsequently producing a field enhancement at the surface[1].

The bound modes are generated by charge density oscillations at a metal-dielectric interface called surface plasmons (SPs).

2.3.1 Boundary Conditions and Surface Plasmons

The permittivity at the boundary for a flat dielectric-metal is given by,

$$\epsilon(y) = \begin{cases} \epsilon_m & y \leq 0 \\ \epsilon_d & y \geq 0, \end{cases} \tag{2.3.1}$$

where ϵ_m, ϵ_d are the dielectric functions of the metal and dielectric respectively.

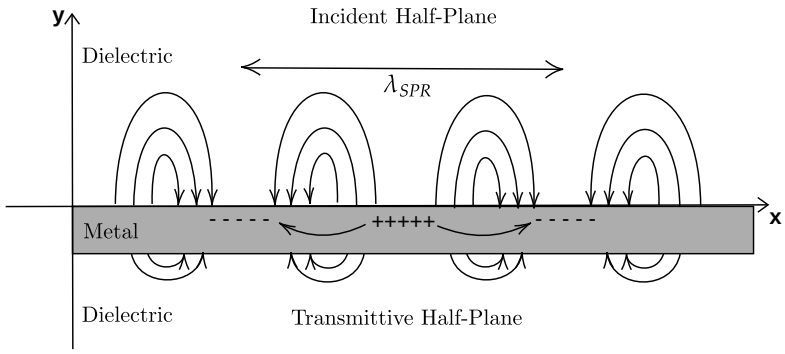

Figure 2.5: Cross-section representation of the electrical fields in a bound SPR mode by interacting free electrons

The fields for the SP mode have a bound, oscillatory component at the surface with an evanescent component away from the surface, written below (and shown in Fig. 2.5):

$$\tilde{\mathbf{E}} = \begin{cases} \tilde{\mathbf{E}}_{0,m} e^{i(k_{x,m}x + ik_{y,m}y)} & y \leq 0 \\ \tilde{\mathbf{E}}_{0,d} e^{i(k_{x,d}x + ik_{y,d}y)} & y \geq 0 \end{cases} \tag{2.3.2}$$

$$\tilde{\mathbf{H}} = \begin{cases} \tilde{\mathbf{H}}_{0,m} e^{i(k_{x,m}x + ik_{y,m}y)} & y \leq 0 \\ \tilde{\mathbf{H}}_{0,d} e^{i(k_{x,d}x + ik_{y,d}y)} & y \geq 0 \end{cases} \tag{2.3.3}$$

The complex amplitudes and wave vectors in Eq.'s 2.3.2, 2.3.3 are specified with subscripts to denote the occupying media of the fields ('m','d'):

$$\tilde{\mathbf{E}}_0 = [E_x, E_y, 0], \quad \tilde{\mathbf{H}}_0 = [0, 0, H_z] \tag{2.3.4}$$

Using limiting conditions at the interface dictated by Maxwell's equations, the

following boundary equalities must be satisfied[1]:

$$\tilde{\mathbf{E}}_x(y \to 0^-) = \tilde{\mathbf{E}}_x(y \to 0^+) \tag{2.3.5}$$

$$\tilde{\mathbf{H}}_z(y \to 0^-) = \tilde{\mathbf{H}}_z(y \to 0^+) \tag{2.3.6}$$

$$\epsilon_m \tilde{\mathbf{E}}_y(y \to 0^-) = \epsilon_d \tilde{\mathbf{E}}_y(y \to 0^+) \tag{2.3.7}$$

Substituting the fields in Eq. 2.3.2 into Eq. 2.3.5 and evaluating:

$$\tilde{\mathbf{E}}_x(x \to 0, y \to 0^-) = \tilde{\mathbf{E}}_x(x \to 0, y \to 0^+) \Longrightarrow E_{x,m} = E_{x,d}, \tag{2.3.8}$$

the wave vector tangent to the surface is given by:

$$k_{x,m} = k_{x,d} \equiv k_x. \tag{2.3.9}$$

Using Eq. 2.1.4 and substituting the SP fields of Eq. 2.3.2 into Eq. 2.3.7 the wave vector relationship normal to the surface is given by:

$$\frac{k_{y,m}}{\epsilon_m} = \frac{k_{y,d}}{\epsilon_d}. \tag{2.3.10}$$

Eq. 2.3.11 and Eq. 2.3.9 are derived with the assumption of a zero surface charge and current density environment, and is valid in a field averaged approximation along the whole surface.
The Helmholtz equation and its general solutions provide the dispersion relationship for a non-magnetic material media found in Eq. 2.3.11:

$$k^2_{(d,m)} = k_x^2 + k^2_{y,(d,m)} = \omega^2 \mu_0 \epsilon_{(d,m)} \tag{2.3.11}$$

The SP wave vector can be isolated in the form where $k = k' + ik''$, using Eq.'s 2.3.10, 2.3.11 and with help of identity $\sqrt{a+ib} = \pm\left(\sqrt{\frac{|z|+a}{2}} + i\frac{b}{|b|}\sqrt{\frac{|z|-a}{2}}\right)$:

$$k'_x = \frac{\omega}{c}\left[\frac{\epsilon_{r,d}}{(\epsilon'_{r,m}+\epsilon_{r,d})^2 + (\epsilon''_{r,m})^2}\right]^{\frac{1}{2}} \cdot \left[\frac{\epsilon^2_{r,c} + \sqrt{\epsilon^4_{r,c} + (\epsilon''_{r,m}\epsilon_{r,d})^2}}{2}\right]^{\frac{1}{2}} \tag{2.3.12}$$

$$k''_x = \frac{\omega}{c}\left[\frac{\epsilon_{r,d}}{(\epsilon'_{r,m}+\epsilon_{r,d})^2 + (\epsilon''_{r,m})^2}\right]^{\frac{1}{2}} \cdot \left[\frac{(\epsilon''_{r,m}\epsilon_{r,d})^2}{2(\epsilon^2_{r,c} + \sqrt{\epsilon^4_{r,c} + (\epsilon''_{r,m}\epsilon_{r,d})^2})}\right]^{\frac{1}{2}} \tag{2.3.13}$$

$$\epsilon^2_{r,c} = (\epsilon'_{r,m})^2 + (\epsilon''_{r,m})^2 + \epsilon_{r,d}\epsilon'_{r,m} \tag{2.3.14}$$

The subscript 'r' denotes the relative permittivity for both the dielectric and metal. Assuming $\epsilon''_{r,m} << \epsilon'_{r,m}$, Eq.'s 2.3.12, 2.3.13 can be approximated as follows:

$$k'_x \approx \frac{\omega}{c}\left(\frac{\epsilon_{r,d}\epsilon'_{r,m}}{\epsilon_{r,d}+\epsilon'_{r,m}}\right)^{\frac{1}{2}} \tag{2.3.15}$$

$$k''_x \approx \frac{\omega}{c}\left(\frac{\epsilon_{r,d}\epsilon'_{r,m}}{\epsilon_{r,d}+\epsilon'_{r,m}}\right)^{\frac{3}{2}}\frac{\epsilon''_{r,m}}{\epsilon'_{r,m}} \tag{2.3.16}$$

A bounded mode exists if k'_x is real which is true when $|\epsilon'_{r,m}| > \epsilon_d$ and $\epsilon'_{r,m} < 0$. The latter is shown to be true in a Drude metal when $\omega < \omega_p$ and the former can be chosen appropriately by design. The real and imaginary wave vector components of the SP mode represent the propagation and the attenuation of the wave respectively. An expression for the evanescent wave vector away from the surface, $k_{y,(m,d)}$, can be derived in a similar manner[1].

The dispersive nature of an SP mode on a flat surface in Eq. 2.3.15 is inconsistent with light in a homogeneous material. In other words, light incident on a flat metal-dielectric surface will not couple to the SP mode. Therefore other methods must be used to excite a surface plasmon resonance (SPR).

2.3.2 Surface Plasmon Resonance and Grating Coupling

SPRs occur when photons couple to the SP mode creating a quasiparticle which reradiates an enhanced field at the coupling wavelength. Metallic layered SRGs have the ability to excite an SPR response as will be discussed next.

Using the grating equation in Eq. 2.1.59, the wavevector of incident light on an SRG is

$$k_{light} = k\sin\theta_i + K, \tag{2.3.17}$$

where $K = 2\pi/\Lambda$, Λ is the pitch of the grating, θ_i is the projected angle with respect to the grating vector (GV) and $k = \sqrt{\epsilon'_{r,m}}k_0$. Substituting Eq. 2.3.15 into 2.3.17 and rearranging for the coupling wavelength (λ_{SP}) results in the equation:

$$\lambda_{SP} = n_d\left(\sqrt{\frac{\epsilon'_{r,m}}{n^2_{r,d}+\epsilon'_{r,m}}} \mp sin(\theta_i)\right)\Lambda, \tag{2.3.18}$$

where n_d is called the refractive index of the dielectric and is related to the permittivity by $n_d = \sqrt{\epsilon_d}$. The coupling of photons to the SP mode require an electric field in the direction of the GV, and therefore only light polarized parallel to the GV will induce an SPP excitation. The equality in Eq. 2.3.18 is an approximation to the wavelength derived from a perfectly flat surface. The approximation fails when the depth of the grating is a significant percentage of the relative coupling wavelength[1].

To add context to the following conversation on polarization conversion via SP coupling, and experimental results using beams with both OAM and SAM

to induce SPP on circular gratings; the geometric phase associated with polarization transformations and the curvature of the Poincaré sphere is conserved in the, light→ SPP→ light, process[76]. This is something to keep in mind when discussing intensity measurements of the SPP intensity profile.

2.3.3 Circular Symmetry on SPP Polarization

A linear grating has an unchanging cross section producing a constant surface plasmon resonance (SPR) response with linear polarization at the coupling wavelength. In comparison, a CG has a GV which rotates around the center and an SPR intensity corresponding to the projection of the polarization on the GV, represented in Fig. 2.6.

A low curvature region on a circular grating can be approximated as a linear grating and loses validity when the curvature increases towards the center of the CG. Consider a linearly polarized beam along the y-axis with the desired

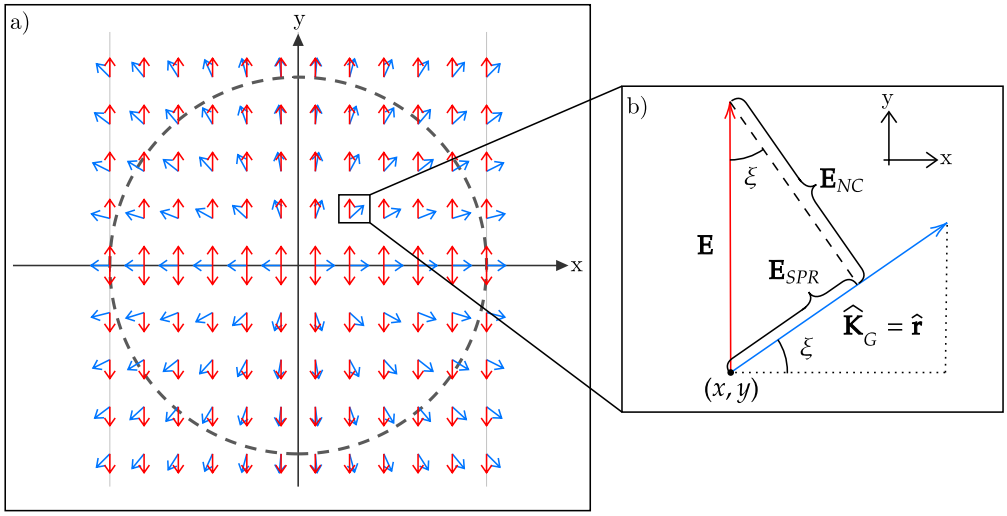

Figure 2.6: Representation of a Linearly Polarized Beam's Electric Field (red), and the normalized GV (blue) for a circular grating with a normal boundary (dashed)

SP wavelength (λ_{SP}) covering the surface of a circular grating shown in Fig. 2.6. The intensity of the SPR should be greatest along the y-axis, decreasing as the component of the electric field projected onto the GV decreases to zero along the x-axis.

The linearly polarized field shown in Fig. 2.6 is described in polar coordinates, expressing the electric field in terms of the coupling (E_{SPR}) and non-coupling (E_{NC}) components in Eq. 2.3.19. The coordinate transformation of cartesian to

polar coordinate system in Eq. 2.3.19 creates a singularity at the origin where the electric field isn't defined even though the pre image of the field is uniquely constant in the y-dir.:

$$\mathbf{E} = E_0(\sin\xi\hat{\mathbf{r}} + \cos\xi\hat{\boldsymbol{\theta}}) = E_{SPR}\hat{\mathbf{r}} + E_{NC}\hat{\boldsymbol{\theta}} \tag{2.3.19}$$

The magnitude of the GV can be neglected when the wavelength of the exciting field is uniquely the coupling wavelength of the SP mode ($\mathbf{E}(\lambda_{SP})$). The unit direction of the GV is then sufficient for the following discussion and provides simplification in the form of Eq. 2.3.20:

$$\mathbf{K}_G = \hat{\mathbf{r}} \tag{2.3.20}$$

Note Eq. 2.3.19 alters the phase information of the fields outside of the quarter plane, though it still preserves the intensity norm of the electric field and can be simply addressed by specifying quarter plane piecewise functions correcting for sign changes.

In Eq. 2.3.21, the angle between the GV and the field polarization is given by the dependency of the coordinates of the GV:

$$\xi = \arctan\frac{y}{x} \tag{2.3.21}$$

The transformation of basis vectors from a cartesian to a radial coordinate system is given in terms of Eq. 2.3.21 and shown in Eq. 2.3.22. This is important in regards to the geometry of the grating since it allows for the separation of SPR coupling and noncoupling components:

$$\hat{\mathbf{r}} = \cos\xi\hat{\mathbf{x}} + \sin\xi\hat{\mathbf{y}} \qquad \hat{\boldsymbol{\theta}} = -\sin\xi\hat{\mathbf{x}} + \cos\xi\hat{\mathbf{y}} \tag{2.3.22}$$

Substituting these unit vectors into Eq. 2.3.19 gives the following vector expressions:

$$\hat{\mathbf{E}}_{SPR} = E'_{SPR}\begin{bmatrix}\cos\xi\sin\xi\\ \sin^2\xi\end{bmatrix} \qquad \hat{\mathbf{E}}_{NC} = E'_{NC}\begin{bmatrix}-\cos\xi\sin\xi\\ \cos^2\xi\end{bmatrix} \tag{2.3.23}$$

With respect to the surface modes of the SPR, it is understood that $E_{SPR,surface} \gg E_{NC,surface}$ and further $E_{SPR,T} \gg E_{NC,T}$, where the subscript 'T' indicates the transmission modes through an optically thick metallic film. It follows that $E_{NC,T}/E_{SPR,T} \ll 1$ and therefore the ratio $\mathbf{E}_T/E_{SPR,T}$ of the transmission field has a dominant component and can be approximated as in Eq. 2.3.24:

$$\mathbf{E} \approx \mathbf{E}_{SPR}, \tag{2.3.24}$$

where the subscript 'T' is dropped for the remainder of the discussion.

The SPR fields destructively interfere in reflection,therefore with help from the

relationship, $E_{SPR}/E_{NC} \ll 1$, a discussion on the intensity profile would follow in a similar manner.

Using the field approximation in Eq. 2.3.24 and the definition of Intensity in Eq. 2.1.19, the intensity profile of the SPR signal is explored. It is important to note that E_{SPR} field is dependent on multiple parameters, including the materials characterizing the surface, the film thickness when observing in transmission and the surface profile. The relationship between the incident field amplitude (E_0) and the SPR field amplitude E_{SPR} in Eq. 2.3.19 is removed from this discussion. Therefore we will simply consider E_{SPR} as a scalar from which it can be removed out of the dot product when normalizing the intensity profile in Eq. 2.3.25:

$$I \propto \begin{bmatrix} \cos\xi \sin\xi & \sin^2\xi \end{bmatrix} \begin{bmatrix} \cos\xi \sin\xi \\ \sin^2\xi \end{bmatrix} = \sin^2\xi \tag{2.3.25}$$

Cross-sections of Eq. 2.3.25 are plotted in Fig. 2.7(a),(b) with constant y and x coordinates respectively. These plots show that as we take horizontal cross-sections (Fig 2.7(a)) closer to $y = a = 0$, the functions converge to zero everywhere but at the origin. This is contrasted by the plots in Fig. 2.7(b) where vertical cross-sections are plotted closer to $x = a = 0$. Here, the plots converge to 1 everywhere but 0 at the origin. Therefore, it is important to note that the intensity profile in Eq. 2.3.25 is undefined at the origin.

$$I_{SPR}(x,a) = \sin^2(\arctan\frac{a}{x}) \quad I_{SPR}(a,y) = \sin^2(\arctan\frac{y}{a}) \tag{2.3.26}$$

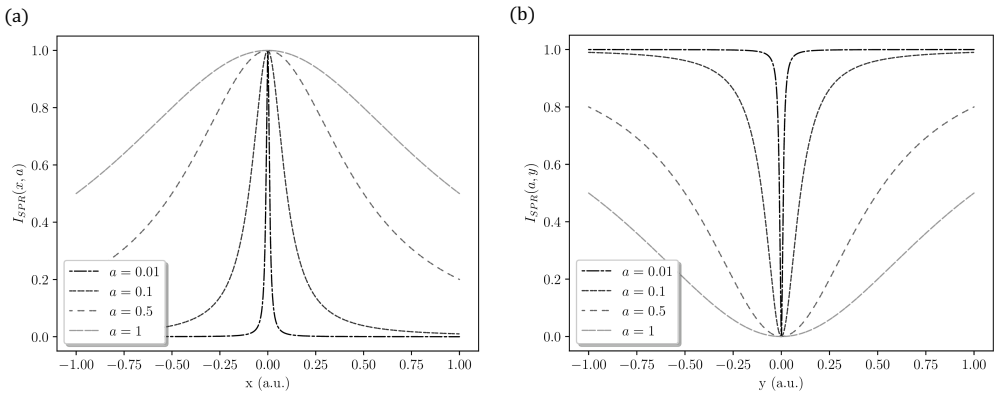

Figure 2.7: Intensity cross sections of I_{SPR} for constant y-values (a) and x-values (b)

Geometrically, Eq. 2.3.25's level curves lie on rays emanating from the origin. The origin is undefined since taking different paths towards it converge to different values as discussed previously. The discontinuous nature of the 2D-profile at the origin creates difficulty in accurately plotting a 2D contour profile. This is remedied by stitching together $I_{SPR}(x, a)$ curves as plotted in Fig. 2.7(a). The constant horizontal cross-sections are chosen equally spaced from the interval $(-1, 1)$ and later meshed into a 2D contour graphs using the Plotly library in python. Contour plots with varying incident polarization are shown in Fig 2.8.

The angle of the linearly polarized field incident on the CG should rotate the I_{SPR} profile. This is modelled as a phase shift in the argument of the $\sin^2$ function in Eq. 2.3.25 and explicitly shown in Eq. 2.3.27:

$$I \propto \sin^2(\xi + \theta_0) \tag{2.3.27}$$

Figure 2.8 shows the rotation of the I_SPR profile with varying θ_0

A second LP in series to the SPR setup is modelled using a Jones matrix of a rotated linear polarizer. Substituting the Jones matrix for a LP beam along the y-axis into Eq. 2.1.39 and operating it on the Jones vector in Eq. 2.3.23, excluding $\mathbf{E}_{NC}$ for reasons previously discussed on page 19, the following expression of the SPR field between two LP ,crossed at angle θ, is given by:

$$\mathbf{E}_{SPR,||}(\theta) = \begin{bmatrix} \sin^2\theta \sin\xi\cos\xi - \sin\theta\cos\theta\sin^2\xi \\ -\sin\theta\cos\theta\sin\xi\cos\xi + \cos^2\theta\sin^2\xi \end{bmatrix} \tag{2.3.28}$$

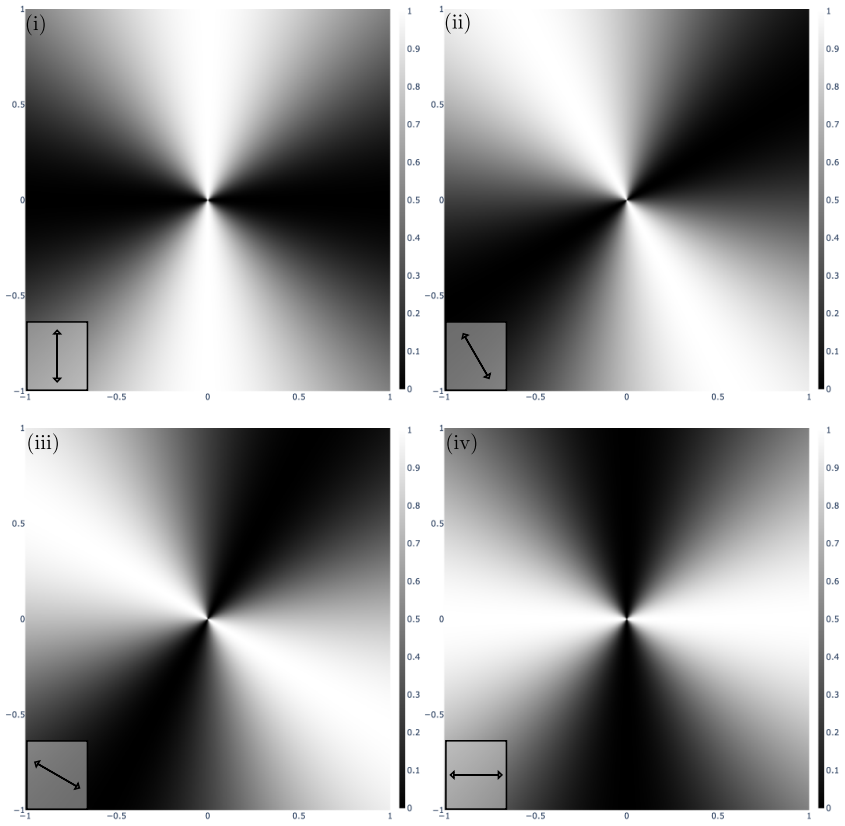

Figure 2.8: 2D contour maps of $\sin^2(\xi + \theta_0)$ with varying θ_0: (i) 0^o, (ii) 30^o, (iii) 60^o, (iv) 90^o

The following intensity relationship is derived by Substituting Eq. 2.3.28 into Eq. 2.1.19:

$$\begin{aligned} I_{SPR,||}(\theta) \propto & \sin^4\theta \sin^2\xi \cos^2\xi + \sin^2\theta \cos^2\theta \sin^4\xi - 2\sin^3\theta \sin^3\xi \cos\xi \cos\theta \\ & + \sin^2\theta \cos^2\theta \sin^2\xi \cos^2\xi + \cos^4\theta \sin^4\xi - 2\cos^3\theta \sin^3\xi \cos\xi \sin\theta \end{aligned} \tag{2.3.29}$$

The expression can be greatly simplified by considering the sum of the two lines

in Eq. 2.3.29 term by term

$$\begin{aligned}
&\sin^4\theta\sin^2\xi\cos^2\xi + \sin^2\theta\cos^2\theta\sin^2\xi\cos^2\xi \\
&= \sin^2\theta\sin^2\xi\cos^2\xi(\sin^2\theta + \cos^2\theta) = \sin^2\theta\sin^2\xi\cos^2\xi \\
&= \sin^2\theta\sin^2\xi - \sin^2\theta\sin^4\xi \qquad (2.3.30)\\
&\sin^2\theta\cos^2\theta\sin^4\xi + \cos^4\theta\sin^4\xi = \cos^2\theta\sin^4\xi(\sin^2\theta + \cos^2\theta) \\
&= \cos^2\theta\sin^4\xi \qquad (2.3.31)\\
&- 2\sin^3\theta\sin^3\xi\cos\xi\sin\theta - 2\cos^3\theta\sin^3\xi\cos\xi\sin\theta \\
&= \sin^3\xi\cos\xi(-2\cos\theta\sin\theta)(\sin^2\theta + \cos^2\theta) = -\sin^3\xi\cos\xi\sin 2\theta, \qquad (2.3.32)
\end{aligned}$$

summing together Eq.'s 2.3.30 and 2.3.31 results in,

$$\begin{aligned}
&\cos^2\theta\sin^4\xi + \sin^2\theta\sin^2\xi - \sin^2\theta\sin^4\xi \\
&= \sin^2\theta\sin^2\xi + \sin^4\xi(\cos^2\theta - \sin^2\theta) \\
&= \sin^2\xi(\sin^2\theta + \sin^2\xi\cos 2\theta), \qquad (2.3.33)
\end{aligned}$$

and finally summing the remaining term, Eq. 2.3.32 with Eq. 2.3.33 results in:

$$\begin{aligned}
&\sin^2\xi(\sin^2\theta + \sin^2\xi\cos 2\theta) - \sin^3\xi\cos\xi\sin 2\theta \\
&= \sin^2\xi(\sin^2\theta + \sin^2\xi\cos 2\theta - \sin\xi\cos\xi\sin 2\theta) \\
&= \sin^2\xi(\sin^2\theta + \sin\xi(\sin\xi\cos 2\theta - \cos\xi\sin 2\theta)) \\
&= \sin^2\xi(\sin^2\theta + \sin\xi\sin(\xi - 2\theta)) \qquad (2.3.34)
\end{aligned}$$

Substituting the trig identity, $\sin\alpha\sin\beta = \frac{1}{2}(\cos\{\alpha-\beta\} - \cos\{\alpha+\beta\})$, into Eq. 2.3.34 gives the final simplification:

$$\begin{aligned}
&= \sin^2\xi(\frac{1}{2} - \frac{1}{2}\cos 2\theta + \frac{1}{2}(\cos 2\theta - \cos(2(\xi-\theta)))) \\
&= \sin^2\xi(\frac{1}{2}(1 - \cos(2(\xi-\theta)))) = \sin^2\xi\sin^2(\xi-\theta) \qquad (2.3.35)
\end{aligned}$$

Note, the effect the second LP has on the transmission mode is identical to the SPR response on a CG from a linearly polarized field phase shifted by the angle of the LP (θ).

$$I_{SPR,\theta} \propto \sin^2\xi\sin^2(\xi-\theta) \qquad (2.3.36)$$

Graphing the intensity of a cross polarized setup ($\theta = 90^o$), using the methods previously used for Eq. 2.3.25 , the resulting intensity profile is shown in Fig. 2.9 The derivation theorizes the presence of a non-zero intensity passing through crossed polarizers at the wavelength of the SPR. By hypothesis, this is caused by the polarization conversion via SPR excitation.

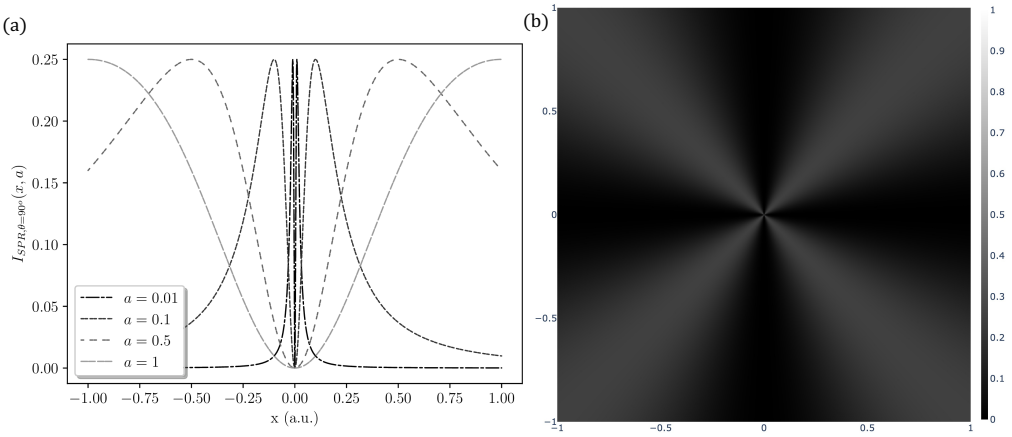

Figure 2.9: (a)Simulation of $I_{SPR,\theta=90^o}(x,a)$ for varying a, (b) 2D contour of $I_{SPR,\theta=90^o}$(x,y)

2.4 Rigorous Coupled Wave Analysis (RCWA)

The RCWA method, pioneered by M.G.Moharam and T.K. Gaylord [77], expresses a SRG's dielectric function in terms of a Fourier series expansion [78],

$$\epsilon(x) = \sum_h \epsilon_h \exp\left(i\frac{2\pi h}{\Lambda}\right), \tag{2.4.1}$$

in a region defined by the depth of the grating (d) shown in Figure 2.10. Utilizing the symmetry of the grating in the y-direction shown in Figure 2.10, the Field in the grating region betweeen Region I,II can be expressed as a sum of modes. Each mode individually satisfies Maxwell's and Helmholtz's equations, although differing polarization states have to be considered separately.

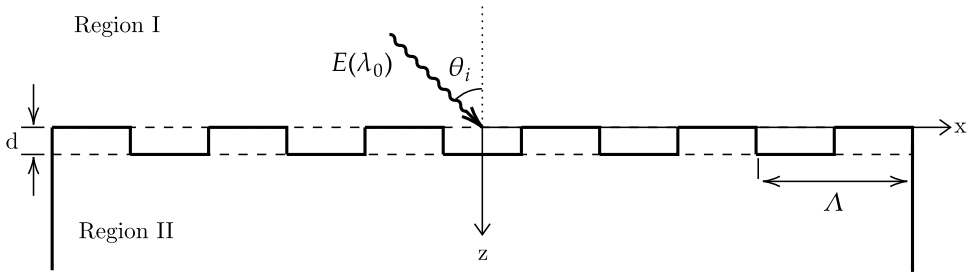

Figure 2.10: Planar diffraction model and the relevant parameters for the RCWA method: d - depth of grating, $E(\lambda_0)$ - incident electric field, Λ - pitch of grating, θ_i - angle of incidence of the electric field

Assuming separabilility of the fields in the grating region ($E(x,z) = E_x(x)E_z(z)$) the solutions for the amplitudes of the seperated modes are periodic with respect to the period of the planar grating (Λ)[79]. Maxwell's equations are used to find the auxilliary field expansion and a set of coupled equations. The set of coupled equations is expressed as a matrix and its eigenvalues and eigenvectors are numerically solved and used to form the set of equations for the field amplitudes in the grating region.The field amplitudes of the forward and back-diffracted modes are found by calculating the coupling constants in the grating region and back-substituting into boundary conditioned field equations at the grating surface ($z = 0, z = d$). The transmission diffraction efficiencies for all modes can be calculated using Eq. 2.4.2,

$$DE_{ti} = T_i T_i^* Re(\frac{k_{II,zi}}{k_0 n_{II}} \cos\theta_{inc}), \tag{2.4.2}$$

where T_i, T_i^* is the i-th transmitted diffraction amplitude and its complex conjugate respectively, and the wave vector ($k_{\ell,zi}$) in the z-direction defined via the Helmholtz equation and the boundaries of the grating region:

$$k_{\ell zi} = \begin{cases} k_0[n_\ell^2 - (k_{xi}/k_0)] & k_0 n_\ell \geq k_{xi}, \\ -ik_0[(k_{xi}/k_0) - n_\ell^2] & k_{xi} > k_0 n_\ell 0 \quad \ell = I, II \end{cases}$$

n_l is the refractive index of each region (I, II), $k_0 = 2\pi/\lambda_0$, λ_0, θ_{inc} is the incident field's wavelength in free space and the angle normal to the grating's surface respectively and the wave vector along the grating surface is given as,

$$k_{xi} = k_0[n_I \sin\theta_{inc} - i(\lambda_0/\Lambda)], \tag{2.4.3}$$

Eq. 2.4.3 is often referred to as the "Floquet Condition" in the literature [78] [79]. Exact coupled equations for multi-layered gratings [80], derived by Moharam et. al, have been used in simulation software to simulate the diffraction efficiencies

of a wide range of grating geometries[]. The convergence for accurate diffraction amplitudes are determined by the number of harmonics retained in the original dielectric function expansion in Eq. 2.4.1

Further work has been done for the numerical stability and speed of convergence of lossy materials such as metals using efficient eigenvalue and eigenvector computations[].

3 Experimental Methods

3.1 Thin Film Sample Fabrication

A Disperse Red 1 (gDR1) azobenzene + mexylaminotriazine group is synthesized according to literature [81]. The resulting powder is dissolved in a dichloromethane solution with a 3% ratio by weight. It is then pressed through a 50 μm filter to remove any large particulates. Soda lime glass slides were cut to dimension (3.5cm x 3.5cm), cleaned with a household surfactant and rinsed with warm water. The slides were hand wiped and dried with Kim wipes as to remove any remaining dust particles left on the surface. They were then oven-dried at 100 degrees Celsius for up to 15 minutes, making sure all water evaporated from the depositing surface. 3ml of the azobenzene mixture was deposited on each slide before being spun at 1000 RPM for 20 seconds. Each sample was then placed back into the oven at 85 degrees Celsius for 25 minutes to for total solvent evaporation. The temperature is optimized as to prevent a phase change in the azobenzene molecules evaporation of the thin film. To determine the thickness of the resulting films, a small scratch is made in the film and the resulting groove is measured using a Dektak Profilometer.

3.2 Interference Lithography

3.2.1 Circular Diffraction Grating Generator

Previous work accomplished the manufacturing of the CDGs, these were used throughout this project[61].

The truncated, conical surface of the polished mirror interior of the CDG, when illuminated at normal incidence with coherent beam, creates a circular interference pattern. This circular interference pattern is used to inscribe surface relief gratings on the thin films. Several variables determine the surface relief grating profile having been previously described in literature[25][82] and involve the laser irradiance on the film, time of inscription, initial depth of the film, and wavelength of the inscription source. Optimization of the gratings profile and thickness of the optically thin metallic layering is crucial to the excitation of an SPR signal. Four

CDGs were used throughout the experiment seen in the following table,with the dimensions labelled as seen in Fig. 2.4

CDG	Small Aperture (+/-0.01 mm)	Large Aperture (+/-0.01 mm)	Angle (degrees)
4	11.84	18.61	24.00
5	11.12	16.25	29.42
6	11.91	16.51	27.93
7	12.14	21.82	34.33

Table 3.1: Circular diffraction grating generator parameters

Constant and chirped gratings were fabricated using the experimental setups in Fig. 3.2 and Fig. .3 respectively.

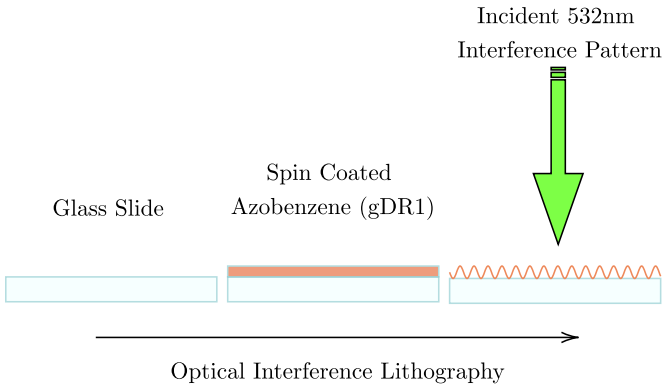

Figure 3.1: Optical interference lithography procedure

3.2.2 Circular Diffraction Grating (Constant)

In both constant and chirped setups a coherent LP beam of known wavelength is passed through a quarter-wave plate, inducing an active response in the azo films when producing SRGs. As seen in Fig. 3.2, the beam is passed through a spatial filter to smooth the beam, followed by a couple of lenses to expand and then collimate the beam, and an adjustable iris to control the spot width. The CDG is placed normal to the incident beam creating constant pitched circular gratings, since all rays have identical relative wave vectors when collimated, the interfernce pattern has a constant period.

The characteristics of the circular gratings are determined by the height and angle of the CDG[61]. If the height of the mirror section is not at a critical height h_c then the reflected wavefront does not interfere with the center of the normally

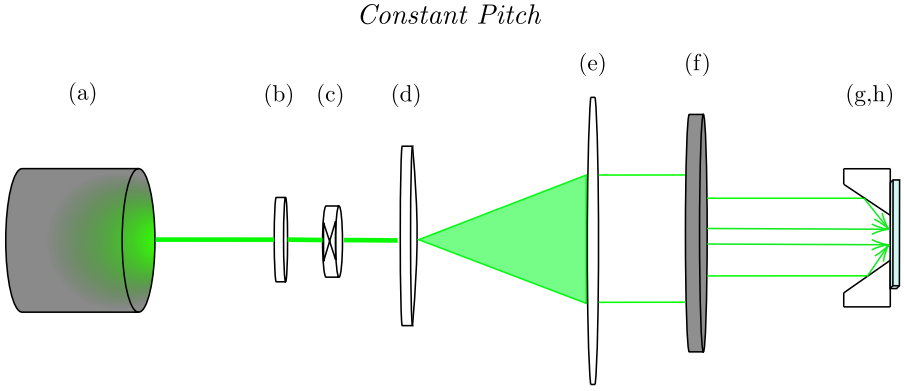

Figure 3.2: Constant pitch circular diffraction grating experimental setup - (a) 532nm Coherent source laser, (b) $\lambda/4$ wave plate, (c) Spatial filter, (d) Convex lens, (e) Collimating lens, (f) Variable iris, (g,h) CDG with affixed Azo sample

incident beam resulting in a flat intensity profile near the center, insribing only a ring of gratings. However if the height of the mirror surface exceeds the critical height then the beam interfers along the full radius inscribing gratings to the center. If the height of the CDG exceeds the critical height then by placing a paper placard in place of the sample interference area, the iris is adjusted to control the width of the beam preventing overlap across the center.

3.2.3 Grating Profile Optimization

SRG's using azo-isomerization interference lithography are dependent on both polarization and irradiance[25]. In this study, it is necessary that we make the gratings from 15nm - 70nm in depth, from peak to trough. To insure this is satisfied, each film was irradiated at $300mW/cm^2$ for times ranging between 50-100 seconds depending on the CDG and setup(constant/chirped). The variance in the timing on different CDG's likely comes from the quality of the reflective surface as the CDG's were made in house.

3.3 Surface Characterization

3.3.1 Atomic Force Microscope Imaging

The primary instrument used in profiling the depth and character of the SRGs was an Atomic Force Microscope (AFM). The AFM uses a rigid metal tip to track the surface level of the sample in combination with a laser scattering interpolation

software programmed by the manufacturer (Bruker). The software contains a viewing window to analyze the 2D surface image. Scans of 5um x 5um ,10um x 10um were taken on various areas of the samples. Taking scans 1-5mm from the center with increments of 1mm along the 0,90,180,270 degree directions of the grating. Averaging is done on the cross section of the grating along the entire scan to reduce errors on the grating depth measurements. A Fast Fourier Transform is automatically performed on the averaged cross section and a manual measurement is also performed by counting the periods spanned by the scan and using this integer to divide the horizontal distance measured by the Bruker software.

3.4 Metal Deposition

A Quorum Technologies sputter coater deposited 50nm of gold on the SRG samples as shown in Fig. 3.3. The thickness of the metal is chosen to be optically thin but still thick enough to induce a substantial SPR signal. The confirmation of the thickness of the metallic layer is done by making another scratch through all layers of the film and measuring the depth using the DEKTAK Profilometer and finding the difference between the film thickness and the measured metal-azo thickness.

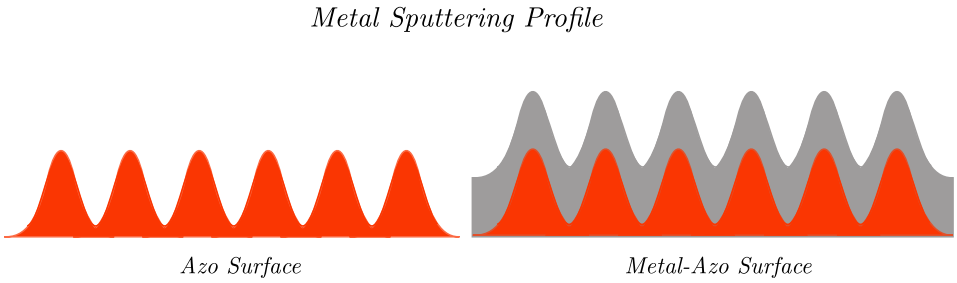

Figure 3.3: Cross-section of a grating with and without layer of metal (*Note: Thickness of films not to scale*)

3.5 Surface Plasmon Spectral and Polarization Sampling Methods

Experiments were conducted on the transmitted and reflected fields of the circular diffraction gratings, to validate both the presence and polarization of the SPR.Spectra and Polarization measurements were taken using multiple optical setups.

3.5.1 Spectroscopy Imaging - Transmission/Reflection

An Incandescent source light contained in a housing unit, Fig. 3.4, is used for a broad spectrum driving field on the grating. The source output is directed at a concave mirror and redirected around a large rectangular panel through an adjustable circular iris. The iris determines the focused beam size directed onto the sample. A neutral density filter attenuates the field so that spectroscopic sensor doesn't become saturated. The light is focused on the sample and subsequentially through a final focusing lens into an optical fiber leading to the Ocean Insight Spectrometer measuring the spectrum and where OceanView software records the measurements. The Vis-NIR detector operates under specification within a range of 350-925 nm wavelengths, splitting the light via a broad spectrum grating and passed onto an air-cooled 1024 x 58 CCD pixel array.

Two methods are used when measuring a reference throughout the various measurements. When the beam width covers the entire grating surface the reference used is a flat metal film of equal thickness. A single linear polarization cannot be used globally over a 'large' section of the circular grating as is performed with linear gratings Fig. 3.6. If the beam width is taken on a 'small' area of the grating where the curvature of the grating is large then a single LP can be used as the reference orthogonal to the grating vector.

Using a grating-diameter width beam of the source light in Fig. 3.4, the SPR signal was measured in transmission with varying relative LP angles, where the sample was rotated on an optical fixture by various angles. This was to emulate the rotation of polarization while holding the Intensity constant, since the measured source was elliptically polarized causing a systematic error in the observed spectra that is otherwise prevented by rotation of the symmetric grating.

3.5.2 Intensity-Polarization SPR Imaging

In characterising EM radiation, the defining observables of the beam include the Frequency, Intensity, and Polarization. Frequency-Intensity measurements use gratings combined with calibrated CCD sensors to accurately determine the intensities of a range of frequencies in spectroscopy. The downside is a loss of spatial information as the spectroscopic measurement is simply taking a global measure-

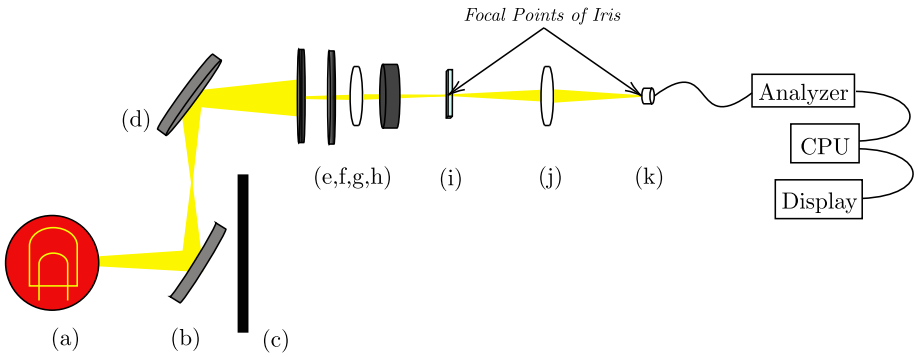

Figure 3.4: Spectroscopic experimental setup in transmission - (a) Incandescent source light,(b) concave mirror, (c) source shield,(d) flat mirror,(e,f,h) variable iris, neutral density filter, birefringent polarizer, (g,j) lens, (i) sample, (k) optical fiber

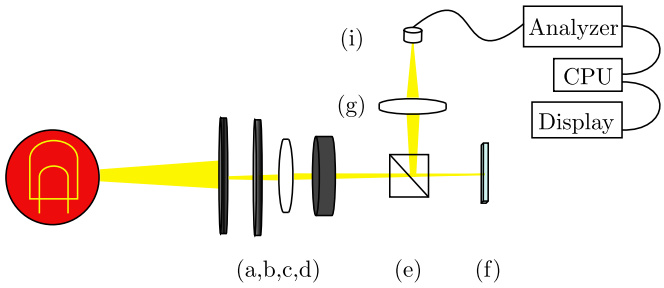

Figure 3.5: Spectroscopic experimental setup in reflection - (a,b,d) Variable iris, neutral density filter, birefringent polarizer (c,g) lens, (e) beam splitter, (f) sample,(i) optical fiber

ment from a focused field.

An industrial use Ueye CMOS camera, in series with a Liquid Crystal Tunable Filter (LCTF) (THORLABS KURIOS-WL1)in Fig. 3.7, captured images of the transmission intensities of various gratings over a range of optical frequencies. The CMOS camera preserves spatial intensity information, important when preserving polarization information. The LCTF is designed to selectively transmit a narrowband frequency of light from the incandescent source used in the spectro-

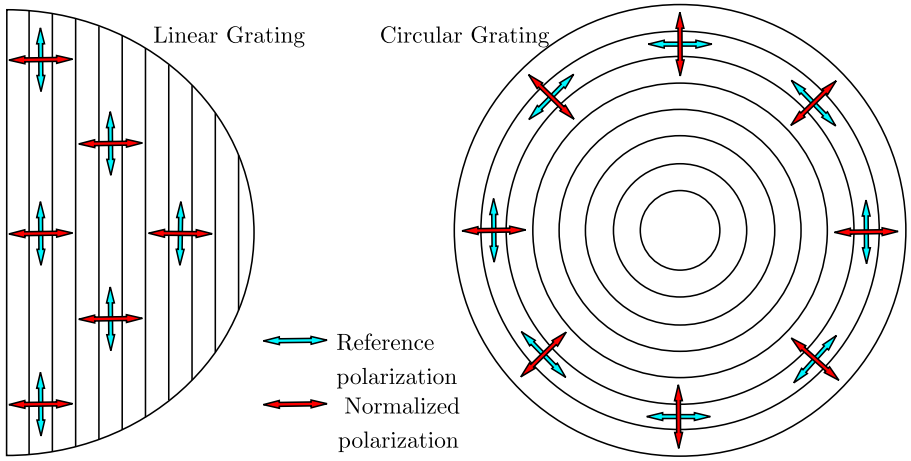

Figure 3.6: Comparison of reference polarizations between linear and circular gratings

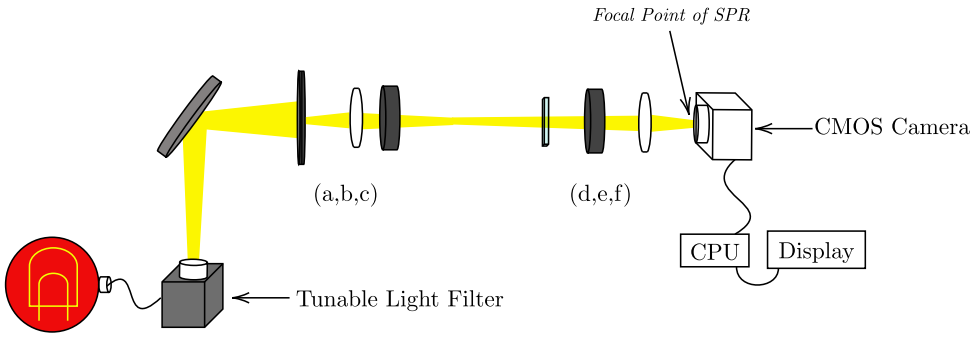

Figure 3.7: Cross polarization experimental setup in transmission - (a) Variable iris, (b,f) lens, (c,e) birefringent polarizer, (d) sample

scopic analysis. As seen in data recorded by THORLABS in Fig. 3.8 the LCTF has increasing frequency bandwidth and Intensity profiles at different centered transmission wavelengths.

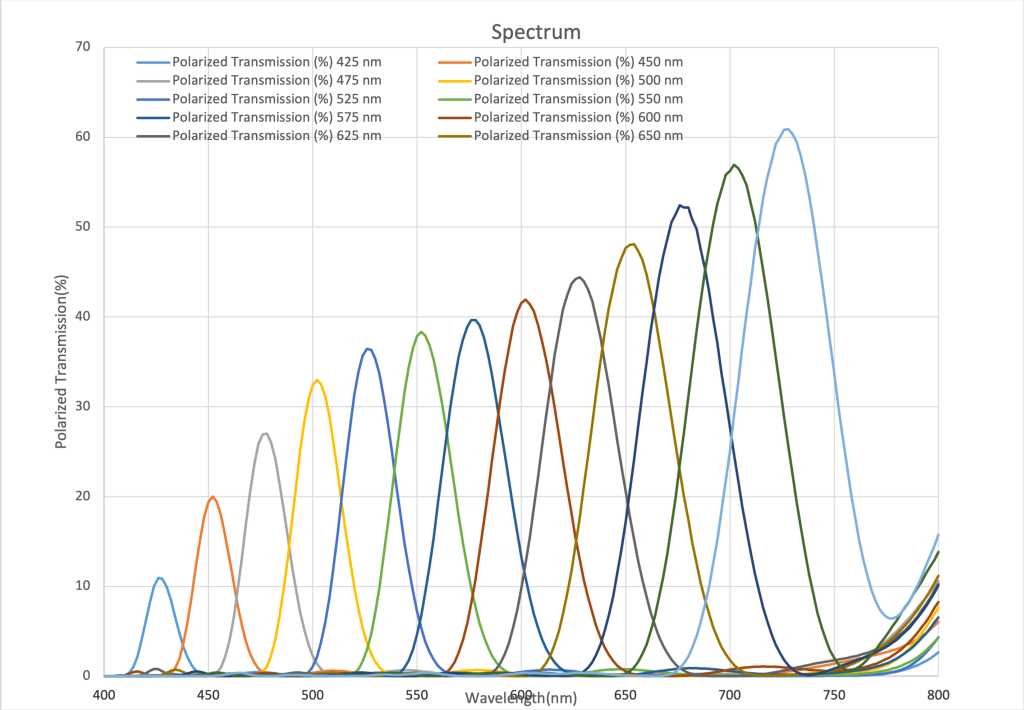

Figure 3.8: Thorlabs transmission data of the KURIOS-WB1 Liquid Crystal Tunable Filter centered on various transmission peaks labelled in the legend.[83]

3.6 Radially Polarized Source and Exciting Surface Plasmons

A near-lossless Radial Polarization Converter (RPC), used in this experiment, developed by ARCoptix is capable of transforming a linearly polarized coherent beam into a continuous radial or azimuthal polarization distribution. Linearly polarizing a 4mW He-Ne laser and collimating the beam in Fig. 3.9 are necessary for the RPC,with a secondary linear polarizer on the backside of the radially/azimuthally converted beam to analyze the intensity distribution. The RPC has an Inductor-Capacitor driver to output a variable square amplitude at 1.6 KHz with polarity inversion, supplying the variable phase retarder for conversion of different wavelengths[53]. Another output is also used on the LC driver for the Twisted Nematic (TN) cell to switch between Azimuthal and Radial polarization[53]. As seen Fig. 3.6 the 'reference' is identical to an Azimuthal Polarization centered on the circular grating and the 'normalized' beam, identical to a Radial Polarization.Using the RPC in combination with a CMOS camera in Fig. 3.9,images were captured in transmission with both Azimuthal and Radial polarizations on a circular grating with a SPR signal at the wavelength specified.

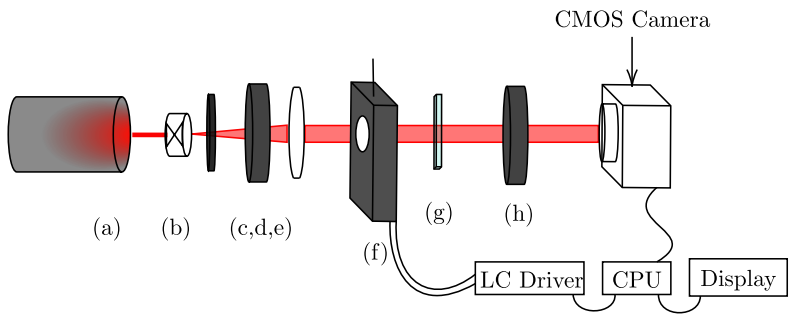

Figure 3.9: Radial polarizer SPR sxcitation experimental setup - (a) He-Ne 632 source laser, (b) spatial filter, (c) neutral density filter, (c,h) birefringent polarizer, (e) lens, (f) TN radial polarization converter, (g) sample

Removing the RPC, the intensity profile transmission between cross polarizers is captured with both the He-Ne setup and with the previously discussed LCTF setup.

3.6.1 Polarimetry

A PAX1000VIS THORLABS Polarimeter digitally analyzes the polarization of a source at a singular wavelengths between 400-700 nm. A rotating quarter wave plate,fixed LP and a photodiode in series. A fast fourier transform (FFT) is performed on the measured photocurrent measuring the Stokes Vectors and outputing the measurements as a point on the Poincare sphere[84].

The Polarimeter was used as a polarization confirmation from the RPC and to measure the ellipticity of sources.

3.6.2 Diffraction Grating Analysis Software

GSolver, a diffraction grating simulation software, was used in optimizing the thickness of the metal film and depth of the gratings. The RCWA technique uses a Fourier expansion of the dielectric function for an interface and calculates the corresponding fields with respect to the boundary conditions. The construction of a single period of the grating is made through a graphical software interface. The software has data for the dielectric permittivity for Gold, and a constant value for the azo-film dielectric function is used.

GSolver simulates incident fields with any polarization on the Poincaré sphere over a range of frequencies, and a normalized transmission TE/TM graph is simulated for various pitches.

4 Results and Discussion

The experimental results recorded in this chapter were by means of the methods outlined in Chapter 3. The goal was to produce and identify an SPR excitation via unpolarized light on a large aperture circular diffraction grating. The polarization dependent SPR excitation corresponds to a polarized SPR mode with intensity enhancement or absorption in transmission and reflection respectively, as understood by the theory outlined in Chapter 2.

The thickness of the azo-films were measured at approximately $300 \pm 20nm$ in depth. The pitch and depth of the grating are independent parameters of the SRG, the prior modulated by the nominal angle of the CDG, and the latter optimized with the laser irradiance value and duration of inscription. Manufacturing of the CDG's requires precision milling and polishing with fixed angles. The choice of pitch is limited to the wavelength of the inscription sources and the choice of CDG in Table 3.1. Using the measured nominal angles of each CDG, the expected pitch of the inscribed SRGs with various inscription wavelengths were calculated using Eq. 2.1.60. Scans with area 10x10μm ranging from 2500-5000 μm from the center were used to measure the pitch of the SRGs. The averages across all scans are presented in Table 4.1 presented with the theoretical values for the corresponding CDG nominal angle, where the theoretical values are obtained using Eq. 2.1.60.

CDG Angle (Degrees)	Inscription Wavelength (nm)					
	488		514		532	
	Theo.	Exp.	Theo.	Exp.	Theo.	Exp.
16.25	570	583	600	598	622	623
16.51	589	581	621	617	642	668
18.61	657		692		716	717

Table 4.1: Experimental vs.Theoretical Values of constant pitch inscription for differing CDG angles and varying inscription wavelengths

The theory outlining the coupling of SPs in Chapter 2 assumes a constant grating vector magnitude with symmetry along a single dimension on the grating surface. For non-linear gratings, specifically in the case of circular gratings, the

grating vector has a 2D spacial dependency as seen in Eq. 2.3.20. Moreover, a constant pitched CG has a constant GV magnitude with circular symmetry, such that the vector field associated with the GV has a source point centered on the axis of symmetry. Exciting SPs locally on a CG, where the curvature of the grating is small relative to the pitch, the grating vector can be approximated as linear with small incident beam widths. The approximation was used throughout the preceeding theory, and will be assumed throughout the following discussion.

4.1 Surface Fabrication and Characterization

In previous literature, inscribing the SRGs using an azobenzene film involves a Lloyd mirror setup seen in Fig. 4.1.

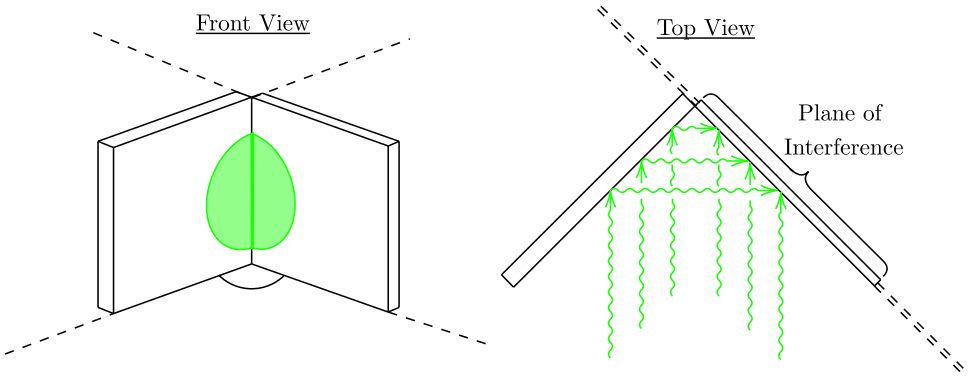

Figure 4.1: A diagram showing the geometry of a Lloyd mirror with an incident inscription beam.

In the Lloyd mirror setup under a collimated beam of constant irradiance, a unit area of reflection has a constant interference area on the film irrespective of the location on the reflective surface. In other words the intensity profile on the film, under constant irradiance conditions, will be constant on the inscription area. In contrast, the geometry of a CDG does not have this property as illustrated in Fig. 4.2

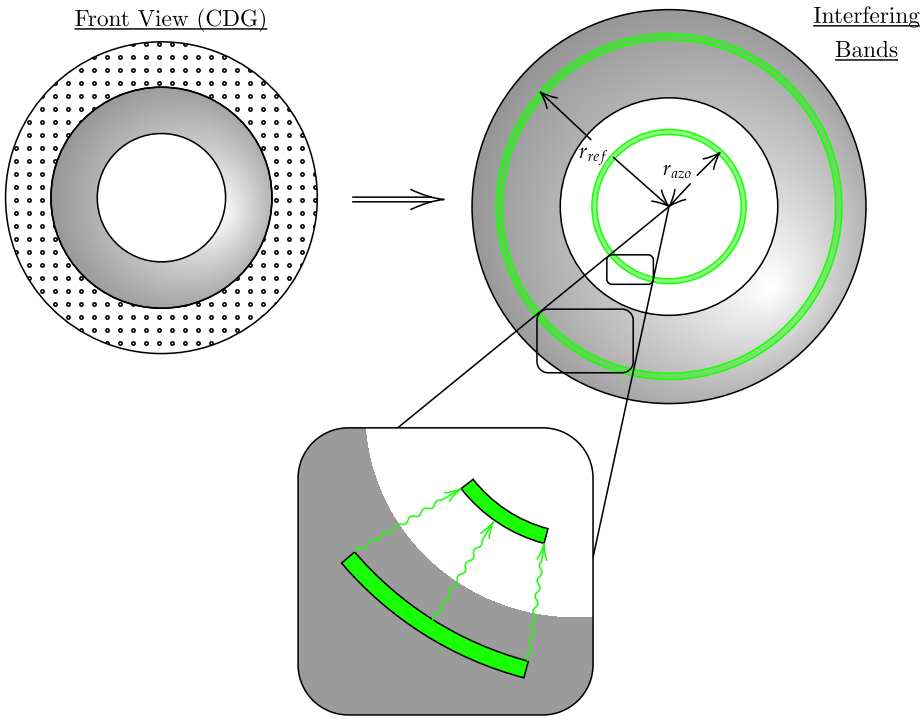

Figure 4.2: A diagram showing the geometry of a CDG with an incident inscription beam.

A ring with radius larger than the small aperture of the CDG reflects to a ring of smaller radius at the film's surface. Under geometric conditions imposed by the width of the incident beam, the reflection at the beam edge is focused at the center, where the beam width is adjusted for full circular gratings. The proximity of the reflected rings to the small aperture of the CDG corresponds to the level of focusing of the ring. That is to say under the assumption of an incident beam with constant irradiance, the presence of complete destructive interference occurs only at the boundary of the small aperture. This is relevant since the photoreactive response of the azopolymer is dependent on both the polarization and intensity profile in the film. With this in mind, it is expected that the growth rate of the SRG inscribed on a CDG will vary depending on the distance from the center of the CDG.

As seen in Fig. 4.3, the depth of the circular gratings along rays extending out from the center were found to have an increasing depth from the center out towards the edge of the grating. This can be explained by the focal geometry of the CDG apparatus. Moreover, it is understood that the CDGs are not ideal conical surfaces, and defects with size appreciable to the wavelength of the inscription

beam (λ_i) will perturb the reflection and in turn create unexpected inteference on the film. Since the creation of SRGs via azopolymer films is not fully understood, the underlying depth variability observed could also be of unknown large scale processes. Consider a system of rings for the grating inscription as seen in Fig. 4.2. A focused reflected ring slice with angle $d\theta$, has an infitesimal area $r_{ref}drd\theta$, $r_{azo}drd\theta$ for the reflected ring and film ring respectively, where r_{ref},r_{azo} is the radius of the reflected ring and interference ring of the corresponding reflected ring on the azo film. Since $r_{ref} > r_{azo}$, it is clear that an integration over the rings will produce a larger irradiance for the reflected ring ($I_{ref} > I_{azo}$). This discrepancy in the Irradiance theoretically reduces to zero as the radius' converge to the limit at the edge of the small aperture.

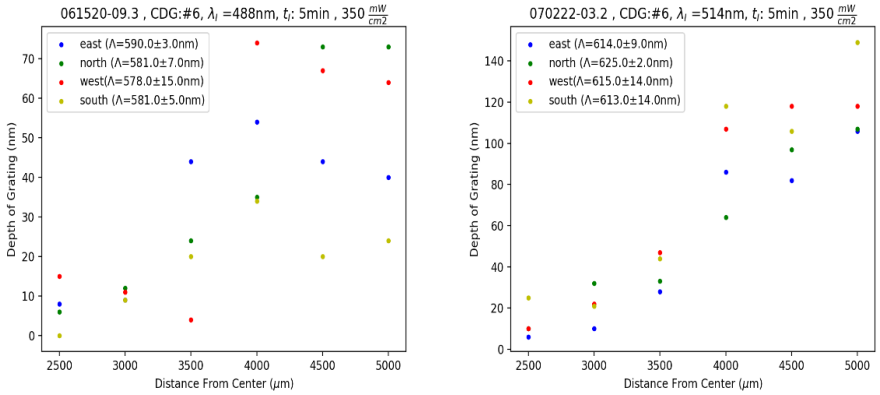

Figure 4.3: Depth of grating across rays of circular gratings

Figure 4.4 shows an example of surface scans and some single cross sections to illustrate the depth-radius positive correlation along a single ray. A closer look at the scans, it is clear that the structure becomes less uniform near the edge of the grating, where the rings as proposed should interfer with most nullification of the field. This is due to edge effects from manufacturing of the CDG and the scattering from small defects.

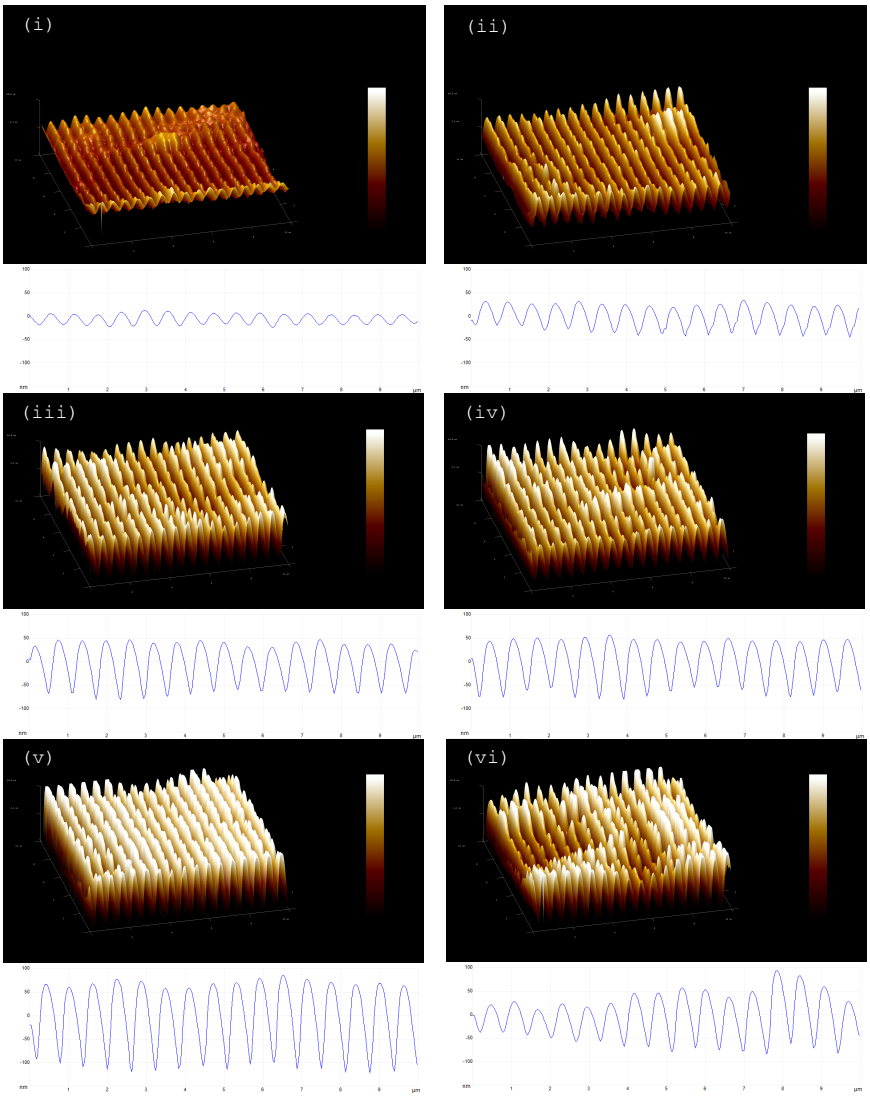

Figure 4.4: Sequence of AFM surface scans ($10\mu m$x$10\mu m$) of a CG inscribed with 514nm wavelength laser light. The scans were taken along a single ray with inscreasing distances from the center: (i)$2500\mu m$, (ii)$3000\mu m$, (iii)$3500\mu m$, (iv)$4000\mu m$, (v) $4500\mu m$, (vi)$5000\mu m$. Note: All graphs share common colour and axis scales

4.1.1 Circular SRG Center Profile

The CGs fabricated in this project used a beam width, adjusted in size for inscription to the center of the CDG. It is important not to use a beam width greater than this as to avoid unexpected interference across the center of the grating center. All inscriptions caused the following effect on the film as seen in Fig. 4.5. These ray formations could be occuring, via unexpected reflections from the surface of the mirror. The surface near the center has topological features that are larger than the AFM can measure, in the order of $1\mu m$. This is particularly exceptional since the thickness of the pre-irradiated film was roughly 300 nm thick. This implies that the azoglass is congregating near the center of the inscribed grating with around 3 times the thickness of the original film. The dominant topological features less than 1mm from the center are the structures observed in Fig. 4.5 with no discernable SRG formation. Surface profilometer scans were taken in Fig.'s 4.6, showing a significant 'mountain' of azo at the center of the inscribed area. Figure 4.7 shows another profilometer scan in which a newly spin-coated and dried azo film was scratched and scanned to confirm the thickness of the azo-film; showing the thickness to be around 300 nm.

The mountain deformation could be from some diffraction effects from the iris used to control the beam width, in which case there would be unexpected reflections directed at the center of the fixture. The focus of the beam at the center has the largest irradiance interference gradient and any imperfections of the CDG surface would cause the inscription of unexpected features on the azo surface, also supressing the formation of regular gratings. These center features of the fabrication process will be discussed later in terms of suppressing SPR excitation.

The irradiated azo-film congregates a bulk of the glass molecules, moving significant mass into localized areas of the film. Specifically, the focal center of the CDG centered on the small radius, is a point (area; although quite small) in which a caustic is formed. In other words the center when irradiated with a normal beam of sufficent radius is a ray singularity. The field dynamics is choatic and any sort intensity analysis will have some asymptotic feautures; in which the azo-film is experiencing under irradiation.

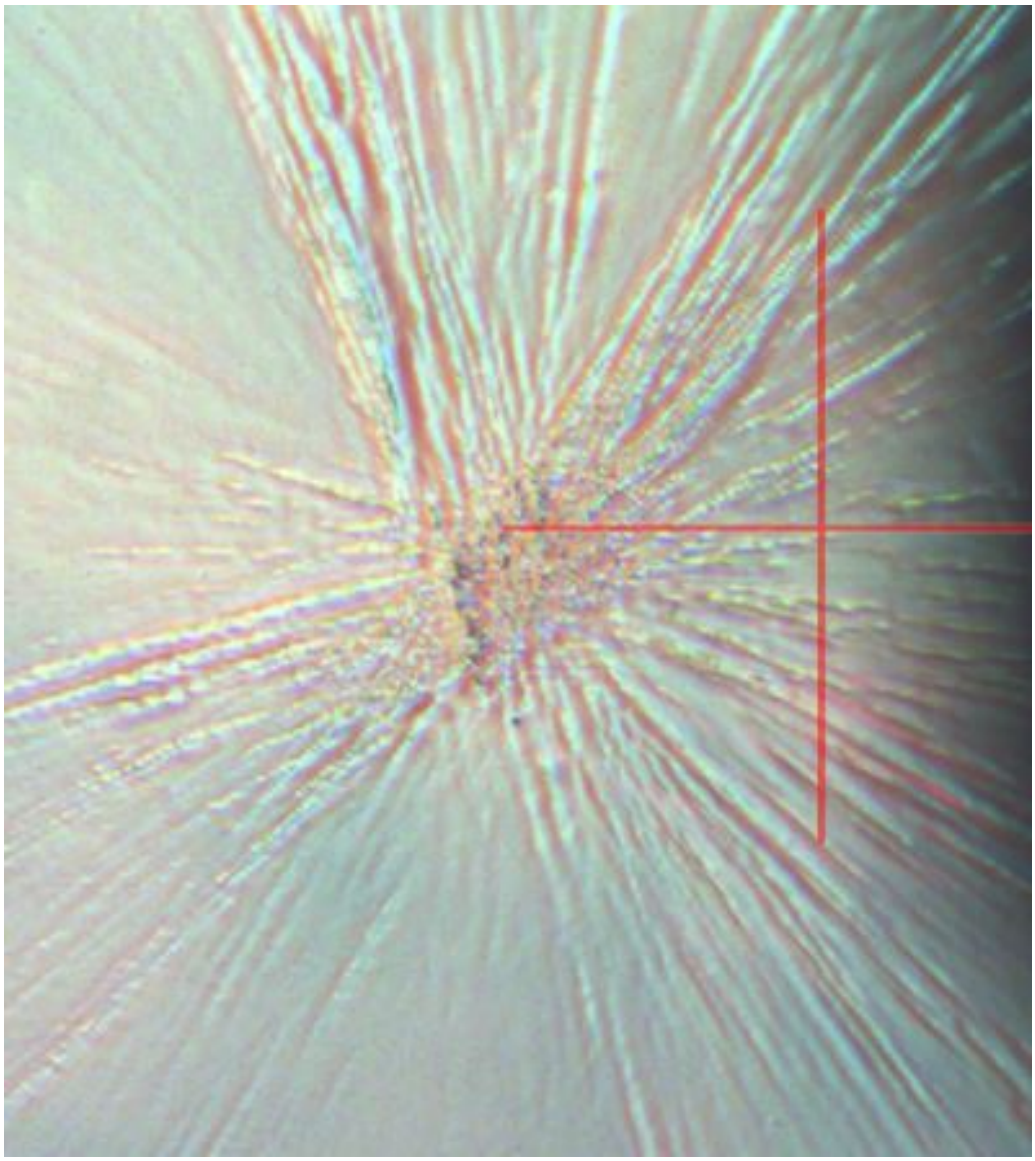

Figure 4.5: Picture of the surface of an azo-film CG using the camera on the AFM, where the center of the configuration is deformed after inscription.

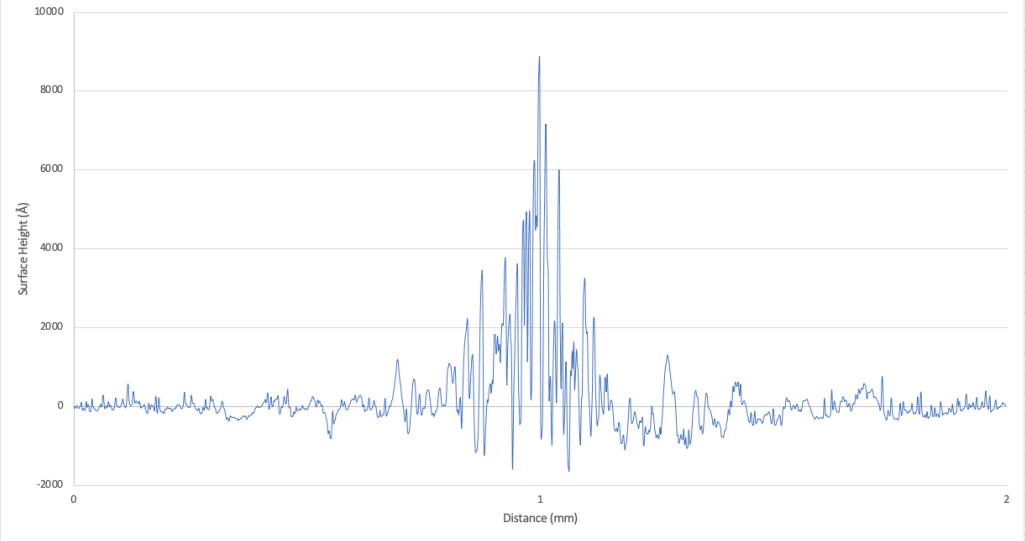

Figure 4.6: Surface profile of the center of a circular grating inscribed by a CDG. The measurement was made using a DEKTAK Profilometer.

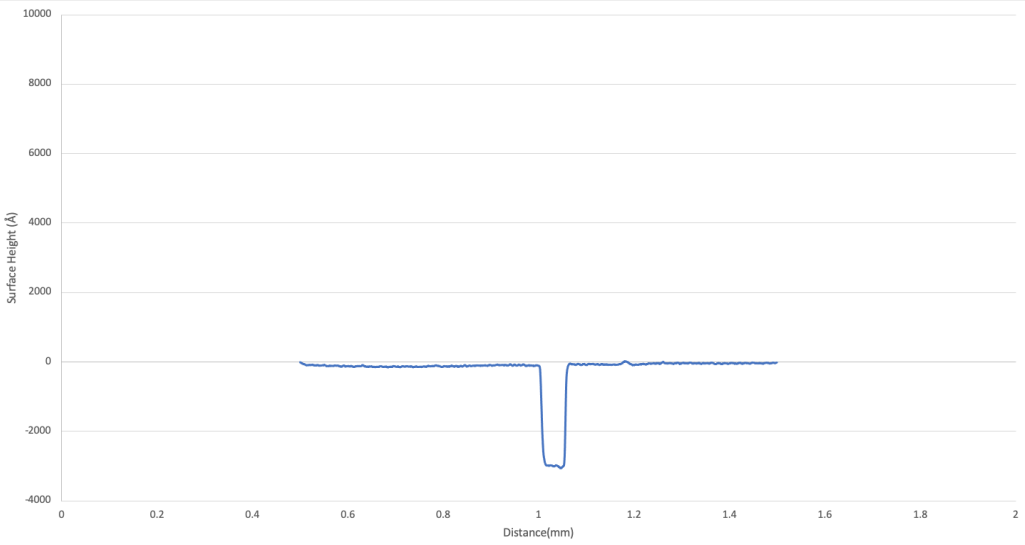

Figure 4.7: Surface profile of a ∼300 nm thick azo-film with a scratch mark in the center. The measurement was made using a DEKTAK Profilometer and before inscription with the CDG.

4.2 SPR Excitation

As seen in Eq. 2.3.18, the excitation of an SPR mode, on a linear grating with a sufficiently 'flat' surface, is dependent on the real components of the relative permittivity of both media constituting the surface, the pitch of the grating, and the angle of incidence with respect to the normal of the surface.

The relative permittivity of air will be set to $\epsilon_{r,d} = 1$ for all frequencies, and the relative permittivity of gold is obtained from measurements of a thin film (Yakubovsky et al. 2017: 50-nm film). The permittivity of gold varies over the frequency domain and thus over the corresponding wavelengths. According to the data set measured by Yakubovsky et al., the relative component of the permittivity at 500nm and 900nm are $\epsilon'_{r,m}(\lambda = 500\text{nm}) = -2.8159$ and $\epsilon'_{r,m}(\lambda = 900\text{nm}) = -36.162$ respectively. When calculating the expected resonance wavelength using Eq. 2.3.18, the relative permittivity of the gold film will be set to a constant measured value, $\epsilon'_{r,m}(\lambda = 632\text{nm}) = -12.797$. The expected SPR wavelength at normal incidence ($\theta_i = 0$), is given by the linear relationship with respect to the pitch of the grating:

$$\lambda_{SP} = 1.04\Lambda \tag{4.2.1}$$

Table 4.2 shows the expected theoretical maximum of the SPR signal using Eq 4.2.1.

CDG Angle (Degrees)	Measured Pitch with 532 nm inscription wavelength (nm)	Theoretical SPR Wavelength (nm)
29.4	623	648
27.9	668	694
24.0	717	746

Table 4.2: Theoretical values of the SPR signal of varying pitched linear gratings inscribed with a 532 nm source and $\epsilon'_{r,m} = -12.797$

The CGs have a large aperture ($\approx 1cm$) such that the curvature of the gratings over the majority of the grating should produce an SPR signal approximately at the linear grating prediction in Table 4.2. Using the transmission spectroscopy setup described in Chapter 3, a series of normalized measurements are graphed for each CG. It is important to note, that for any broad spectrum incident beam that covers the entire grating surface, a divergent beam is used, such that the incidence angle is only going to be equivalent to zero along the optical axis. Specifically, the surface plasmon wavelength is dependent with regard to the radius of excitation and the distance from the focalized beam as visualized in Fig. 4.8

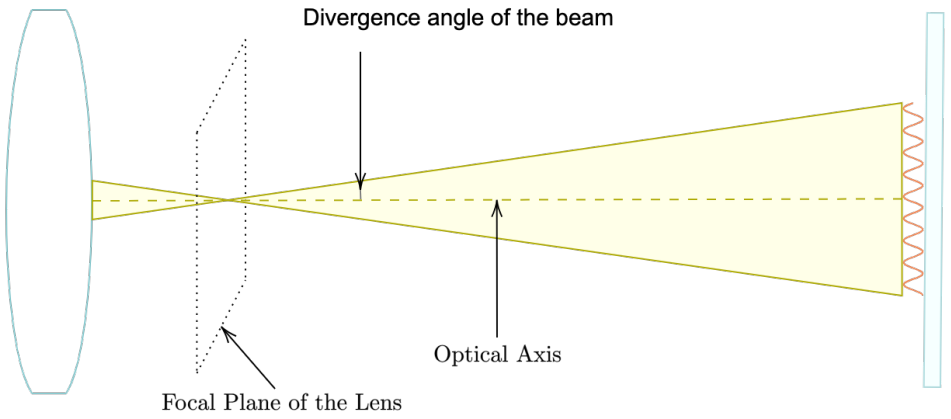

Figure 4.8: Diagram showing the physical setup of the fully irradiated grating. Note the grating surface is not a true depiction of a cross section of a circular grating

4.2.1 SPR Excitation via Linear Polarization on Circular Gratings

When exciting an SP mode on the surface of a metallic grating, a component of the polarization needs to be in the direction of grating vector. It is not necessary that the electric field oscillates solely in the direction of the grating vector but that there is a non-zero projection onto the grating vector. Fig. 4.9 shows a representation of the orientation of the beam, and its polarization on the CG when observing the transmission signal. The labels describe the positioning of the source beam (red) and the projection of the electric field with respect to the grating vector at the center of the beam. Consider the orientations shown in Fig. 4.9, it is hypothesized that the centered beam would produce a transmission SPR signal greater in intensity than the off-center orientations. When centered the source beam is covering the entirety of the grating surface and should couple to the SP mode where the grating vector is parallel (or has a component parallel) to the polarization. Specifically, by the geometry of a circle, there should only be two rays from the center of the CG (in this case, the horizontal rays) which do not couple to the SP mode. During the experiment, the normalization process was performed only once when measuring the transmission spectra of all concerned orientations in Fig. 4.9, therefore the average intensity of the source light is static and the variations in the measured signal come from the interactions of the SPR into the far-field transmision measurements. However, an unexpected observation was found in the transmission spectra of the CGs graphed in Fig.'s 4.10 - 4.12.

The observed transmission spectra and the peaks of each in Fig.'s 4.10 - 4.12 coincide with the theoretical SPR wavelength, providing confidence that the inten-

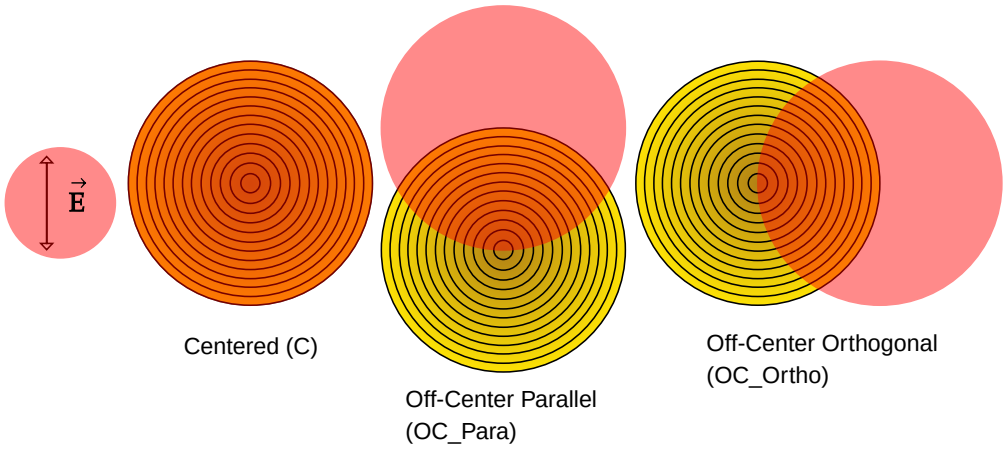

Figure 4.9: Diagram showing physical setup and nomenclature of the linearly polarized

sity enhancement observed is a result of an SPR excitation. When using a linearly polarized beam on the CGs, it is seen that the greatest intensity of the SPR signal occurs when the beam is off-center parallel. As was discussed in Chapter 2, the electric field's component parallel to the GV excites an SPR signal, and therefore in an ideal setting the total intensity enhancement should be proportional to the projection of the electric field onto the grating vector. It is expected that the off-center parallel spectrum would have a larger transmission peak at the SPR wavelength than the off-center orthogonal spectrum's transmission peak, since the sum of the total projection of the electric field onto the GV is greater in the off-center parallel orientation. Under this hypothesis the centered beam over the CG would produce an even larger transmission peak, since the exposed grating vector with a component parallel to the electric field is larger. However this is contrary to what is observed in Figures 4.10- 4.12. We expect to have around twice the transmission intensity enhancement on the centered beam as in the off-center parallel beam, as there is roughly twice the coverage of the pump beam for the centered geometry. The observed peak transmission signals of the beam placements are seen in Table 4.3.

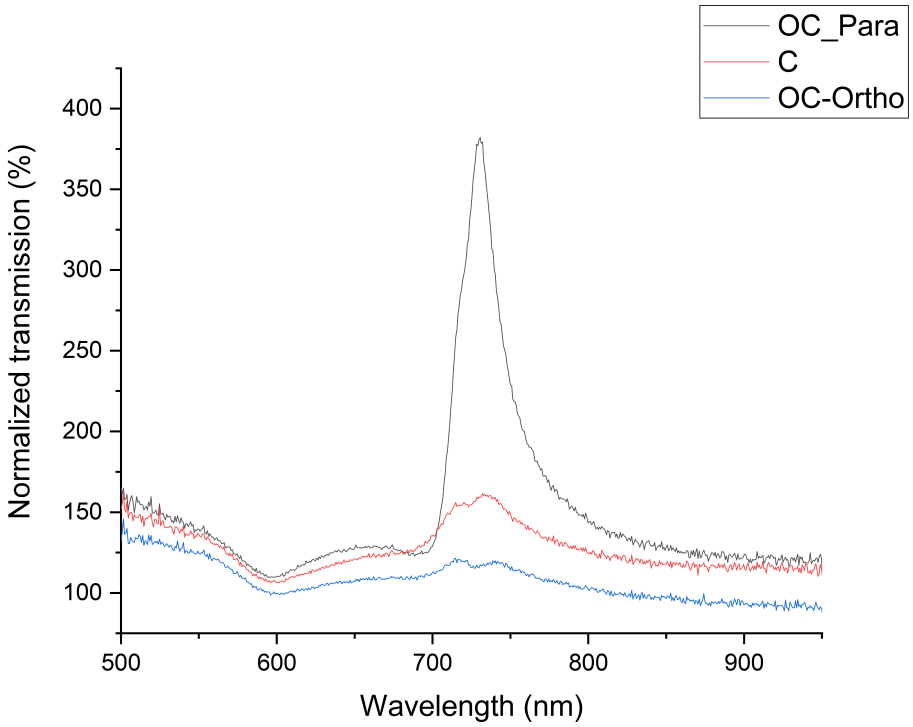

Figure 4.10: Normalized transmission spectra of a CG ($\Lambda = 717$nm) with varying LP beam orientations

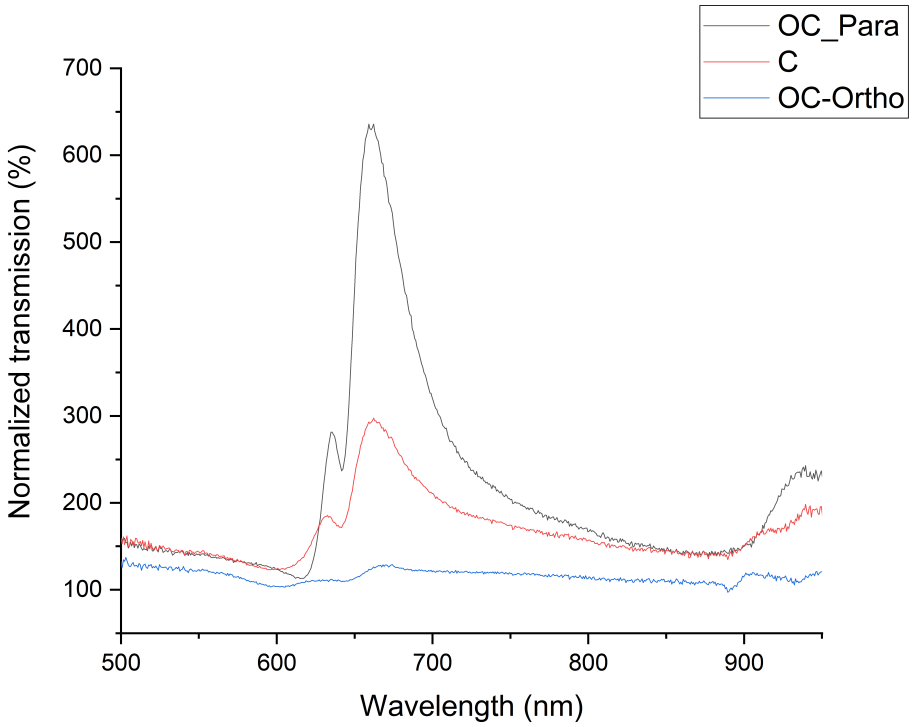

Figure 4.11: Normalized transmission spectra of a CG ($\Lambda = 668$nm) with varying LP beam orientations

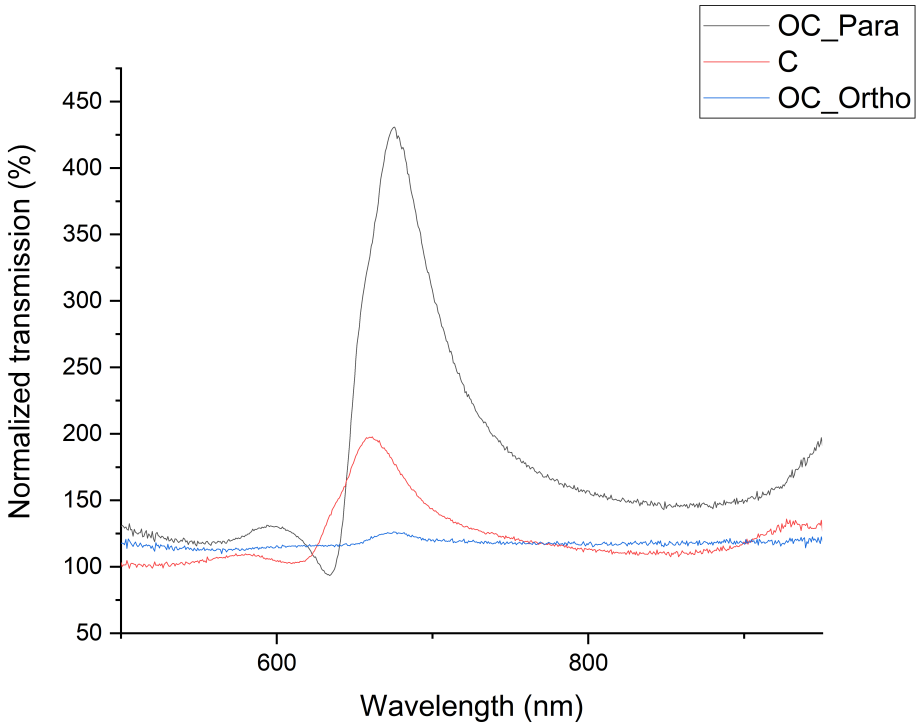

Figure 4.12: Normalized transmission spectra of a CG ($\Lambda = 623$nm) with varying LP beam orientations

CDG Angle (Degrees)	Normalized Peak Enhancement (%): OC_Ortho	Normalized Peak Enhancement (%): OC_Para	Normalized Peak Enhancement (%): Center	Center/OC_Para Ratio
16.25	126.18	430.76	176.65	0.41
16.51	126.47	635.89	297.55	0.47
18.61	117.47	382.24	159.21	0.42

Table 4.3: Table of the normalized peak values at the SPR wavelength and the ratio of the transmittive enhancement across differing CDGs.

The ratio (Center/OC_Para) in Table 4.3 shows a consistent relationship between the two coverages and their corresponding SPR transmission peak. The centered coverage is seen to transmit the SPR signal at roughly 40% of the efficiency as the off center parallel coverage. This can be explained by a couple of features related to the geometry and surface irregularities of the surface. The SPR excited on a diffraction grating has two propagative modes, forward and backward via the corresponding diffraction orders shown in Eq. 2.3.18. The mountain

structure at the center of the CG, could be causing some destructive interference between the propagative modes. The SPR mode propagates along the surface on the order of micrometers from the area of irradiance from the pump beam. This discredits the idea that there is some destructive intereference happening with the SPR mode directly since the mountain features size is in the order of milimeters. Potentially within the far field radiation the SPR field is destructively interfering and supressing the transmission spectrum. This could be studied further by irradiating the CG with a ring beam instead of a full disk. This would preclude the irradiation of the irregular mountain surface at the center of the grating. SPR transmission spectra could also be studied on smaller sections of the CG so as to find some average over the entire CG. The CGs could also be fabricated as ring SRGs by changing the width of the inscription beam, preventing the large irregularity of the surface towards the center to compare the peak SPR transmission enhancement over the varying positionings of the pump beam.

The set of contour graphs in Figures 4.13- 4.15 show the transmission spectra of the CGs with varying angles of a linearly polarized centered beam at normal incidence. The in-plane axes of the graph are the transmission wavelength spectrum and polarization angle of the incident beam, where the contour axis represents the normalized intensity of the beam. The contour graphs show a generally unshifting SPR peak at the expected wavelength corresponding to the measured pitch.

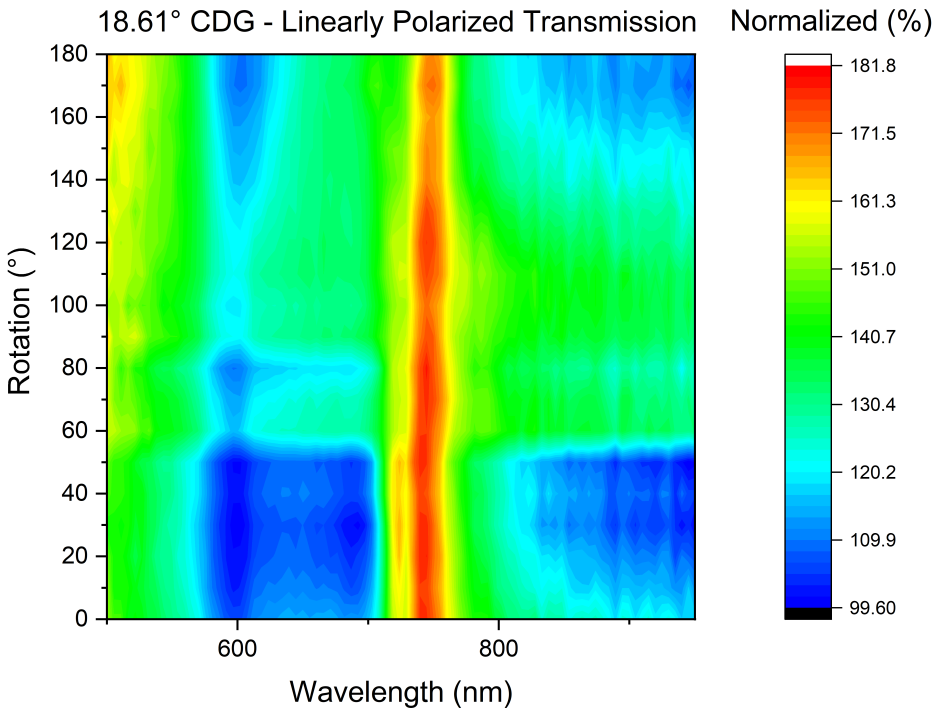

Figure 4.13: Normalized transmission intensity contour graph of a CG with $\Lambda = 623nm$ at varying linear polarization angles

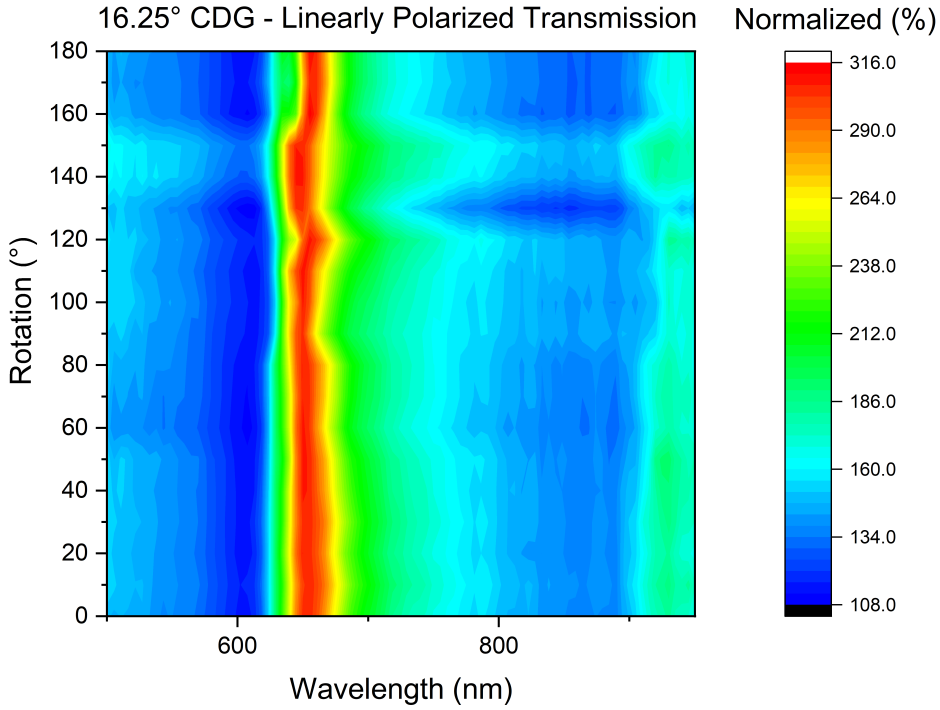

Figure 4.14: Normalized transmission intensity contour graph of a CG with $\Lambda = 668nm$ at varying linear polarization angles

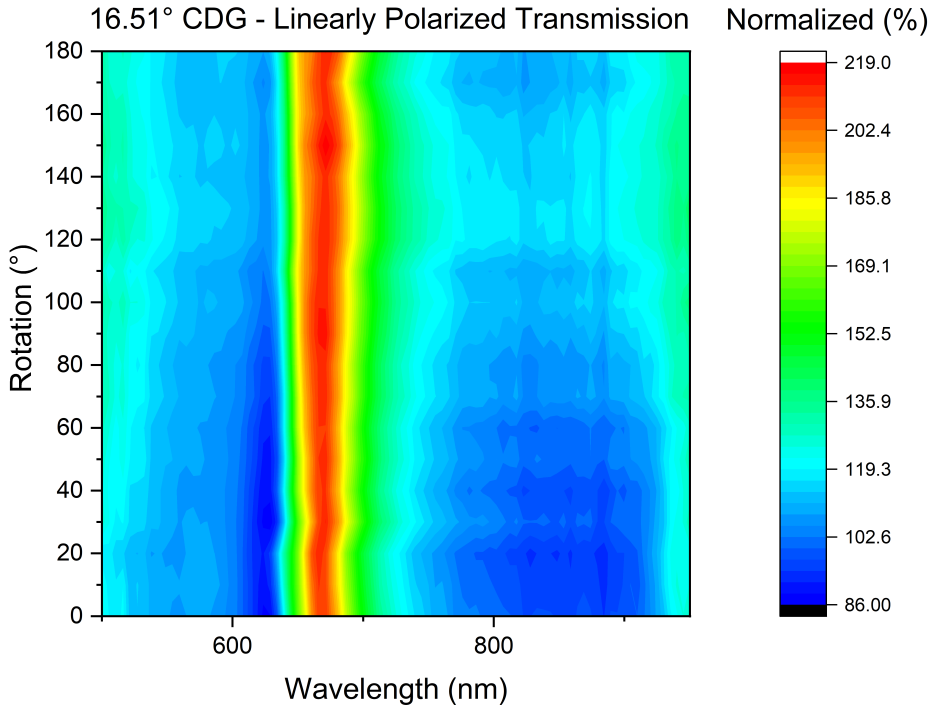

Figure 4.15: Normalized transmission intensity contour graph of a CG with $\Lambda = 717nm$ at varying linear polarization angles

The spectroscopic measurements were taken with a fixed birefringent linear polarizer and a single reference measured prior to the captured SPR measurements. As discussed in Chapter 3, the intensity of the linearly polarized light from the source was variable with respect to the polarization angle, thus a reference for each angle of polarization would be necessary to have a set of normalized spectra to compare between each measurement. The rotation of the CG itself emulates the rotation of the linear polarizer while preventing a calibration of the reference spectra for each individual angle of polarization. The drawback of this method is seen in Figures 4.13-4.15, where the contour heat maps have sharp discontinuities or 'cut' features in the horizontal direction.

For each measurement the CG was repositioned so the peak normalized intensity remained constant while remaining positioned near the center of the source beam. As seen in Table 4.3, the centered linearly polarized beam has a peak SPR signal with only 40 percent of the intensity enhancement as the off-centered parallel beam. Since the transmission spectrum intensity varies extraordinarily between the two edge cases (off-centered,off-center parallel), and shifts continously

between these two positionings, any shift in the plane induces a continuous shift of the spectrum between any two positions. The contour spectra illustrate the sensitivity of the SPR intensity with regard to the position of the linearly polarized beam on a CG, creating the horizontal 'cut' artifacts in Figures 4.13-4.15.

4.2.2 SPR Excitation via Unpolarized Light on Circular Gratings

The CGs were illuminated with unpolarized light from the source nearly identical to the setup seen in Fig. 3.4 with the removal of the linear polarizer preceeding the sample. The SPR signals observed from the three CGs are shown in Fig. 4.16 with peak wavelengths seen in Table 4.4

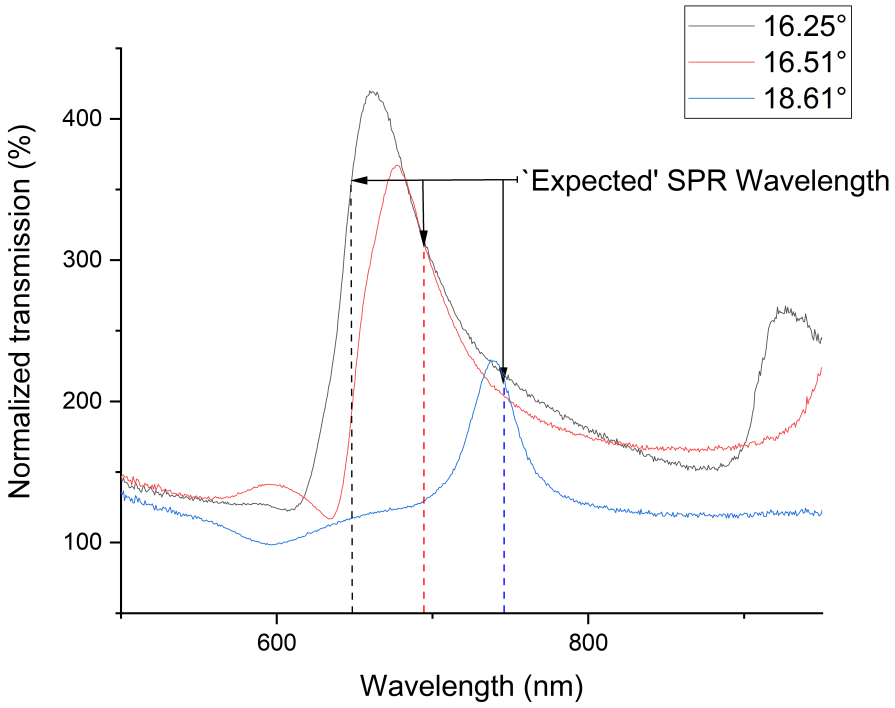

Figure 4.16: Normalized transmision spectra of varying CGs with incident unpolarized light

CDG Angle (Degrees)	Expected SPR Wavelength (nm)	Measured SPR Wavelength (nm)
29.4	648	660
27.9	694	675
24.0	746	738

Table 4.4: Table of the expected SPR peak vs. the measured SPR

The measured values of the SPR peak seen in Table 4.4 correlates fairly well with the expected SPR peak but does not align with great precision. This discrepency can be accounted for by the CG themselves perturbing the SPR signal. The theoretical resonance wavelength is given for a 1-Dimensional (1D) linear grating where the CGs by their nature are 2-Dimensional(2D). However if this were entirely the case, the shift in the measured SPR signal with respect to the expected one would be consistently greater or lower, which is not the case as seen in Table 4.4. The expected SPR wavelength was calculated using Eq 4.2.1 and the measured pitch values in Table 4.1.

The CG inscribed using the nominal angle CDG of 16.51 has an SPR signal peak that is significantly blue-shifted from the expected value given the measured pitch. This could be caused by an experimental uncertainty in the measurments of the pitch, since the theoretical pitch values in Table 3.1 are lower by $\approx 20nm$ than the measured values.

4.2.3 Crossed Polarizer CG Transmission Profile with He-Ne Laser

In Chapter 2, the theoretical transmission profile of a CG at the SP wavelength was derived in Eq. 2.3.36. The surface of Eq. 2.3.36 is graphed using an open-sourced python library, with the code in the appendices.

Eq. 2.3.36 is general enough to express the intensity profile with varying solid angles between polarizers given by θ. When $\theta = 0^o$, the polarizers preceeding and suceeding the CG are both vertical, increasing to a full cross polarization at $\theta = 90^o$. In Fig. 4.17 the spatial profile of Eq. 2.3.36 is plotted for $\theta : 90 - 0^o$ with decreasing 10^o increments. When the polarizers are crossed the intensity profile has four lines of symmetry (vertical,horizontal, $+45^o$,-45^o) creating four equally intense 'lobes' emanating from the center of the plane. As the back polarizer is rotated, decreasing the solid angle between the polarizers, the axes of symmetries decrease to two and lie along the rays which the lobes are centered on. In the case where $\theta = 0^o$, there is simply 1 'lobe' in each half-plane as can be expected as the back polarizer is simply acting as an analyzer of the SPR transmission.

The profile between these two limiting cases ($\theta = (0^o, 90^o)$) have a primary and secondary ray maximums in the half-plane that are rotated away from the

45^o by an angle of $45 - \theta/2$. For example, when the back polarizer is rotated at an angle of $\theta = 20^o$ the primary and secondary maximum rays occur 35^o away from the diagonal rays($\pm 45^o$).

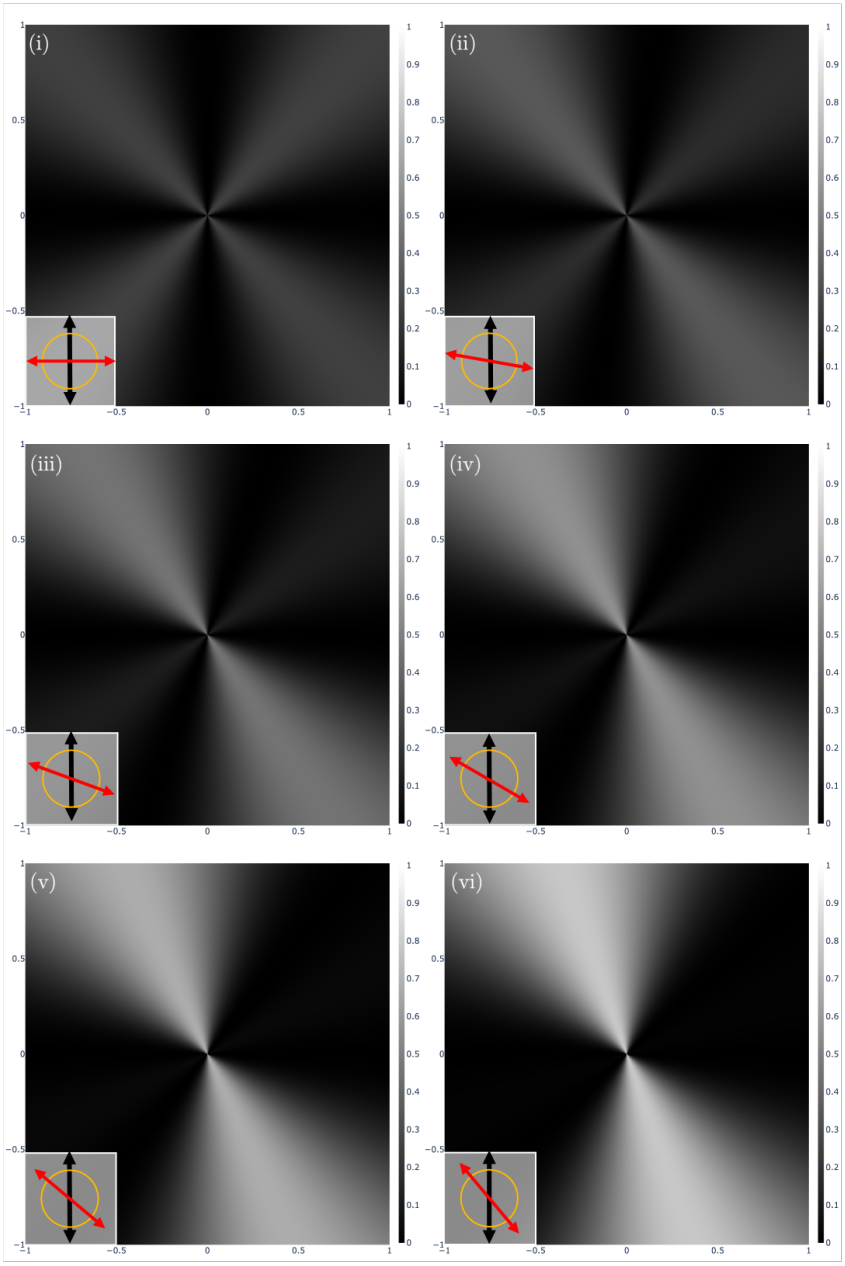

(a) Plots for varying θ:(i) 90^o, (ii) 80^o, (iii) 70^o, (iv) 60^o, (v) 50^o, (vi) 40^o

Figure 4.17: (a) Simulated spatial intensity plots of a two polarizer SPR transmission optical system describe by Eq. 2.3.36

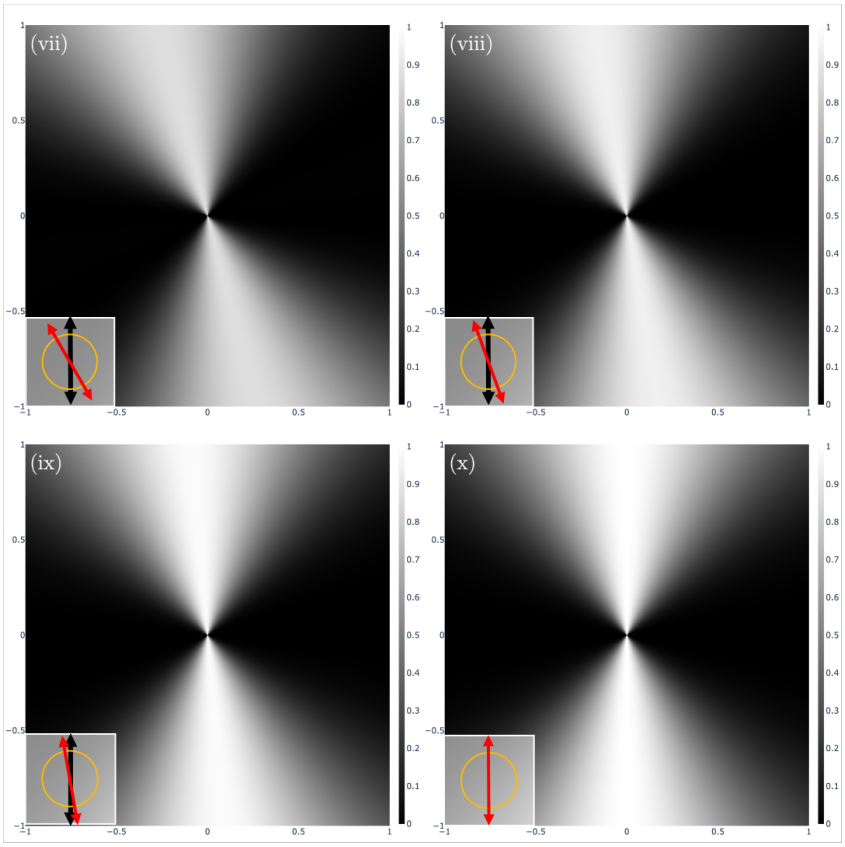

(b) Plots for varying θ:(vii) 30^o, (viii) 20^o, (ix) 10^o, (x) 0^o

Figure 4.17: (b) Spatial intensity plots of a two polarizer SPR transmission optical system describe by Eq. 2.3.36

There is a secondary maximum in all of the intermediate polarizer solid angles ($\theta = (10^o - 80^o)$), however it becomes suppressed as the solid angle becomes smaller, and the contrast of the graphs do not display the location. The secondary maximum is extinguished as the polarizers align since the SPR signal produced around the CG in the orthogonal direction is filtered out.

Using the setup seen in Fig. 3.7 with a He-Ne laser source in replacement of the tunable light filter, photos of the transmission of the collimated beam at varying solid angles between the linear polarizers are seen in Fig. 4.18. The small diagrams in the bottom left corner of each image depicts the relative angles of each polarizer as two-sided arrows with the CG sitting in between seen as the gold circle. The red arrow represents the rotating back polarizer, the analyzer of the system.

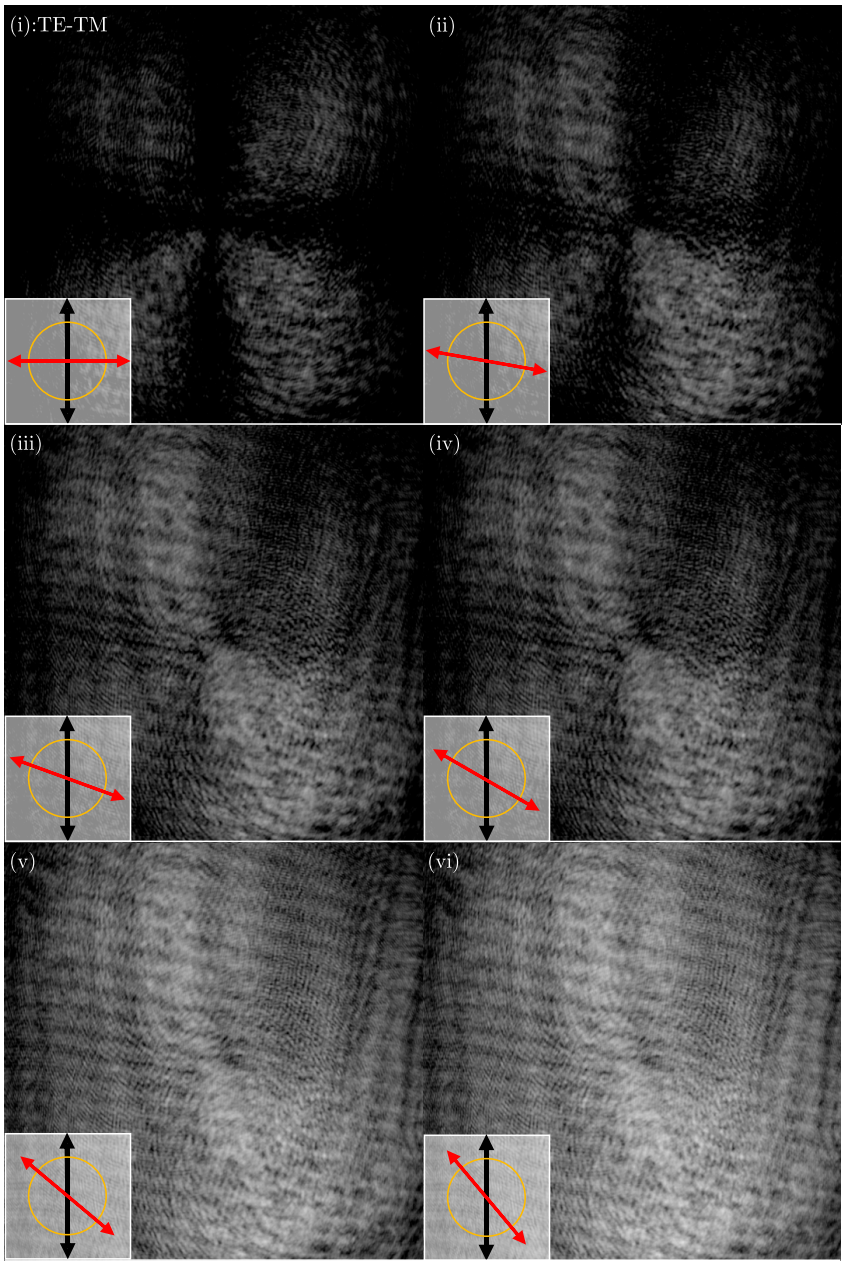

(a) Images with varying solid angles (θ) between the polarizers:(i) 90^o, (ii) 80^o, (iii) 70^o, (iv) 60^o, (v) 50^o, (vi) 40^o

Figure 4.18: (a) Transmission images of a 623nm pitch CG with 631.8nm beam incident beam. Bottom left diagrams: Front Polarizer (Black Arrow), Grating Surface (Gold Cirlce), Back Polarizer (Red Arrow)

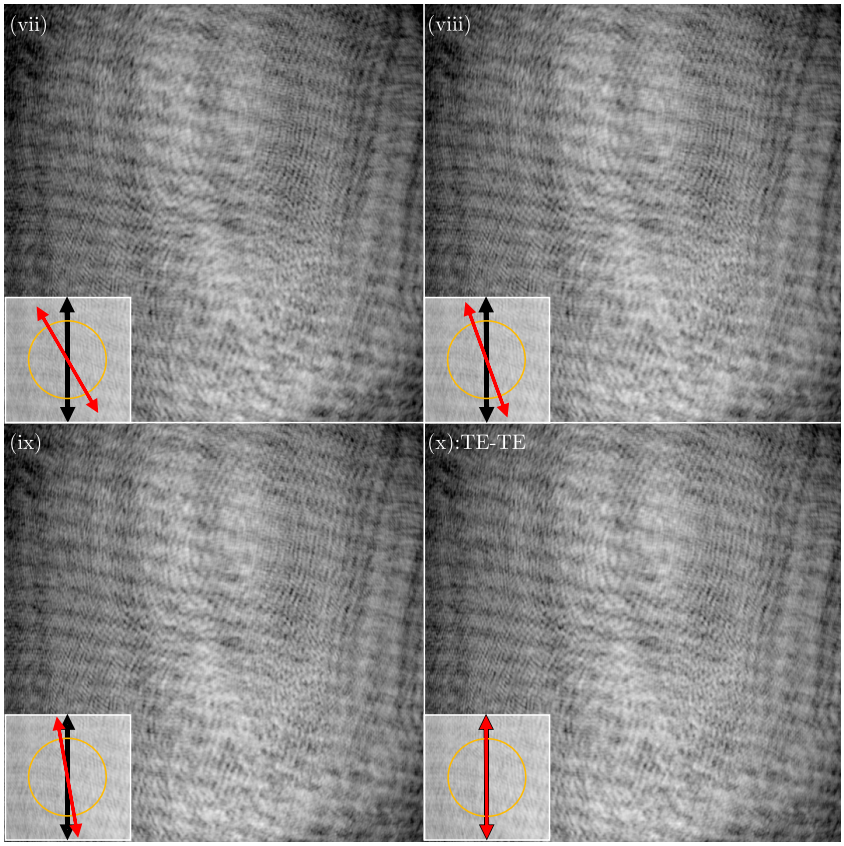

(b) (b) Images with varying solid angles (θ) between the polarizers:(vii) 30^o, (viii) 20^o, (ix) 10^o, (x) 0^o

Figure 4.18: Transmission images of a 623nm pitch CG with 631.8nm beam incident beam. Bottom left diagrams: Front Polarizer (Black Arrow), Grating Surface (Gold Cirlce), Back Polarizer (Red Arrow)

Comparing the images in Fig. 4.18 to the theoretical profiles in Fig. 4.17, the crossed polarizer enivronment experimentally reveals the symmetric four 'lobed' clover as hypothesized. In Fig. 4.18a the four symmetries are broken and the lobes in the second and fourth quadrant start to rotate towards the vertical line while becoming increasingly more intense compared to the adjacent lobes. A divergence occurs in Fig. 4.18b from the hypothesized profiles, where the 'cone' in Fig. 4.17 is only partially visible in the experimental images without any additional analysis. The increased intensity in Fig. 4.18b relative to the dark regions in theory is due to the non-coupling component of the transmission field that was neglected in Eq. 2.3.23. Since the bias and black-out levels of the camera were fixed across

all images, the transmission fields of the non-coupling component are transmitted through the back polarizer as the angle coincides with the front polarizer angle. To mitigate the unwanted transmission modes, the sensor settings of the camera can be altered revealing the SPR profile. This can be as simple as decreasing the bias and increasing blackout level.

Taking a cross section of the first image (TE-TM) in Fig. 4.18a reveals the structure of the profile visible to the camera. The horizontal cross section is chosen as a fraction of the distance away from center, such that the center is chosen as zero and the top and bottom edges are considered as $x = \pm 1$ respectively. Since there are 576 pixels vertically on the camera, the center pixels are 288 and 289. Determining the cross section to sample, the corresponding scaling value (a) of the images, similarly as in Eq. 2.3.26, were labelled by a pixel distance away from the 'middle' row of the sensor. In Fig. 4.19 the signal is noisy as a result of the high bias settings enabled on the camera. To smooth the signal a 10-step Gaussian kernal was used and a convolution was performed on the data in Fig. 4.19 and plotted in Fig. 4.20.

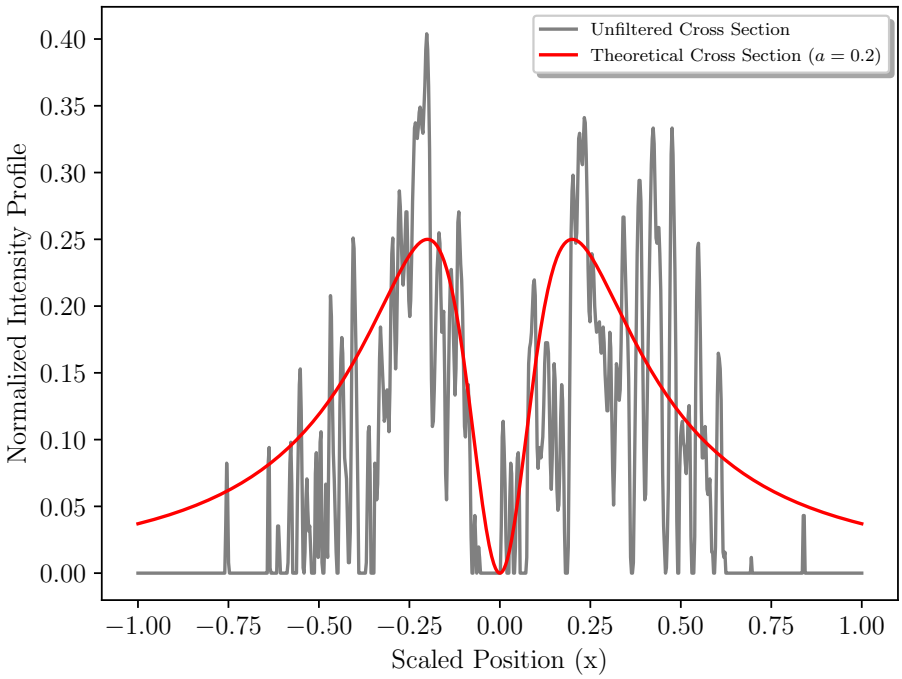

Figure 4.19: Black - Horizontal cross section of the raw data in Fig. 4.18a (i); Red - Theoretical cross section of a profile describe by Eq. 2.3.25 with the constant parameter $a = 0.5$ – x-axis scaled by the number of pixels horizontally, y-axis normalized by 255(Maximum possible pixel value recorded digitally)

As seen in Fig. 4.20, the theoretical line in red is a reasonable approximation to the observed transmission spectrum. The largest deviations occur on the tails of the curve near $x = \pm 1$. The equations of the theoretical cross section do not take the boundary of a CG into account. Therefore the tails extend on as if the grating were infinite in all directions where the image tails off to zero, where the grating ends.

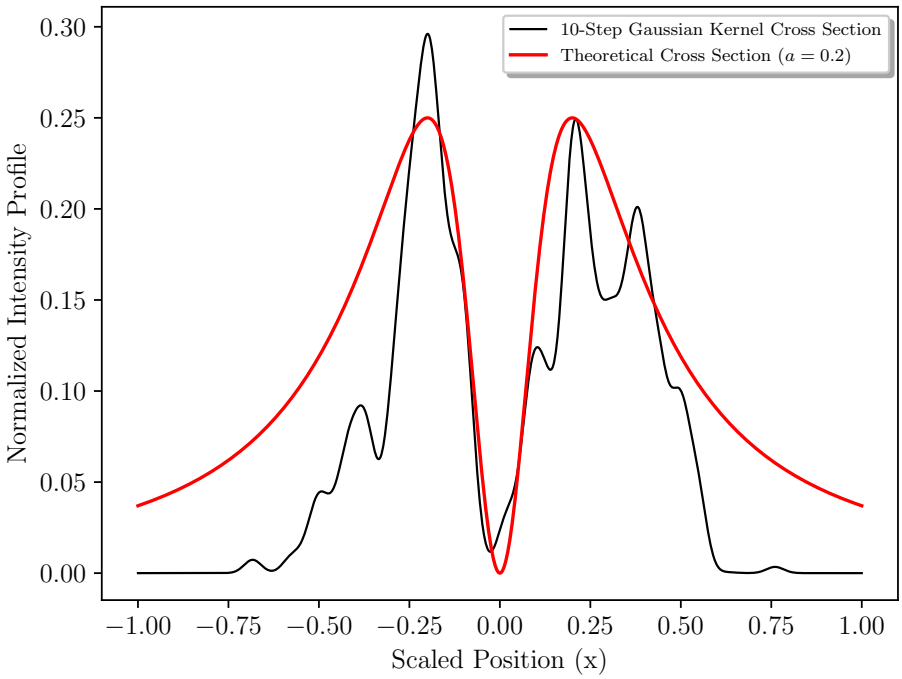

Figure 4.20: 10-step Gaussian convolution of the raw data in Fig. 4.19

4.2.4 Crossed Polarizer CG Transmission Profile with Tunable Light Filter

The Intensity profile of the CG in transmission within the cross polarizer environement under a coherent source revealed the polarization of the excited SPR field through the CG. The polarization of the SPR field inferred with the intensity measurement under cross polarization, is a linearly polarized field with a locally dependent intensity profile.

Under theoretical conditions an excited SPR field has a monochromatic coupling wavelength for each grating pitch. In practice, the dampening of the metal and depth of the gratings broadens the resonance peak. The polarization conversion of the incident field is induced by the SP coupling, therefore the intensity of the profile under cross polarization should correspond to the SPR transmission spectrum. The tunable light filter alters the source's wavelength on the CG. Using the setup in Fig. 3.7, the CMOS camera was used to image the transmission profiles of a CG over a range of wavelengths using the tunable light filter as the source. A sequence of images in Fig. 4.23 show the absence of the 'clover' profile with the bandwidth centered at 570 nanometers. When the bandwidth peak

wavelength was increased, the profile seen under the He-Ne Laser appeared and then faded as the tunable filter reached its functional limit at 730 nanometers. The profile remained as the peak wavelength increased past the resonance peak that was observed by the spectrometer in Table 4.2. The detection of the profile comes from the lorentzian SPR signal seen with spectroscopic measurements, as well as from the broadening and intensifying of the tunable wavelength bandpass as seen in Fig. 3.8.

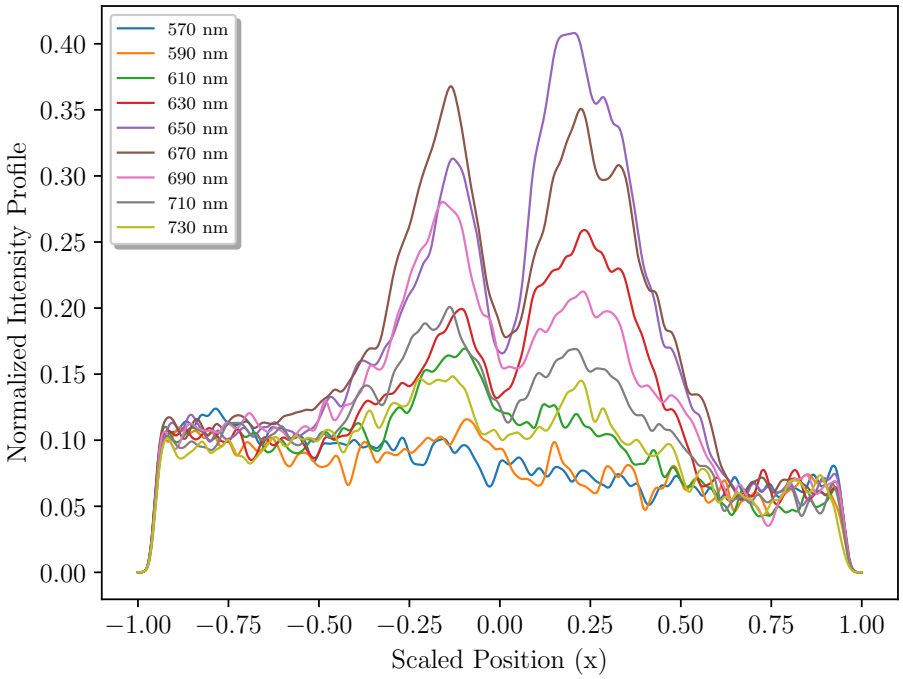

Figure 4.21: Cross sections of images in Fig. 4.23 at pixel row 318 from the top. Where the cross sections are labelled from the spectrum maximum using the tunable filter.

As seen in Fig. 4.21, a cross section of the 'clover' reaches a maximum transmission between 670-690 nanometers. Cross sections of the images were taken along a single row of pixels, convoluted with a 5-step Gaussian Kernel, and plotted in Fig. 4.21. The peaks in Fig. 4.21 are asymmetric across the center. The asymmetry is likely caused by an off center grating, a deviation of the cross polarizers away from a 90 degree solid angle, or an asymmetrical grating structure during inscription.

The focused source isn't symmetric enough to conclude with certainty the underlying reason for the asymmetry across the cross sections. As seen in Fig. 4.23,

there is a circular region of higher intensity throughout the images. This circular region of high intensity is a result of the optical setup used coincidently with the LCD tunable filter. The polychromatic light was focused with an attempt at collimation using a lens in front of the CG resulting in two beam widths of differing intensities. The transmitted light was passed through a diverging lens again to expand the beam width on the camera sensor. This data is therefore not reliable to compare the intensities across the surface, but is useful to analyze intensities over the varying bandpass spectra in Fig. 4.23.

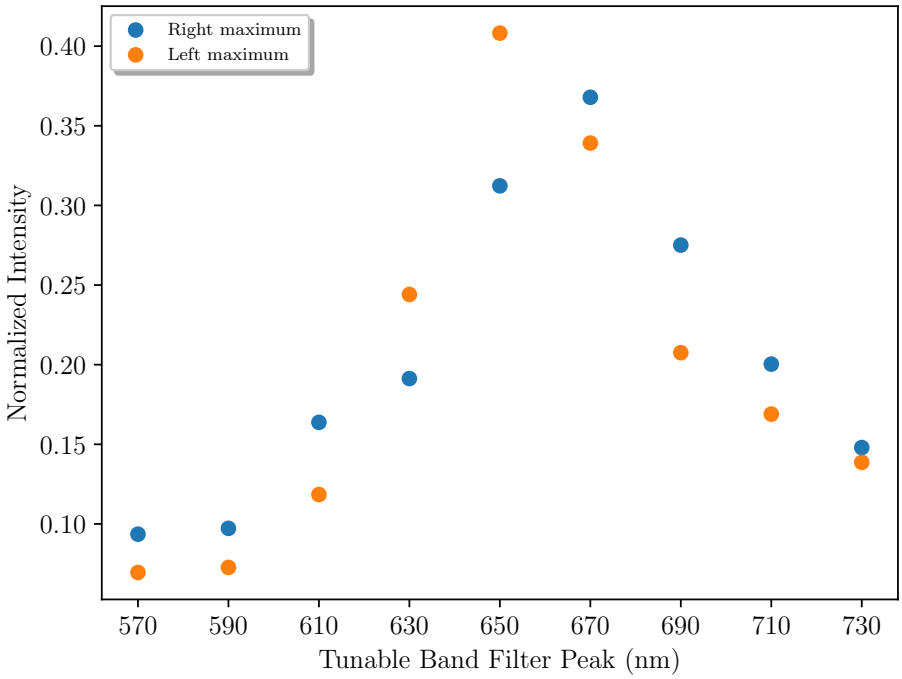

Figure 4.22: Normalized pixel intensity on a pixel corresponding to each max peak with varying bandpass spectrum peaks.

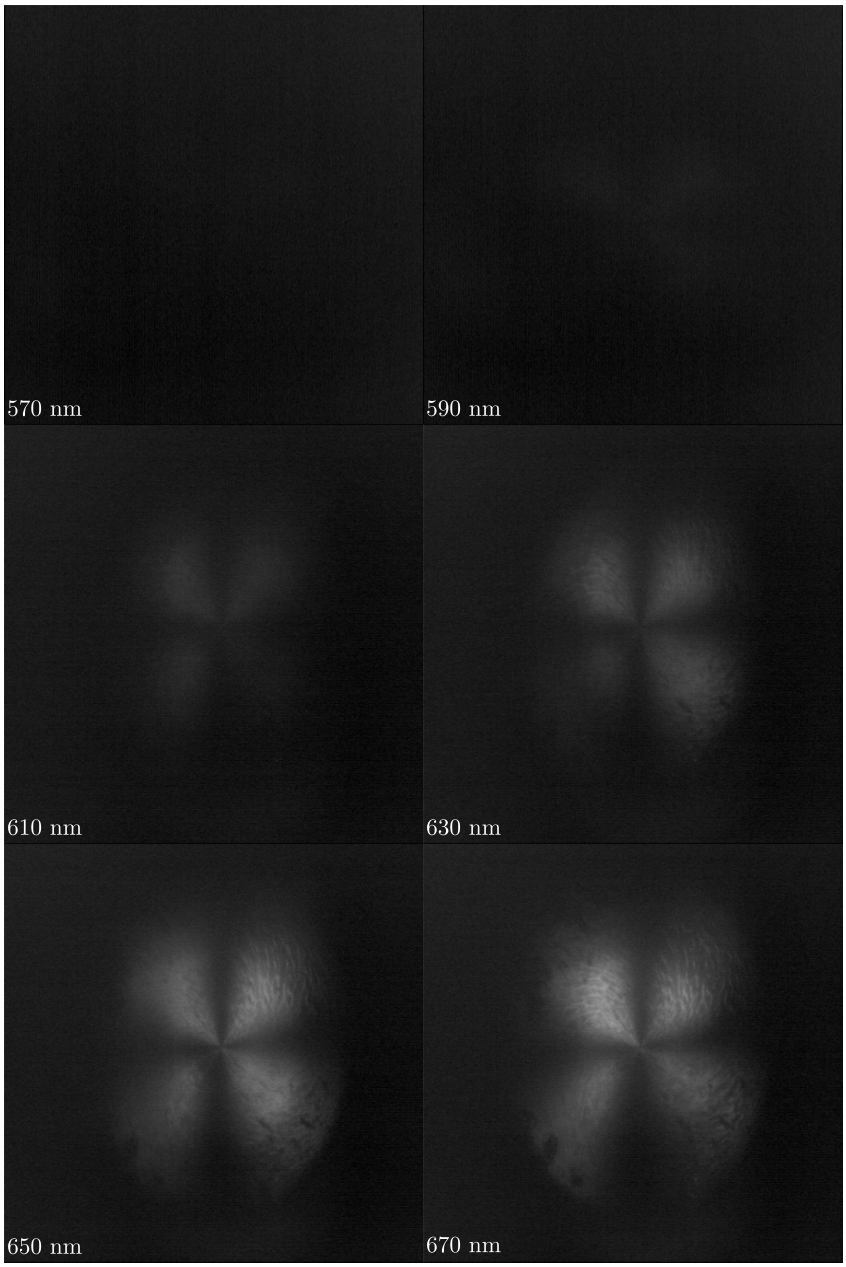

(a) Increasing peak transmission wavelength from top-down, and left-right.

Figure 4.23: (a) Transmission images of a 623nm pitch CG with varying spectrum wavelength peaks and bandwidths. Wavelength peaks denoted in the bottom left of each image

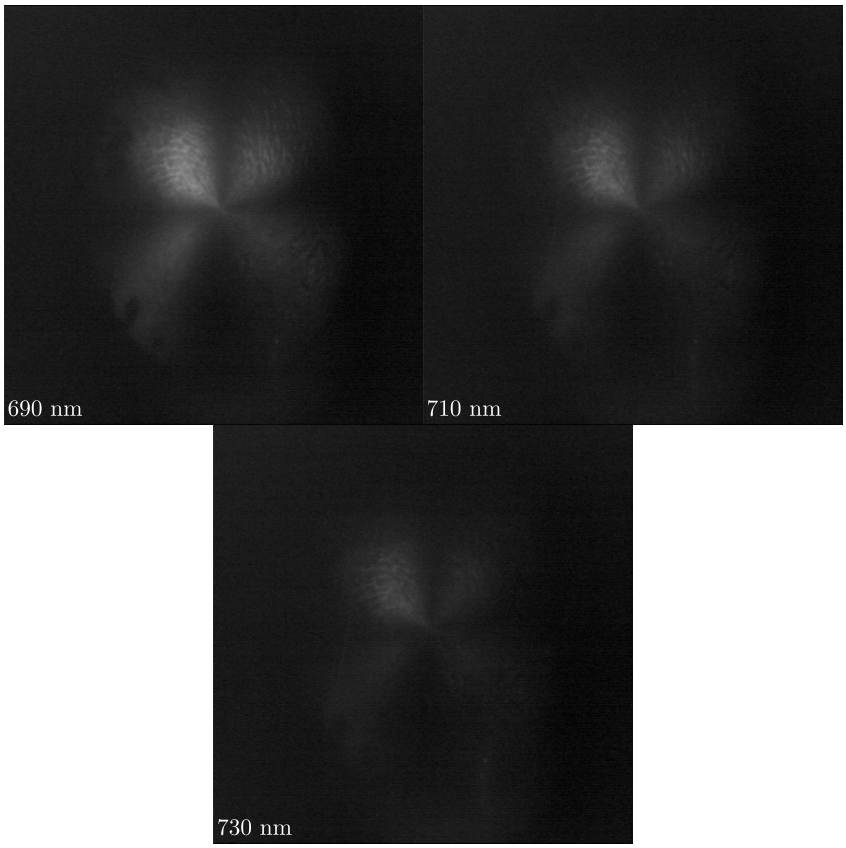

(b) Increasing peak transmission wavelength from top-down, and left-right.

Figure 4.23: (b) Transmission images of a 623nm pitch CG with varying spectrum wavelength peaks and bandwidths. Wavelength peaks denoted in the bottom left of each image

A reference pixel was chosen from each peak of the cross section (left/right) as seen in Fig. 4.21, and was picked by using the highest intensity pixel across all cross sections. The intensity of the reference pixel was plotted for all cross sections vs. the bandpass peak of the incident spectrum as seen in Fig. 4.22. The transmission intensities of the chosen cross sections for each peak (left/right) reached maximum at different wavelengths 670nm/650nm respectively. The scatter plot in Fig. 4.22 shows a resonant behaviour peaking in between 650-670nm, within the range of the SPR peak for a 623 nm pitch grating as seen in Table 4.2.

4.2.5 Circular/Elliptical Polarized Source on Circular Grating

The CG was irradiated with 'almost' circularly polarized light using a quarter-wave plate and a He-Ne source, where the polarimeter was used to verify the polarization of the output beam through the quarter-wave plate. The phase space between the limits of linear polarization and circular polarizations, lie the space of elliptically polarized plane waves. The polarizations of a transverse plane wave have unique momentum and energy states up to a rotation in the plane. When considering time-averaging processes all plane wave polarizations are considered as instaneously linearly polarized, where the direction of linear polarization rotates in the plane for the elliptic and circular polarized cases.

An SPR excitation on a grating is polarization dependent along the direction of the grating vector. Therefore when a circular polarized EM field is incident on a CG, the SP mode is maximally and minimally coupled when the electric field is parallel and orthognal to the grating vector respectively. The period-averaged SPR excitation is equivalent on all rays of the CG and therefore the intensity of the transmitted SPR intensity should be equivalent when averaged over one or more cycles. When the SPR is induced via linear polarization the SPR mode radiates linearly polarized light in the direction of the grating vector. A CG illuminated by a circularly polarized plane wave will induce an SPR field with radial polarization by the geometry of the grating vectors. The period-averaged intensity of a collimated beam is constant, therefore the SPR intensity induced on every ray is equivalent and the radially polarized SPR field is flat.

If we assume the transmitted SPR field dominates the non-coupled transmitted field, the introduction of a linear polarizer into on the back-side of the CG with an incident circularly polarized field will produce an intensity profile seen in Fig. 2.8. As seen in Fig. 2.8, the SPR cone axis coincides with the direction of the linear polarizer. The images in 4.24 show an intensity profile similar to that seen in Fig. 2.8, up to a rotation of the analyzing linear polarizer. The cause of this rotational discrepency in the spatial profile could be caused by a sensitvity to the polarization induced by the quarter wave plate. The polarization of the incident field was measured using the polarimeter and found to be right hand elliptically polarized with significant eccentricity away from perfectly right handed circular polarized (RHCP) ($\chi = 45°$) as can be seen in Table 4.5, being nearly circular. More about the polarimeter and the math behind it in the Appendices. Any eccentricity away from $\pm 45°$ breaks the symmetry of the fields both incident and transmitted, thus the CG is sensitive to the eccentricity parameter using the SPR field intensity.

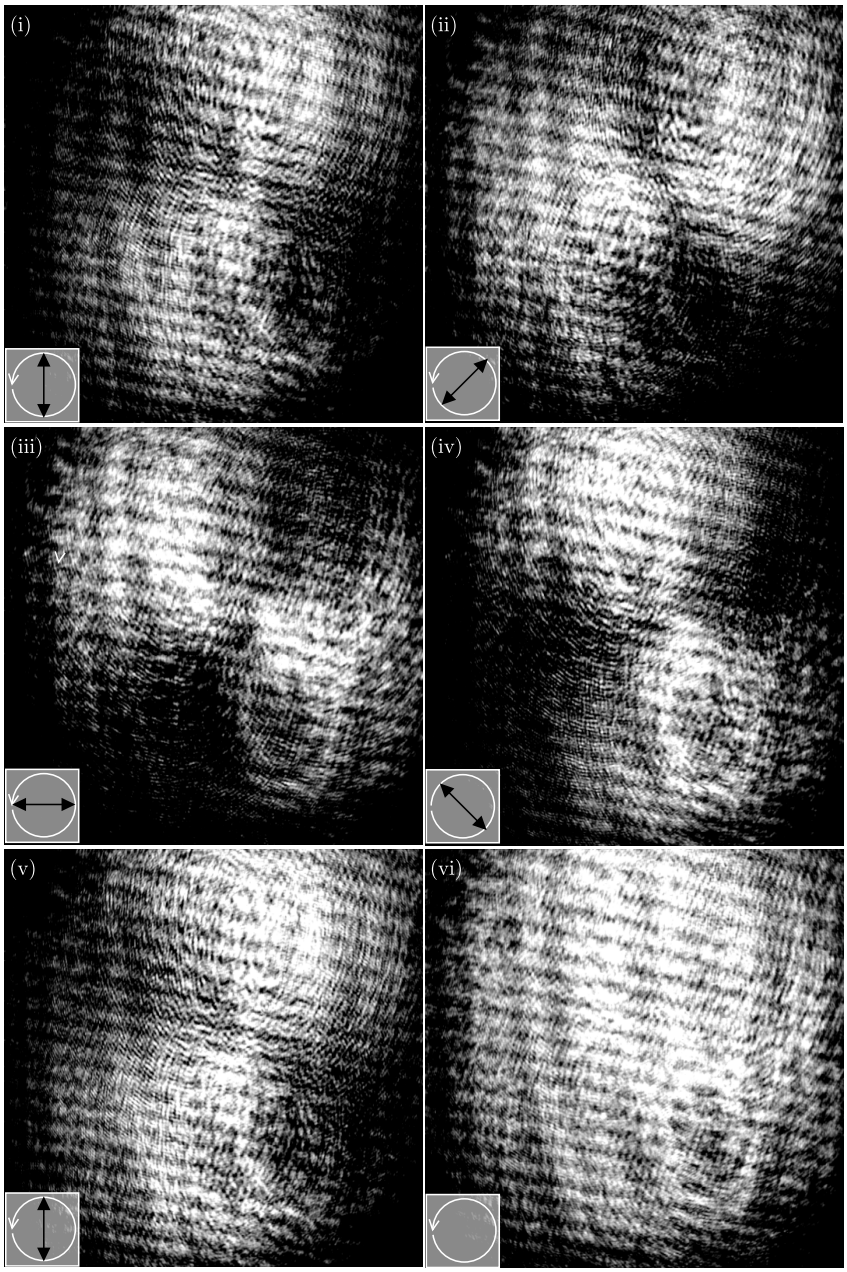

Figure 4.24: Transmitted profile of 'circularly' polarized light with back linear polarizer filter at varying angles: (i) TM, (ii) 45^o, (iii) TE, (iv) 135^o, (v) TM; Transmitted profile of circularly polarized light with no back polarizer (vi) Reference image of the trasmitted field without the linear polarizer analyzer

Polarimeter Measurements							
	S_0	S_1	S_2	S_3	ψ (Azimuth)	χ (Ellipticity)	ϕ (Phase Shift)
RHCP	2.526	-0.253	0.256	2.503	67.3±0.1°	40.9±0.1°	84.16±0.01°
	Normalized Stokes Comp. (±0.0001)						
	1	-0.1000	0.1013	0.9911			

Table 4.5: The Stokes vector components of the incident 'RHCP' beam on the circular grating as seen in Fig. 4.24

This relationship can be observed directly when the polarization ellipse that the polarimeter measured is laid over top of one of the images from Fig. 4.24, as seen in Fig. 4.25. The largest expected intensity response from the plasmonic cone, if the polarization is completely circular, would be along the vertical ray. The oblique ellipticity causes a rotated plasmonic cone with respect to the ideal circular polarized case and the linear polarizer angle in Fig. 4.24

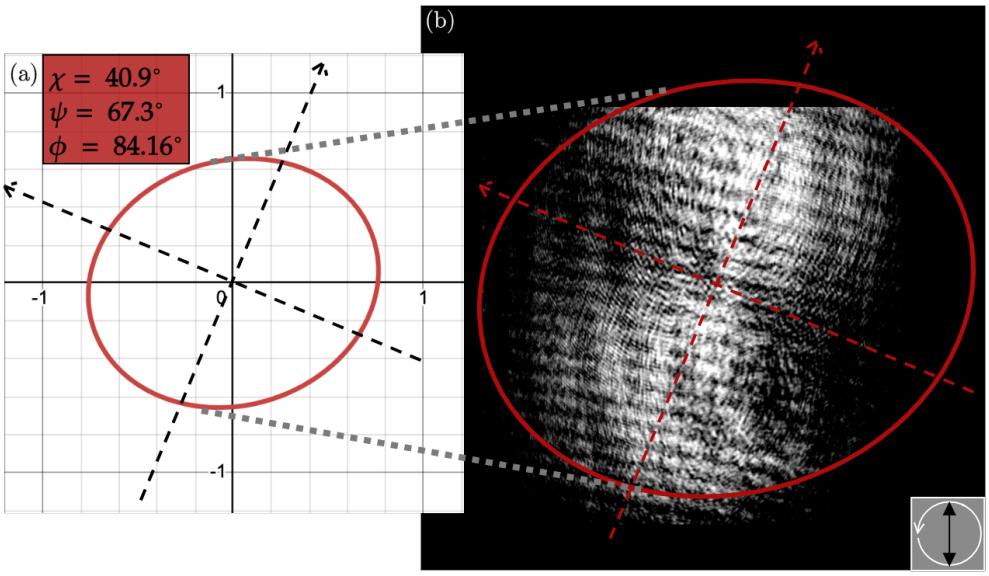

Figure 4.25: Figure showing the intensity relationship of the transmitted beam signal through a circular grating and the incident polarization; (a) Normalized polarization ellipse generated from the polarimeter measurements in Table 4.5 (b)Scaled ellipse overlaid on a transmission image with a vertical linear polarizer analyzer

It's important to note the polarization conversion of the incident field into the SPR field imparts an orbital angular momentum (OAM) with a helical phase front. This phase front conversion of the SPR field would interfere with the non-coupled transmitted field, potentially effecting the transmitted intensity profile.

4.2.6 Excitation of SPR on Circular Grating using collimated Laguerre-Gaussian Modes

A He-Ne LASER was collimated and centered on the RPC. The centering is important because of the radial symmetry in the twisted nematic cell that converts the linear polarization of the incident light into an axially symmetric polarized beam. Centering the RPC's transmitted beam on the CG, the azimuthal and radial transmission were imaged as seen in Fig. 4.26.

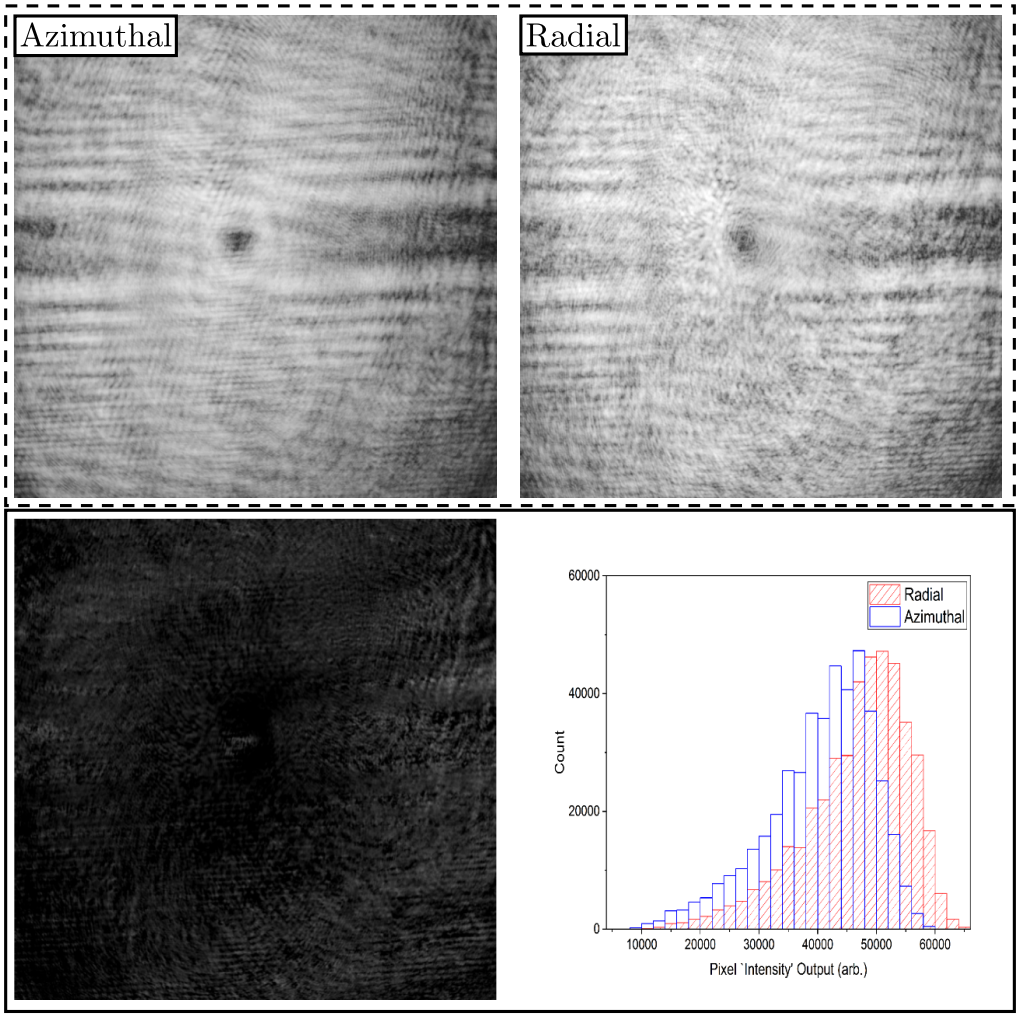

Figure 4.26: Top Left/Right: Transmission of Azimuthally/Radially Polarized LG mode. Bottom Left: Pixel subtraction of the radial image by the azimuthal image. Bottom Right: Count of pixels at each registered intensity of the radial/azimuthal images

As seen in Fig. 3.6, an azimuthally polarized beam can be used as the reference for an SPR image on a CG, similar to a TM/TE reference on a linear grating. The transmission images with both azimuthal and radial polarizations were used to generate a new image by pixel-to-pixel subtraction (radial-azimuthal).

In Fig. 4.3 the CGs were measured to have increasing depth from the center out to the edge, corresponding to the increased SPR transmission seen in Fig. 4.26 (bottom-left). As discussed in Chapter 2, the diffraction of the field induces the coupling of the SP mode to the incident EM field. The grating depth, as long as not too deep (> 70nm), positively correlates with the SPR field intensity via the diffraction efficiency. Since the grating depth increases from the center out, the SPR intensity enhancement is expected to be greatest near the edges of the grating.

5 Conclusion

In conclusion, azobenzene lithography has been shown to inscribe large-aperture circular gratings for use in optical plasmonic research. Specifically the following results have presented the feasibility of tuning the SPR wavelength (λ_{SPR}) by a change in the inscribed pitch of the circular gratings; via a change in the nominal angle of the conical mirror, or CDG (θ_{CDG}). The 'Introductory SPR Theory', using a 1D 'flat' surface,has been shown to predict SPR wavelength to a reasonable degree, admittedly with questionable precision. In practice the perturbations of the flat interface model, from large amplitude gratings, create energy bandgaps in the dispersion curve leading to a splitting of the resonance frequency as seen in some of the orientations of the circular grating.

Furthermore, 'Full' Circular Gratings were inscribed using in-house polished conical metal mirrors, where circularly polarized light interferd at a plane on a 'circular' conic with a smaller area. This focusing in the inscribing plane results in a growth-rate curve of the SRGs over an extended exposure. Specifically, the focusing near the center of the axis of the inscription plane causes ray surface deformations that extends in the order of millimeters out from the center, with a center mountain deformation, an order of magnitude higher than the thickness of the AZO glass film. These surface deformations are hypothesized to be formed by caustics on the interference plane; areas of dense ray packing. This chaotic 'intensity-polarization' field possesses an irregular gradient profile, in which scattering effects dramatically alter the interference pattern on the film, therefore generating an unexpected crimpling of the surface, and supressing SRG formation. AFM scans verified that the grating uniformity and amplitude increased as the curvature decreased due to the reduced area contraction in those regions of interference; more work should be done attempting to inscribe more unifrom gratings with larger curvature. Commercial products such as convex conical mirrors have been made using a glass substrate with a metal coating; similar to axicons. Potentially, CDG's could be made by polishing a concave conical surface into a glass cylinder and depositing a metal film onto the reflecting surface. Ultimately it may be just more practical to use axicons for large curvature inscriptions.

The SPR response of the circular gratings have unique transmission properties under varying plane-wave polarizations. The transmission spectrum for each

circular grating had a peculiar quality under linear polarization; where the SPR response increased under half illumination vs. full-illumination. More specifically, a circular grating illuminated with a linearly polarized broad spectrum optical beam had the largest SPR peak maximum transmittance when the grating was 'half-illuminated' along the axis of polarization; a minimum when centered over the axis of the circular grating. This is thought to be from a suppression of the surface plasmon at normal incidence from the irregular nature of the center of the gratings, exciting a split plasmon at a greater radius but at an angle in which two counter propagating surface plasmons are excited. Another more suspect reason comes from a waveguiding effect from the circular grating itself combined with the varying depth profile with respect to the radius. This future work can be readily measured by simply taking measurements of the beam intensity across the beam width and analyzing with respect to the SPR response maximum across, local areas along the grating ray; measurements have verified the increased intensity in the SPR reponse, along an arbitrary ray (center→edge). A more statistical image of the grating can be achieved with greater resolution with more sampling to verify SPR response more precisely at varying angles of incidence. Lastly in relationship to the beam positioning, if it's the case the beam has a negligible flux variance then the anomalous intensity behaviour could be attributed simply an artifact from the diverging beam, or a waveguiding effect from the curvature of the grating itself.

The circular gratings' transmission spectrums were measured under largely unpolarized light and found to have a strong SPR response with peaks dependent on the grating pitch. The large aperture gratings show a proof of concept for measuring an intensity profile of an SPR transmission intensity; and measured a sharp intensity profile under various optical setups and even under convolution, where the grating acts as a wavelength dependent filter. Specifically, it was shown that the intensity profile of the SPR mode on a circular grating can be modelled with a linear approximation; involving the evanescent non-coupling component with the coupling component of the SP mode; the approximation was uniquely fit as a linear transformation by exploiting the symmetries involved with the projections and approimations of the supression of the non-coupling component. The regard for a time-averaged non-degenerate general elliptical electric field, the projections of polarization with regard to a single stationary grating vector was not discussed. It is assumed that any ellipticity on the grating will excite a SP mode with an angular dependent intensity profile and have shown some sensitvity with regard to this experimentally. Future work on this would involve discussing fields on less symmetric gratings (elliptical/ hyperbolic curvature), and elliptical or CVB's on these circular gratings.

References

[1] StefanA. Maier, editor. *Plasmonics:Fundamentals and Applications*. Springer Link, 2007. ISBN: 978-0-387-37825-1.

[2] KWelford. Surface plasmon-polaritons and their uses. *Optical and Quantum Electronics*, 23:1–27, 1991.

[3] R.W.Wood. On a remarkable case of uneven distribution of light in a diffraction grating spectrum. *Proceedings of the Physical Society of London*, 18(1), 1902.

[4] LordRayleigh O.M. P.R.S. Note on the remarkable case of diffraction spectra describe by prof. wood. *The London, Edinburgh, and Dublin Philisophical Magazine and Journal of Science*, 14:60–65, 1907.

[5] U.Fano. The theory of anomalous diffraction gratings and of quasi-stationary waves on metallic surfaces (sommerfeld's waves). *Journal of the optical society of America*, 31:213–222, 1941.

[6] E. Kretschmann and H. Raether. Notizen: Radiative decay of non radiative surface plasmons excited by light. *Zeitschrift für Naturforschung A*, 23:2135 – 2136, 1968.

[7] Andreas Otto. Excitation of nonradiative surface plasma waves in silver by the method of frustrated total reflection. *Zeitschrift für Physik*, 216:398 – 410, 1968.

[8] J.D.Swalen. Optical wave spectroscopy of molecules at surfaces. *The Journal of Physical Chemistry*, 83(11):1438–1445, 1979.

[9] H. Guo and et. al. The effects of grating profile on dispersion relations of surface plasmon polaritons in kretschmann-raether configuration. *Plasmonics*, 16:2249–2258, 2021.

[10] A. V.Zayats, I. I. Smolyaninov, and A. A. Maradudin. Nano-optics of surface plasmon polaritons. *Physics Reports*, 408(3):131–314, 2005. ISSN 0370-1573. doi: https://doi.org/10.1016/j.physrep.2004.11.001.

[11] A.J.McAlister. Plasma resonance absorption in thin metal films. *Physical Review Journals Archive*, 132(4):1599–1602, 1963.

[12] E.A. Stern. Plasma radiation by rough surfaces. *Physical Review Letters*, 19 (23):1321–1324, 1967.

[13] G.Mie. Beiträge zur optik trüber medien, speziell kolloidaler metallösungen. *Annalen der Physik*, 330(3):377–445, 1908.

[14] K. Lance Kelly, Eduardo Coronado, Lin Lin Zhao, and George C. Schatz. The optical properties of metal nanoparticles: The influence of size, shape, and dielectric environment. *The Journal of Physical Chemistry B*, 107(3): 668–677, 2003.

[15] T. W.Ebbesen, H. J. Lezec, H. F. Ghaemi, T. Thio, and P. A. Wolff. Extraordinary optical transmission through sub-wavelength hole arrays. *Nature*, 391: 667–669, 1998.

[16] W.L. Barnes, T.W.Preist, S.C. Kitson, and J.R.Sambles. Physical origin of photonic energy gaps in the propagation of surface plasmons on gratings. *Physical Review B*, 54(9):6227–6244, 1999.

[17] P. T.Worthing and W. L. Barnes. Efficient coupling of surface plasmon polaritons to radiation using a bi-grating. *Applied Physics Letters*, 79(19): 3035–3037, 2001.

[18] E. Devaux, T. W. Ebbesen, J. C. Weeber, and A. Dereux. Launching and decoupling surface plasmons via micro-gratings. *Applied Physics Letters*, 83 (24):4936–4938, 2003.

[19] S. Chevalier and et.al. Optically tunable metal-dielectric diffractive structures. *Physical Review Materials*, 6(9), 2022.

[20] L. Nedelchev and et.al. In-line and off-axis polarization-selective holographic lenses recorded in azopolymer thin films via polarization holography and polarization multiplexing. *Applied Optics*, 62(10):D1–D7, 2023.

[21] A. Porfirev and et.al. Writing and reading with the longitudinal component of light using carbazole-containing azopolymer thin films. *Scientific Reports*, 12(3477), 2022.

[22] Y. Bdour, C.Escobedo, and R.G.Sabat. Optically tunable metal-dielectric diffractive structures. *Opitcs Express*, 27(6):8429–8439, 2019.

[23] I. C. Merritt, D. Jacquemin, and M. Vacher. cis-trans photoisomerisation of azobenzene: a fresh theoretical look. *Phys. Chem.*, 23:19155–19165, 2021.

[24] Paul Rochon, E .Batallaa, and L. Natansohn. Optically induced surface gratings on azoaromatic polymer films. *Applied Physics Letter*, 66(2):136–138, 1995.

[25] N. S. Yadavalli, M.Saphiannikova, and S.Santer. Photosensitive response of azobenzene containing films towards pure intensity or polarization interference patterns. *Applied Physics Letters*, 105(5), 2014.

[26] H. S. Kang, S.Lee, and J-K.Park. Multi-level micro/nanotexturing by three-dimensionally controlled photofluidization and its use in plasmonic applications. *Advanced Materials*, 25(38):5490–5497, 2013.

[27] Yazan Bdour, Carlos Escobedo, and Ribal Georges Sabat. Wavelength-selective light sensor fabricated on a photoactive azobenzene film. In Jaehwan Kim, Kyo D. Song, Ilkwon Oh, and Maurizio Porfiri, editors, *Nano-, Bio-, Info-Tech Sensors, and Wearable Systems 2022*, volume 12045, page 1204503. International Society for Optics and Photonics, SPIE, 2022. doi: 10.1117/12.2610973. URL `https://doi.org/10.1117/12.2610973`.

[28] S. Nair, C.Escobedo, and R.G. Sabat. Crossed surface relief gratings as nanoplasmonic biosensors. *American Chemical Society*, 2(3):379–385, 2017.

[29] Petr A. Ledin and et. al. Light-responsive plasmonic arrays consisting of silver nanocubes and a photoisomerizable matrix. *American Chemical Society*, 7 (8):4902–4912, 2015.

[30] M. Mazloumi, P. Rochon, and R. G. Sabat. Dynamic resonant waveguide crossed gratings for wavelength-selective polarization conversion and optical modulation. *OSA Continuum*, 4(8):2284–2293, 2021.

[31] Q. Zhen. Cylindrical vector beams: from mathematical concepts to applications. *Advances in Optics and Photonics*, 1(1):1–57, 2009.

[32] A. Yao and M. J. Padgett. Orbital angular momentum: origins, behavior and applications. *Advances in Optics and Photonics*, 3(2):161–204, 2011.

[33] R. Dorn, S. Quabis, and G. Leuchs. Sharper focus for a radially polarized light beam. *Physical Review Letters*, 91(23), 2003.

[34] M. Meier, V. Romano, and T. Feurer. Material processing with pulsed radially and azimuthally polarized laser radiation. *Applied Physics A*, 86:329–334, 2007.

[35] Q. Zhan. Evanescent bessel beam generation via surface plasmon resonance excitation by a radially polarized beam. *Optics Letters*, 31(11):1726–1728, 2006.

[36] N. Karedla and et. al. Simultaneous measurement of the three-dimensional orientation of excitation and emission dipoles. *Physical Review Letters*, 115 (17), 2015.

[37] B. Ndagano and et. al. Fiber propagation of vector modes. *Optics Express*, 23(13), 2015.

[38] S. Chen and et. al. Cylindrical vector beam multiplexer/demultiplexer using off-axis polarization control. *Light: Science and Applications*, 10(222), 2021.

[39] D. Pohl. Operation of a ruby laser in the purely transverse electric mode te01. *Applied Physics Letters*, 20(7):266–267, 1972.

[40] K. Yonezawa, Y. Kozawa, and S. Sato. Generation of a radially polarized laser beam by use of the birefringence of a c-cut nd:yvo4 crystal. *Optics Letters*, 31(14):2151–2153, 2006.

[41] M. A. Ahmed, A. Voss, M. M. Vogel, and T. Graf. Multilayer polarizing grating mirror used for the generation of radial polarization in yb:yag thin-disk lasers. *Optics Letters*, 32(22):3272–3274, 2007.

[42] S N. Khonina and et. al. Generation of cylindrical vector beams of high orders using uniaxial crystals. *Journal of Optics*, 17(6), 2015.

[43] M. R. Beversluis, L. Novotny, and S. J. Stranick. Programmable vector point-spread function engineering. *Optics Express*, 14(7):2650–2656, 2006.

[44] P. G.-Martínez and et. al. Efficient on-axis slm engineering of optical vector modes. *Optics and Lasers in Engineering*, 125, 2020.

[45] S N. Khonina and et. al. Formation of hybrid higher-order cylindrical vector beams using binary multi-sector phase plates. *Scientific Reports*, 8(14320), 2018.

[46] J. A. Davis and et. al. Analysis of a segmented q-plate tunable retarder for the generation of first-order vector beams. *Applied Optics*, 54(32):9583–9590, 2015.

[47] SteveC. Tidwell, DenisH. Ford, and Wayne D.Kimura. Generating radially polarized beams interferometrically. *Applied Optics*, 29(15), 1990.

[48] V. G. Niziev, R. S. Chang, and A. V. Nesterov. Generation of inhomogeneously polarized laser beams by use of a sagnac interferometer. *Applied Optics*, 45(33):8393–9399, 2006.

[49] M. Schadt and W. Helfrich. Voltage-dependent optical activity of a twisted nematic liquid crystal. *Applied Physics Letters*, 18(4), 1971.

[50] M. Stalder and M. Schadt. Linearly polarized light with axial symmetry generated by liquid-crystal polarization converters. *Optics Letters*, 21(23), 1996.

[51] R. Yamaguch, T. Nose, and S. Sato. Liquid crystal polarizers with axially symmetrical properties. *Japanese Journal of Applied Physics*, 28(9R):1730, 1989.

[52] S-W. Ko and et. al. Polarization converters based on axially symmetric twisted nematic liquid crystal. *Optics Express*, 18:3601–3607, 2016.

[53] ARCoptix. Radial Polarization kernel description, 2006. URL `https://arcoptix.com/radial_polarization_converter.htm`.

[54] E. Hutter and J. H.Fendler. Exploitation of localized surface plasmon resonance. *Advanced Materials*, 16(19):1685–1706, 2004.

[55] G. Isfort, K. Schierbaum, and D. Zerulla. Polarization dependence of surface plasmon polariton emission. *Physical Review B*, 74(3), 2006.

[56] Y. Gong, A. G. Joly, P. Z. El-Khoury, and W. P.Hess. Polarization-directed surface plasmon polariton launching. *The Journal of Physical Chemistry Letters*, 8(1):49–54, 2016.

[57] Y. Dai and H. Petek. Plasmonic spin-hall effect in surface plasmon polariton focusing. *ACS Photonics*, 6(8):2005–2013, 2019.

[58] J. P. B. Mueller, K. Leosson, and F. Capasso. Polarization-selective coupling to long-range surface plasmon polariton waveguides. *Nano Letters*, 14(10): 5524–5527, 2014.

[59] E. Diak, M. Mazloumi, and R. G. Sabat. Tunable narrowband plasmonic light emission from metallic crossed surface relief gratings. *Optics Express*, 28(26), 2020.

[60] Heikki Rekola et.al. Digital holographic microscopy for real-time observation of surfac-relief grating formation on azobenzene-containing films. *Scientific Reports*, 10(19642), 2020.

[61] Jamie Leibold. *Design and Analysis of Circular Diffraction Gratings*. PhD thesis, Royal Military College of Canada, 2015.

[62] M. Mazloumi and R. G. Sabat. Real-time imaging of plasmonic concentric circular gratings fabricated by lens–axicon laser interference lithography. *Micromachines*, 14(11), 2023.

[63] Nicholas Swanson and Ribal Georges Sabat. Nano-fabrication and characterization of non-uniform surface relief gratings in azobenzene molecular glass films. In Georg von Freymann, Winston V. Schoenfeld, and Raymond C. Rumpf, editors, *Advanced Fabrication Technologies for Micro/Nano Optics and Photonics XII*, volume 10930, page 1093013. International Society for Optics and Photonics, SPIE, 2019. doi: 10.1117/12.2504382. URL `https://doi.org/10.1117/12.2504382`.

[64] Yevgeniy Mikhyeyev. *Surface Plasmon Microscopy of Inhomogeneous Aqueous Mixtures*. PhD thesis, Royal Military College of Canada, 2019.

[65] C.K.Chang et.al. Similarities and differences for light-induced surface plasmons in one- and two-dimensional symmetrical metallic nanostructures. *Optics Letters*, 31(15):2341–2343, 2006.

[66] A. Maleki and et.al. Curved gratings as plasmonic lenses for linearly polarised light. *Plasmonics*, 11:365–372, 2016.

[67] F. Wang, M. Xiao, K. Sun, and Q-H. Wei. Generation of radially and azimuthally polarized light by optical transmission through concentric circular nanoslits in ag films. *Optics Express*, 18:63–71, 2010.

[68] Eugene Hecht, editor. *Optics*. Addison-Wesley, 1987. ISBN 10: 020111609X / ISBN 13: 9780201116090.

[69] R.Clark Jones. A new calculus for the treatment of optical systems. *Journal of the Optical Society of America*, 31:488–493, 1941.

[70] Max Born and Emil Wolf, editors. *Principles of Optics*. Pergamon Press, 1999. ISBN: 978-110-8477-43-7.

[71] George.G Stokes. On the composition and resolution of streams of polarized light from different sources. *Mathematical and Physical Papers*, 3:233–258, 1901.

[72] L. Allen, M. W. Beijersbergen, R. J. C. Spreeuw, and J. P. Woerdman. Orbital angular momentum of light and the transformation of laguerre-gaussian laser modes. *Physical Review A*, 45, 1992.

[73] G. Milione, H. I.Sztul, D. A. Nolan, and R. R. Alfano. Higher-order poincaré sphere, stokes parameters, and the angular momentum of light. *Physical Review Letters*, 107, 2011.

[74] D. Naidoo and et. al. Controlled generation of higher-order poincaré sphere beams from a laser. *Nature Photonics*, 10:327–332, 2016.

[75] R. G. Sabat. Superimposed surface-relief diffraction grating holographic lenses on azo-polymer films. *Optics Express*, 21:8711–8723, 2013.

[76] S. Daniel and et.al. Surface plasmons carry the pancharatnam-berry geometric phase. *Physical Review Letters*, 119(25), 2017.

[77] M.G.Moharam and T.K.Gaylord. Rigorous coupled-wave analysis of planar-grating diffraction. *Journal of the Optical Society of America*, 71(7), 1981.

[78] M.G.Moharam, Eric B.Grann, Drew A.Pommet, and T.K.Gaylord. Formulation for stable and efficient implementation of the rigorous coupled-wave analysis of binary gratings. *Journal of the Optical Society of America*, 12(5): 1068–1076, 1995.

[79] T.K.Gaylord and M.G.Moharam. Analysis and applications of optical diffraction by gratings. *Journal of the Optical Society of America*, 73(5), 1981.

[80] M.G.Moharam, Drew A.Pommet, Eric B.Grann, and T.K.Gaylord. Stable implementation of the rigorous coupled-wave analysis for surface-relief gratings: enhanced transmittance matrix approach. *Journal of the Optical Society of America*, 12(5):1077–1086, 1995.

[81] J. Vapaavuori and et. al. Submolecular plasticization induced by photons in azobenzene materials. *Journal of the American Chemical Society*, 137: 13510–13517, 2015.

[82] E. Bailey and R. G. Sabat. Surface plasmon bandwidth increase using chirped-pitch linear diffraction gratings. *Optics Express*, 25:6904–6913, 2017.

[83] Thorlabs. Liquid Crystal Tunable Filter - KURIOS-WB1 kernel description, 2006. URL `https://www.thorlabs.com/newgrouppage9.cfm?objectgroup_id=3488`.

[84] B. Schaefer and et. al. Measuring the stokes polarization parameters. *American Journal of Physics*, 75:163–168, 2007.

[85] EdwardCollett, editor. *Polarized Light: Fundamentals and Applications*. CRC Press, 1992. ISBN: 978-0824787295.

Appendix

Appendix A Circular Diffraction Grating Pitch

As seen in Fig. .1,the interference pattern on film, centered at the origin, can be calculated by considering the superposition of the incident and refelcted wave on the film:

$$E_{film} = E_1(y = 0) + E_2(y = 0), \tag{A.1}$$

where E_1 and E_2 are the directly incident and reflected field of the inscription beam respectively.

$$E_1 = E_0 e^{i(\mathbf{k}_1 \cdot \mathbf{r} - \omega t)}, \qquad E_2 = E_0 e^{-i(\mathbf{k}_2 \cdot \mathbf{r} - \omega t)} \tag{A.2}$$

The intensity of the summed field in Eq. A.1 can be calculated using the expression found in Eq. 2.1.30 and the known wavevectors shown in Fig. .1:

$$\begin{aligned} \lambda_I =& \frac{2\pi}{\Delta\mathbf{k} \cdot \mathbf{r}} \\ =& \frac{\lambda_{beam}}{x \sin(2\theta_{cdg}) + y \cos(2\theta_{cdg}) - y}. \end{aligned} \tag{A.3}$$

It can be seen that this is a general equation for which different planes of interference, aside from (y=0) can be used for other pitch inscriptions with variable ellipse dimensions. One can imagine having different conic slices for the dimensions of the grating with constant pitch.

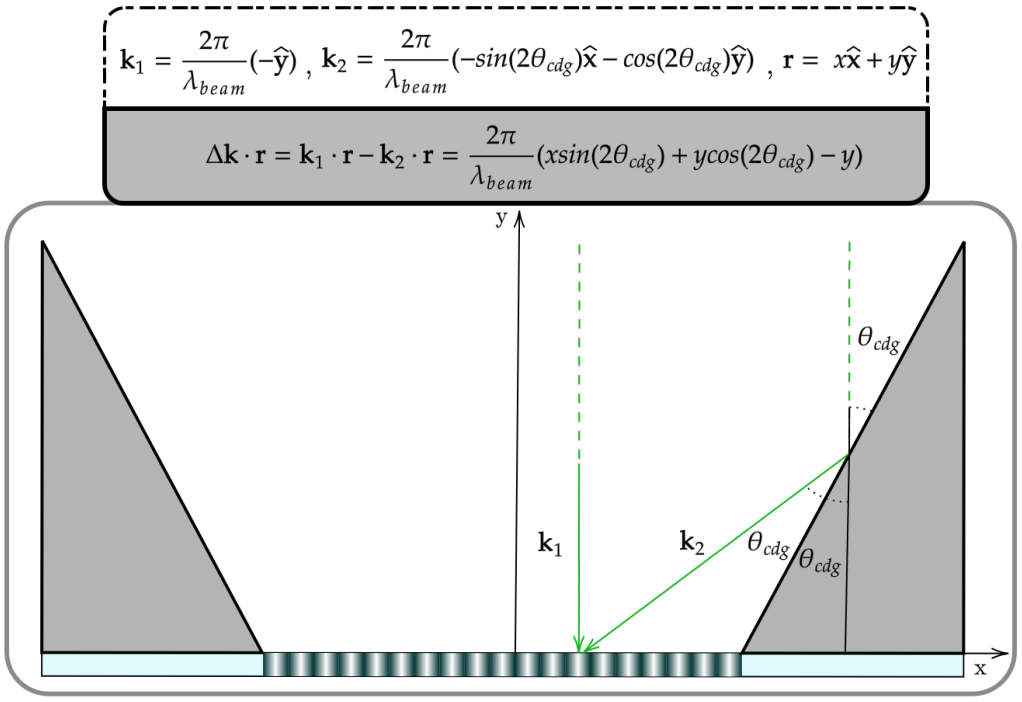

Figure .1: CDG cross section diagram with known beam inscription wavevector

Simply substitutiing (y=0) into Eq. A.3 the known pitch inscription is recovered.

$$\Lambda = \lambda_{beam} \csc 2\theta_{cdg} \tag{A.4}$$

Appendix B Poincaré Sphere/Stokes Vectors Extra

Continued calculation of field dependecies

Note: The following calculation is referenced from two textbooks; Born's Principles of Optics and Collett's Opitcal Engineering: Polarized Light[70][85].

Using Eq. 2.1.49 and Eq. 2.1.48 with substitution of Eq. 2.1.43 and 2.1.44, two new independent equations are formed below with the common sum-angle identities:

$$\begin{aligned} E_{0x'}(\cos\tau\cos\phi_0 - \sin\tau\sin\phi_0) =& E_{0x}(\cos\tau\cos\phi_1 - \sin\tau\sin\phi_1)\cos\psi \\ &+ E_{0y}(\cos\tau\cos\phi_2 - \sin\tau\sin\phi_2)\sin\psi; \\ \pm E_{0y'}(\sin\tau\cos\phi_0 + \cos\tau\sin\phi_0) =& E_{0x}(\cos\tau\cos\phi_1 - \sin\tau\sin\phi_1)\sin\psi \\ &+ E_{0y}(\cos\tau\cos\phi_2 - \sin\tau\sin\phi_2)\cos\psi. \end{aligned}$$

Subsequently substituting $\tau = 0$ and $\tau = \pi/2$ into the preceeding eqautions above give us 4 equations from which relationships between the unknown coefficients of the rotated general ellipse in Eq. 2.1.49:

$$E_{0x'} \cos\phi_0 = E_{0x} \cos\phi_1 \cos\psi + E_{0y} \cos\phi_2 \sin\psi, \tag{B.1}$$
$$E_{0x'} \sin\phi_0 = E_{0x} \sin\phi_1 \cos\psi + E_{0y} \sin\phi_2 \sin\psi, \tag{B.2}$$
$$\pm E_{0y'} \cos\phi_0 = E_{0x} \sin\phi_1 \sin(\psi) - E_{0y} \sin\phi_2 \cos(\psi), \tag{B.3}$$
$$\pm E_{0y'} \sin\phi_0 = -E_{0x} \cos\phi_1 \sin\psi + E_{0y} \cos\phi_2 \cos\psi, \tag{B.4}$$

Squaring and adding Eq. B.1 and Eq. B.2 together we obtain:

$$\begin{aligned} E_{0x'}^2 \cos^2\phi_0 + E_{0x'}^2 \sin^2\phi_0 =& E_{0x}^2 \cos^2\phi_1 \cos^2\psi + E_{0y}^2 \cos^2\phi_2 \sin^2\psi \\ &+ E_{0x}^2 \sin^2\phi_1 \cos^2\psi + E_{0y}^2 \sin^2\phi_2 \sin^2\psi \\ &+ 2E_{0x}E_{0y} \cos\phi_1 \cos\phi_2 \cos\psi \sin\psi \\ &+ 2E_{0x}E_{0y} \sin\phi_1 \sin\phi_2 \cos\psi \sin\psi, \end{aligned}$$

where the equivalency can be compressed further by collecting like terms and using the Pythagorean and angle sum identities,

$$E_{0x'}^2 = E_{0x}^2 \cos^2\psi + E_{0y}^2 \sin^2\psi + 2E_{0x}E_{0y} \cos\psi \sin\psi \cos\phi, \tag{B.5}$$

where ϕ is defined in Eq. 2.1.37. Simlarly, Eq. B.3 and Eq. B.4 can be manipulated in the same manner to produce:

$$E_{0y'}^2 = E_{0x}^2 \sin^2\psi + E_{0y}^2 \cos^2\psi - 2E_{0x}E_{0y} \cos\psi \sin\psi \cos\phi, \tag{B.6}$$

Adding Eq. B.5 and Eq. B.6 together the following relationship is found:

$$E_{0x'}^2 + E_{0y'}^2 = E_{0x}^2 + E_{0y}^2. \tag{B.7}$$

Multiplying Eq. B.1 and Eq. B.3:

$$\begin{aligned} \pm E_{0x'}E_{0y'} \cos^2\phi_0 =& E_{0x}^2 \cos\phi_1 \sin\phi_1 \cos\psi \sin\psi - E_{0y}^2 \cos\phi_2 \sin\phi_2 \cos\psi \sin\psi \\ &+ E_{0x}E_{0y}(\cos\phi_2 \sin\phi_1 \sin^2\psi - \sin\phi_2 \cos\phi_1 \cos^2\psi), \end{aligned}$$

similarly multiplying Eq. B.2 and Eq. B.4:

$$\begin{aligned} \pm E_{0x'}E_{0y'} \sin^2\phi_0 =& E_{0y}^2 \cos\phi_2 \sin\phi_2 \cos\psi \sin\psi - E_{0x}^2 \cos\phi_1 \sin\phi_1 \cos\psi \sin\psi \\ &+ E_{0x}E_{0y}(\cos\phi_2 \sin\phi_1 \cos^2\psi - \sin\phi_2 \cos\phi_1 \sin^2\psi), \end{aligned}$$

and adding these two expressions together and simplyfying we are left with the following expression:

$$\begin{aligned}
\pm E_{0x'}E_{0y'} =& E_{0x}E_{0y}(\cos\phi_2\sin\phi_1 - \sin\phi_2\cos\phi_1) \\
=& E_{0x}E_{0y}\sin(-\phi) \\
\mp E_{0x'}E_{0y'} =& E_{0x}E_{0y}\sin\phi
\end{aligned} \tag{B.8}$$

It can also be seen that the divison of Eq. B.3 by Eq. B.1, and Eq. B.4 by Eq. B.2 gives the following triple equality and the elimination of $E_{0x'}$ and $E_{0y'}$:

$$\begin{aligned}
\frac{E_{0y'}}{E_{0x'}} =& \frac{E_{0x}\sin\phi_1\sin\psi - E_{0y}\sin\phi_2\cos\psi}{E_{0x}\cos\phi_1\cos\psi + E_{0y}\cos\phi_2\sin\psi} = \frac{-E_{0x}\cos\phi_1\sin\psi + E_{0y}\cos\phi_2\cos\psi}{E_{0x}\sin\phi_1\cos\psi + E_{0y}\sin\phi_2\sin\psi} \\
\implies& E_{0x}^2\sin\psi\cos\psi + E_{0x}E_{0y}(\sin\phi_1\sin\phi_2\sin^2\psi + \cos\phi_1\cos\phi_2\sin^2\psi) \\
=& E_{0y}^2\sin\psi\cos\psi + E_{0x}E_{0y}(\sin\phi_1\sin\phi_2\cos^2\psi + \cos\phi_1\cos\phi_2\cos^2\psi) \\
\implies& E_{0x}^2\sin\psi\cos\psi + E_{0x}E_{0y}\cos\phi\sin^2\psi \\
=& E_{0y}^2\sin\psi\cos\psi + E_{0x}E_{0y}\cos\phi\cos^2\psi \\
\implies& (E_{0x}^2 - E_{0y}^2)\sin\psi\cos\psi = E_{0x}E_{0y}\cos\phi(\cos^2\psi - \sin^2\psi) \\
\implies& (E_{0x}^2 - E_{0y}^2)\sin 2\psi = 2E_{0x}E_{0y}\cos\phi\cos 2\psi
\end{aligned} \tag{B.9}$$

It's convenient to introduce a trigonometric substitution:

$$\frac{E_{0y}}{E_{0x}} = \tan\alpha, \qquad 0 \le \alpha \le \frac{\pi}{2}, \tag{B.10}$$

since the right hand side of Eq. B.9 simplifies, using known Trig. identites, to the following,

$$\tan 2\psi = \frac{2E_{0x}E_{0y}}{E_{0x}^2 - E_{0y}^2}\cos\phi = \frac{2\tan\alpha}{1-\tan^2\alpha}\cos\phi = \tan 2\alpha\cos\phi. \tag{B.11}$$

Similarly Eq. B.8 divided by Eq. B.9 and using another convenient Trig. substitution:

$$\mp\frac{E_{0y'}}{E_{0x'}} = \tan\chi, \qquad -\frac{\pi}{4} \le \alpha \le \frac{\pi}{4}, \tag{B.12}$$

the following expression is obtained using more Trig identites:

$$\begin{aligned}
\frac{2E_{0x'}E_{0y'}}{E_{0x'}^2 + E_{0y'}^2} =& \frac{2E_{0x}E_{0y}}{E_{0x}^2 + E_{0y}^2}\sin\phi \\
\implies \frac{2\tan\chi}{1+\tan\chi} =& \frac{2\tan\alpha}{1+\tan\alpha}\sin\phi \\
\implies \sin 2\chi =& \sin 2\alpha\sin\phi.
\end{aligned} \tag{B.13}$$

In summary, it is seen by Eq.'s B.7, B.11, and B.13, if E_{0x}, E_{0y} and ϕ are known with respect to an arbitrary axes then one can determine the orientation and ellipticity of the plane of polarization. Likewise, if $E_{0x'}, E_{0y'}$(amplitude of vertex,co-vertex along the semi-major,minor axes respectively),ψ (the rotation angle away from the reference coordinate axes) are known, then one can calculate the previously mentioned (E_{0x}, E_{0y}, ϕ).

Stokes Parameters and it's relationship with the Poincaré Sphere Transformations

The Stokes parameters completely describe the polarization field of a plane wave.

$$\begin{aligned} S_0 &= E_{0x}^2 + E_{0y}^2 \\ S_1 &= E_{0x}^2 - E_{0y}^2 \\ S_2 &= 2E_{0x}E_{0y}\cos\phi \\ S_3 &= 2E_{0x}E_{0y}\sin\phi \end{aligned} \tag{B.14}$$

S_0 is simply proportional to the total intensity of the field as described by the inner product description $I \propto \langle \mathbf{E} \cdot \mathbf{E} \rangle$, where the field amplitudes can be written effectively as $\mathbf{E} = [E_{0x}, E_{0y}]$, omitting the phase information that would be destroyed in the inner product. S_1 is proportional to the preponderence of horizontal polarization over vertical, S_2 is the preponderance of $+45^o$ polarization over -45^o polarized fields, and lastly S_3 is the preponderance of right-handed circularly polarized light over left-handed circularly polarized light. Where the chirality is determined rotation direction when viewed in the direction of the light source. Moreover, it can be shown that S_0 is dependent on the other parameters with the following relation:

$$S_0^2 = S_1^2 + S_2^2 + S_3^2 \tag{B.15}$$

Explicitly showing this relation with the Pythagorean identity:

$$\begin{aligned} S_0^2 =& E_{0x}^4 + E_{0y}^4 + 2E_{0x}^2E_{0y}^2 \\ S_1^2 + S_2^2 + S_3^2 =& (E_{0x}^4 + E_{0y}^4 - 2E_{0x}^2E_{0y}^2) \\ &+ 4E_{0x}^2E_{0y}^2\cos^2\phi + 4E_{0x}^2E_{0y}^2\sin^2\phi \\ =& (E_{0x}^4 + E_{0y}^4 - 2E_{0x}^2E_{0y}^2) \\ &+ \text{`}4E_{0x}^2E_{0y}^2(\cos^2\phi + \sin^2\phi) \\ =& E_{0x}^4 + E_{0y}^4 + 2E_{0x}^2E_{0y}^2 \end{aligned}$$

Trigonometric substitutions of the stokes parameters can be made as the following:

$$\begin{aligned} S_1 &= S_0 \cos 2\chi \cos 2\psi \\ S_2 &= S_0 \cos 2\chi \sin 2\psi \\ S_3 &= S_0 \sin 2\chi \end{aligned}$$

The equivalence of these relations are shown below:

$$\begin{aligned} S_3 = 2E_{0x}E_{0y}\sin\phi =& (E_{0x}^2 + E_{0y}^2)\sin 2\chi \\ =& S_0 \sin 2\chi, \end{aligned}$$

from the derivation of Eq. B.13. Similarly it can be shown with the derivation of Eq. B.11:

$$\begin{aligned} S_2 = 2E_{0x}E_{0y}\cos\phi =& (E_{0x}^2 - E_{0y}^2)\tan 2\psi \\ =& S_1 \tan 2\psi. \end{aligned}$$

Substituting this into Eq. B.15 along with the relationship of s_3 we get the following:

$$\begin{aligned} S_0^2 =& s_1^2 + (S_1 \tan 2\psi)^2 + (S_0 \sin 2\chi)^2 \\ =& S_1^2(1 + \tan^2 2\psi) + S_0^2 \sin^2 2\chi \\ \implies S_1^2 =& \frac{S_0^2(1 - \sin^2 2\chi)}{1 + \tan^2 2\psi} \\ =& S_0^2 \cos^2 2\chi \cos^2 2\psi \\ \implies S_1 =& S_0 \cos 2\chi \cos 2\psi. \end{aligned}$$

In a similar fashion, by back substituting the new Trig. relationship of S_1, and the known expression of S_3, into the same relationship for S_0, we get the following:

$$\begin{aligned} S_0^2 =& (S_0 \cos 2\chi \cos 2\psi)^2 + S_2^2 + (S_0 \sin 2\chi)^2 \\ S_0^2 =& S_0^2(\cos^2 2\chi \cos^2 2\psi + \sin^2 2\chi) + S_2^2, \\ \implies S_2^2 =& S_0^2(1 - \sin^2 2\chi - \cos^2 2\chi \cos^2 2\psi) \\ =& S_0^2(\cos^2 2\chi - \cos^2 2\chi \cos^2 2\psi) \\ =& S_0^2 \cos^2 2\chi(1 - \cos^2 2\psi) \\ =& S_0^2 \cos^2 2\chi \sin^2 2\psi, \\ \implies S_2 =& S_0 \cos 2\chi \sin 2\psi. \end{aligned}$$

It is important to take note that these auxilliary angles (χ, ψ) are not observables but instead just a mathematical tool to visualize the polarization states with unitary intensity as points on a unit sphere. Stokes first described the paramters

when studying unpolarized light, and were used to describe the degree of polarization. In fact, the equality held for fully polarized planes waves in Eq. B.15 in general is an inequality relationship for partially polarized beams given by:

$$S_0^2 \geq S_1^2 + S_2^2 + S_3^2. \tag{B.16}$$

Appendix B.1 Time-Average of the Polarization Ellipse

The explicit removal of the time dependence of Eq. 2.1.47 was simply of convenience of algebraic manipulation. The replacement of the time dependence in the total field expression leads to the following:

$$\frac{E_x(t)^2}{E_{0x}^2} - 2\frac{E_x(t)}{E_{0x}}\frac{E_y(t)}{E_{0y}}\cos(\phi) + \frac{E_y(t)^2}{E_{0y}^2} = \sin^2(\phi), \tag{B.17}$$

where the amplitudes and phase shift are effectively independent in time when the light is monochromatic.

Taking the time average of this polarization eclipse to be able to predict the observables of the field, the following operator is used:

$$\langle E_i E_j \rangle = \lim_{T\to\infty} \frac{1}{T}\int_0^T E_i(t)E_j^*(t)dt, \qquad i,j = x,y \tag{B.18}$$

where T is the period of the field and $(^*)$ indicating the complex conjugate.

In particular, taking the time averaged operator of Eq. B.17; is equivalent to an observation made for long periods of time with reference to the period of oscillation, shown as the following:

$$4E_{0y}^2\langle E_x(t)^2\rangle + 4E_{0x}^2\langle E_y(t)^2\rangle - 8E_{0x}E_{0y}\langle E_x(t)E_y(t)\rangle\cos(\phi) = (2E_{0x}E_{0y}\sin(\phi))^2 \tag{B.19}$$

The operators are simply calculated with a complex plane wave as shown:

$$\begin{aligned}
\langle E_x^2\rangle &= \lim_{T\to\infty}\frac{1}{T}\int_0^T (E_{0x}Re\{e^{i(kz-\omega t+\phi_1)}\})(E_{0x}Re\{e^{-i(kz-\omega t+\phi_1)}\})dt \\
&= \lim_{T\to\infty}\frac{1}{T}\int_0^T E_{0x}^2\cos^2(kz-\omega t+\phi_1)dt \\
&= \lim_{T\to\infty}\frac{1}{T}\int_0^T E_{0x}^2\Big(\frac{1}{2}+\frac{\cos 2((kz-\omega t+\phi_1))}{2}\Big)dt \\
&= \lim_{T\to\infty}\frac{1}{T}E_{0x}^2\Big(\frac{1}{2}t\Big|_0^T - \frac{1}{4\omega}\sin 2i(kz-\omega t+\phi_1)\Big|_0^T\Big)
\end{aligned} \tag{B.20}$$

Note, since T is presupposed to be the period of the oscillation, the second term cancels out to zero and we're left with the following from Eq. B.20:

$$\langle E_x^2\rangle = \lim_{T\to\infty}\frac{1}{T}\frac{1}{2}E_{0x}^2T = \frac{1}{2}E_{0x}^2, \tag{B.21}$$

and similarly,

$$\langle E_y^2 \rangle = \frac{1}{2} E_{0x}^2. \tag{B.22}$$

The last time-averaged term in Eq. B.19 is given below:

$$\begin{aligned}
E_x(t)E_y(t)^* &= E_{0x}E_{0y} Re\{e^{i(kz-\omega t+\phi_1)}\} Re\{e^{-i(kz-\omega t+\phi_2)}\} \\
&= \frac{1}{4} E_{0x}E_{0y}(e^{i(kz-\omega t+\phi_1)} + e^{-i(kz-\omega t+\phi_1)}) \\
&\times (e^{-i(kz-\omega t+\phi_2)} + e^{i(kz-\omega t+\phi_2)}) \\
&= \frac{1}{4} E_{0x}E_{0y}(e^{i(\phi_2-\phi_1)} + e^{-i(\phi_2-\phi_1)} \\
&+ e^{-i(2(kz-\omega t)+(\phi_1+\phi_2))} + e^{i(2(kz-\omega t)+(\phi_1+\phi_2))}) \\
&= \frac{1}{2} E_{0x}E_{0y}(\cos\phi + \frac{1}{2} e^{-i(2(kz-\omega t)+(\phi_1+\phi_2))} \\
&+ \frac{1}{2} e^{i(2(kz-\omega t)+(\phi_1+\phi_2))})
\end{aligned} \tag{B.23}$$

integrating the expression to find the time-averaged value we get:

$$\langle E_x(t)E_y(t)^* \rangle = \frac{1}{2} E_{0x}E_{0y}\cos\phi, \tag{B.24}$$

and finally substituting these values into Eq. B.19

$$2E_{0x}^2E_{0y}^2 + 2E_{0y}^2E_{0x}^2 - (2E_{0x}E_{0y}\cos\phi)^2 = (2E_{0x}E_{0y}\sin\phi)^2. \tag{B.25}$$

Completing the square, Eq. B.25 is altered by adding and subtracting $E_{0x}^4 + E_{0y}^4$ to the left hand side and factoring to obtain:

$$(E_{0x}^2 + E_{0y}^2)^2 - (E_{0x}^2 - E_{0y}^2)^2 - (2E_{0x}E_{0y}\cos\phi)^2 = (2E_{0x}E_{0y}\sin\phi)^2, \tag{B.26}$$

where Eq. B.26 has recovered Eq. B.15. Specifically the stokes parameters given a plane wave can be written as:

$$S_0 = E_xE_x^* + E_yE_y^* \tag{B.27}$$

$$S_1 = E_xE_x^* - E_yE_y^* \tag{B.28}$$

$$S_2 = E_xE_y^* + E_x^*E_y \tag{B.29}$$

$$S_3 = i(E_xE_y^* - E_x^*E_y) \tag{B.30}$$

A very standard polarization transformation is to shift the phase of the orthogonal field components (E_x, E_y) in opposing directions by a fixed amount, $e^{\pm i\phi_r/2}$, respectively:

$$E_x' = E_x e^{i\frac{\phi_r}{2}}, \qquad E_y' = E_y e^{-i\frac{\phi_r}{2}}. \tag{B.31}$$

A beam with a retarded phase (ϕ_r), is sent through a linear polarizer with a transmission axis rotated an angle θ from the x-axis. Then the beam with field components of Eq. B.31 is transformed by the linear polarizer in the following way:

$$E = E'_x \cos\theta + E'_y \sin\theta \tag{B.32}$$

Calculating the Intensity of the beam passing through the linear polarizer:

$$\begin{aligned}
I(\theta,\phi) =& E \cdot E^* \\
=& E_x E_x^* \cos^2\theta + E_y E_y^* \sin^2\theta + (E_x E_y^* e^{i\phi} + E_x^* E_y e^{-i\phi}) \cos\theta \sin\theta \\
=& \frac{1}{2} E_x E_x^* (1 + \cos 2\theta) + \frac{1}{2} E_y E_y^* (1 - \cos 2\theta) + (E_x E_y^* e^{i\phi} + E_x^* E_y e^{-i\phi}) \sin 2\theta \\
=& \frac{1}{2}((E_x E_x^* + E_y E_y^*) + (E_x E_x^* - E_y E_y^*) \cos 2\theta \\
& + (E_x E_y^* + E_y E_x^*) \cos\phi \sin 2\theta + i(E_x E_y^* - E_y E_x^*) \sin\phi \sin 2\theta),
\end{aligned}$$

The Stokes parameters can easily be substituted into this expression:

$$\frac{1}{2}(S_0 + S_1 \cos 2\theta + S_2 \cos\phi \sin 2\theta + S_3 \sin\phi \sin 2\theta) \tag{B.33}$$

Using the linear polarizer at 3 different angles ($0^o, +45^o, +90^o$) with no retardance ($\phi = 0^o$), and a polarizer angle and retardance of,$\theta = +45^o, \phi = +90^o$, (using a quarter-wave plate) the Stokes parameters can be rewritten in terms of the quantitative Intensity values as shown below:

$$\begin{aligned}
I(0,0) &= \frac{1}{2}(S_0 + S_1), & I(45,0) &= \frac{1}{2}(S_0 + S_2), \\
I(90,0) &= \frac{1}{2}(S_0 - S_1), & I(45,90) &= \frac{1}{2}(S_0 + S_3).
\end{aligned}$$

Solving for the Stokes parameters we find

$$\begin{aligned}
S_0 &= I(0,0) + I(90,0), & S_1 &= I(0,0) - I(90,0), \\
S_2 &= 2I(45,0) - I(0,0) - I(90,0), & S_3 &= 2I(45,90) - I(0,0) - I(90,0).
\end{aligned} \tag{B.34}$$

Appendix C Mueller Matrics and Polarimetry

The Mueller matrix is formed by assuming that under a field transformation, the corresponding transformed stokes vector of the field transformation can be represented as a linear combination of the intial stokes vectors. Specifically, it can be shown with the field transformations: $E_{i,j} \to p_{i,j} E'_{i,j} (0 \le p_{i,j} \le 1), E_{i(+),j(-)} \to$

$e^{\pm i\phi/2}E_{i,j}, E_{i(+),j(-)} \rightarrow E_{i,j}\cos\theta \pm E_{j,i}\sin\theta$ (Linear Polarizer,Compensator,Rotator), that the corresponding mueller matrices are as follows:

$$\bar{\mathbf{M}}_L = \frac{p^2}{2}\begin{bmatrix} 1 & \cos 2\gamma & 0 & 0 \\ \cos 2\gamma & 1 & 0 & 0 \\ 0 & 0 & \sin 2\gamma & 0 \\ 0 & 0 & 0 & \sin 2\gamma \end{bmatrix}; \qquad p_x = p\cos\gamma, p_y = p\sin\gamma, \tag{C.1}$$

$$\bar{\mathbf{M}}_C = \begin{bmatrix} 1 & 0 & 0 & 0 \\ 0 & 1 & 0 & 0 \\ 0 & 0 & \cos\phi & \sin\phi \\ 0 & 0 & -\sin\phi & \cos\phi \end{bmatrix}. \tag{C.2}$$

Where $p_{i,j}$ are attenuation coefficients and ϕ is a simple phase shift. Similar to the Jones rotation matrices in the Jones vector spaces, the Mueller operator space also has a corresponding rotation matrix with an identical transformation algorithm as follows:

$$\bar{\mathbf{M}}'(2\theta) = \bar{\mathbf{M}}_R(-2\theta)\bar{\mathbf{M}}\bar{\mathbf{M}}_R(2\theta). \tag{C.3}$$

Where $\bar{\mathbf{M}}_R(2\theta)$ is the rotation Mueller matrix for a given rotation θ:

$$\bar{\mathbf{M}}_R(2\theta) = \begin{bmatrix} 1 & 0 & 0 & 0 \\ 0 & \cos 2\theta & \sin 2\theta & 0 \\ 0 & -\sin 2\theta & \cos 2\theta & 0 \\ 0 & 0 & 0 & 1 \end{bmatrix} \tag{C.4}$$

This rotation of a Mueller matrix corresponds to the physical rotation of a polarizing element in the beams path. A clever way to measure the polarization of a plane wave in recent years has been to measure the intensity of a beam through a rotating quarter-wave plate ($\phi = \pi/2$) and a horizontal linear polarizer. With Mueller matrices a theoretical stokes vector can be computed via matrix multiplication representing the initial optical setup:

$$\bar{\mathbf{M}}_L(\gamma = 0)\big(\bar{\mathbf{M}}'_{C,\phi=\pi/2}(2\theta)\big) = \bar{\mathbf{M}}_L(\gamma = 0)\big(\bar{\mathbf{M}}_R(-2\theta)\bar{\mathbf{M}}_{C,\phi=\pi/2}\bar{\mathbf{M}}_R(2\theta)\big) \tag{C.5}$$

Transforming Eq. C.5 onto an arbitrary Stokes vector we get the folowing Stokes vector:

$$\frac{1}{2}\begin{bmatrix} 1 & 1 & 0 & 0 \\ 1 & 1 & 0 & 0 \\ 0 & 0 & 0 & 0 \\ 0 & 0 & 0 & 0 \end{bmatrix}\begin{bmatrix} 1 & 0 & 0 & 0 \\ 0 & \cos^2 2\theta & \sin 2\theta\cos 2\theta & -\sin 2\theta \\ 0 & \sin 2\theta\cos 2\theta & \sin^2 2\theta & \cos 2\theta \\ 0 & \sin 2\theta & -\cos 2\theta & 0 \end{bmatrix}\begin{bmatrix} S_0 \\ S_1 \\ S_2 \\ S_3 \end{bmatrix} =$$

$$\frac{1}{2}(S_0 + S_1\cos^2 2\theta + S_2 \sin 2\theta \cos 2\theta - S_3 \sin 2\theta) \begin{bmatrix} 1 \\ 1 \\ 0 \\ 0 \end{bmatrix} \tag{C.6}$$

Importantly, it is seen from Eq. C.6 that the total intensity of the beam through the rotated quarter-wave plate and horizontal linear polarizer is equal to the following:

$$\begin{aligned} I &= \frac{1}{2}(S_0 + S_1\cos^2 2\theta + S_2 \sin 2\theta \cos 2\theta - S_3 \sin 2\theta) \\ &= \frac{1}{2}(S_0 + S_1(\frac{1}{2} + \frac{\cos 4\theta}{2}) + \frac{S_2 \sin 4\theta}{2} - S_3 \sin 2\theta) \\ &= \frac{1}{2}(S_0 + \frac{S_1}{2} - S_3 \sin 2\theta + S_1 \cos 4\theta + \frac{S_2 \sin 4\theta}{2}). \end{aligned} \tag{C.7}$$

Since the stokes components are derived by an observational averaged Intensity, a linear combination of them is also observational. Noticing that we have a truncated fourier series with harmonics of 2θ. Specifically the series is given by the following expression:

$$I(\theta) = \frac{1}{2}(A - B\sin 2\theta + C\cos 4\theta + D\sin 4\theta), \tag{C.8}$$

where the coefficients of the harmonic series given by:

$$A = S_0 + \frac{S_1}{2} \quad B = S_3 \quad C = \frac{S_1}{2} \quad D = \frac{S_2}{2} \tag{C.9}$$

The construction where θ is the rotation of fast axis away from the x-axis. Where the quarter-waveplate is a birefringent material with two paths of propagation and generalizing $\theta = \omega t$, where ω is the angular frequency of the quarter-waveplate. It is easily seen that the coefficients (A, B, C, D) can be recovered from some elementary Fourier analysis. In fact, the coefficients equal the following expressions:

$$\begin{aligned} A &= \frac{1}{\pi}\int_0^{2\pi} I(\theta)d\theta, & B &= -\frac{2}{\pi}\int_0^{2\pi} I(\theta)\sin 2\theta d\theta, \\ C &= \frac{2}{\pi}\int_0^{2\pi} I(\theta)\cos^2 4\theta d\theta, & D &= \frac{2}{\pi}\int_0^{2\pi} I(\theta)\sin^2 4\theta d\theta. \end{aligned} \tag{C.10}$$

Since intensity measurements can only be taken finitely many times it's crucial to make sure that enough data points are collected between $\theta = 0$ and $\theta = 2\pi$. Note that by the Nyquist-Shannon sampling theorem the integrals defining the harmonic coefficients must be represented by a minimum of 8 measurements between the integral bounds. In general the integrals in the set of equations can

be computed by the following measurements:

$$A \approx \frac{2}{N}\sum_{n=1}^{N} I(n\theta_s), \qquad B \approx -\frac{4}{N}\sum_{n=1}^{N} I(n\theta_s)\sin 2n\theta_s$$
$$C \approx \frac{4}{N}\sum_{n=1}^{N} I(n\theta_s)\cos 4n\theta_s, \qquad D \approx \frac{4}{N}\sum_{n=1}^{N} I(n\theta_s)\sin 4n\theta_s \tag{C.11}$$

The sums represent an approximation to the true integral with N measurements with an angular step size of θ_s, where taking multiple measurements reduces the error of the calculated coefficients. Furthermore, and most importantly, the stokes parameters of the incident beam can be calculated by a rearrangement of the set in Eq. C.10:

$$S_0 = A - C, \qquad S_1 = 2C$$
$$S_2 = 2D, \qquad S_3 = B. \tag{C.12}$$

Appendix D Spatial Intensity Profile Code

Below is a sample code showing how to generate arbitrarily snalges linear polarizers for a single and two polarizer system with a circular grating generating an SPR signal at the unitless wavelength in the simulation.

```
------------------------------------------------------------
##packages used in the python libraries##
------------------------------------------------------------
import plotly.io as py
import numpy as np
import plotly.graph_objects as go
from PIL import Image
------------------------------------------------------------
------------------------------------------------------------
##orientation of polarimetry parameters in degrees##
------------------------------------------------------------
deg1=60 #angle from the x-axis in the
counterclockwise direction of the first linear
polarizer#
deg2=90 #angle from the x-axis in the
counterclockwise direction of the second linear
polarizer#
##converting polarizer angle to radians##
```

```
phi1=(np.pi/180)*deg1
phi2=(np.pi/180)*deg2
```

```
dx=2000 # number of iterations for simulation curves#
```

```
##intensity profile function##
```

```
def linear1density(x,a,phi1):
        return (np.sin(np.arctan(a/x)-phi1)**2)
    #normalized intensity profile of the spr field
    with one incident linear polarizer#
def linear2density(x,a,phi1,phi2):
        return (np.sin(np.arctan(a/x)-phi1)*np.sin(np.
    arctan(a/x)-phi2))**2
    #normalized intensity profile of the spr field
    of a circular grating with a cross linear
    polarizer setup#
```

```
##Defining a function to iterate over the parameter
a ('y-axis') ##
```

```
    def contour(x,a,phi):
        x0=np.linspace(-x,x,dx)
        return linear1density(x0,a,phi)
```

```
a0=np.linspace(-1,1,dx) #defining the y-axis scale#
z=[] #defining empty list to add horizontal cross
sections to be added#
```

```
for i in a0:
    z.append(contour(1,i,phi)) #creating the list of
    cross sections#
```

```
#Creating 2D simulation#
```

```
#colour scale setting parameters for the contour
mapping of the intensity profile simulation#
```

```
colorscale = [[0, 'black'], [0.5, 'grey'],[1, 'white']]
```

```
#stitching together the list of horizontal sections (z) and then generating a
```

```
fig = go.Figure(data =
    go.Contour(z=z, x=np.linspace(-1,1,dx),y=np.
    linspace(-1,1,dx),contours_coloring='heatmap',
    line_width=0,colorscale=colorscale,zmin=0,
    zmax=1))
```

```
##enlarging the generated image simulation##
```

```
fig.update_layout( width=round(13.6/13*dx),
height=dx, font=dict(size=40),autosize=False)
```

```
##saving the simluation to a png file##
```

```
py.write_image(fig, '60_Theory.png', format='png')
```

Appendix E Chirped Circular Gratings

The chirped grating setup simply adds an additional focusing lens in series, prior to the CDG. This curves the wavefront and rays hitting the CDG surface are reflected at distinct angles, and specifically creating a non-linear chirped grating pitch dependent on the location of the focal point along the optical axis.

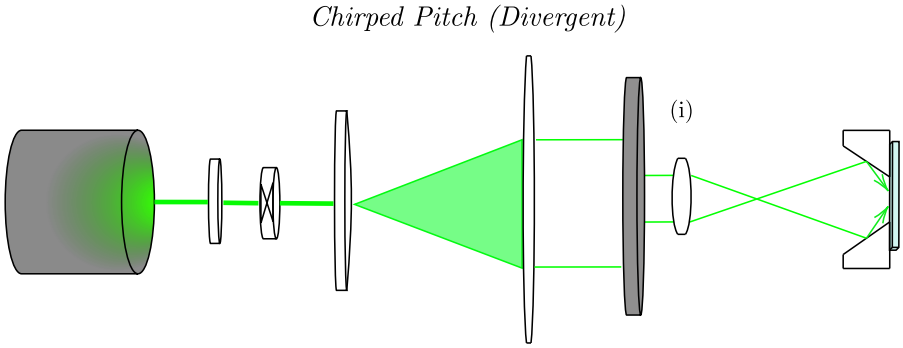

Figure .2: Chirped pitch circular diffraction grating experimental setup (diverging) - (i) Lens where CDG is set after focal point

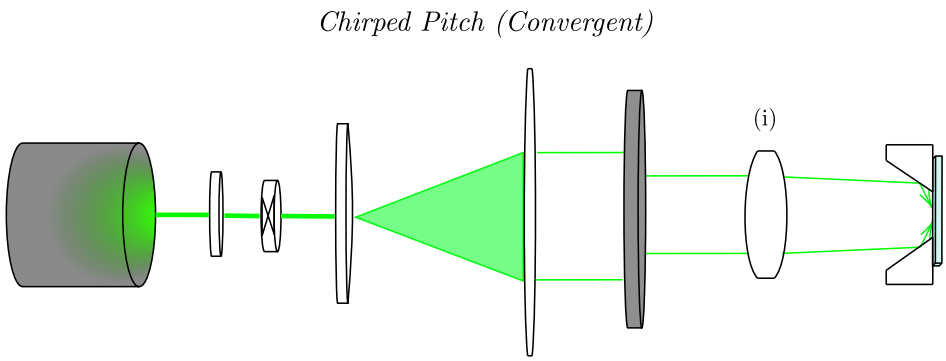

Figure .3: Chirped pitch circular diffraction grating experimental setup (converging) - (i) Lens where CDG is set before focal point

If the focal point is behind the sample (converging) as in Fig. .2, the chirped gratings produced have increasing pitch from the center of the grating(if the CDG has the critical height h_c), to the edge of the grating. Inversely, if the focal point is prior to the sample (diverging) as in Fig. .3, the pitch decreases from the center to the edge of the grating.

Appendix F CDG/AFM Extra

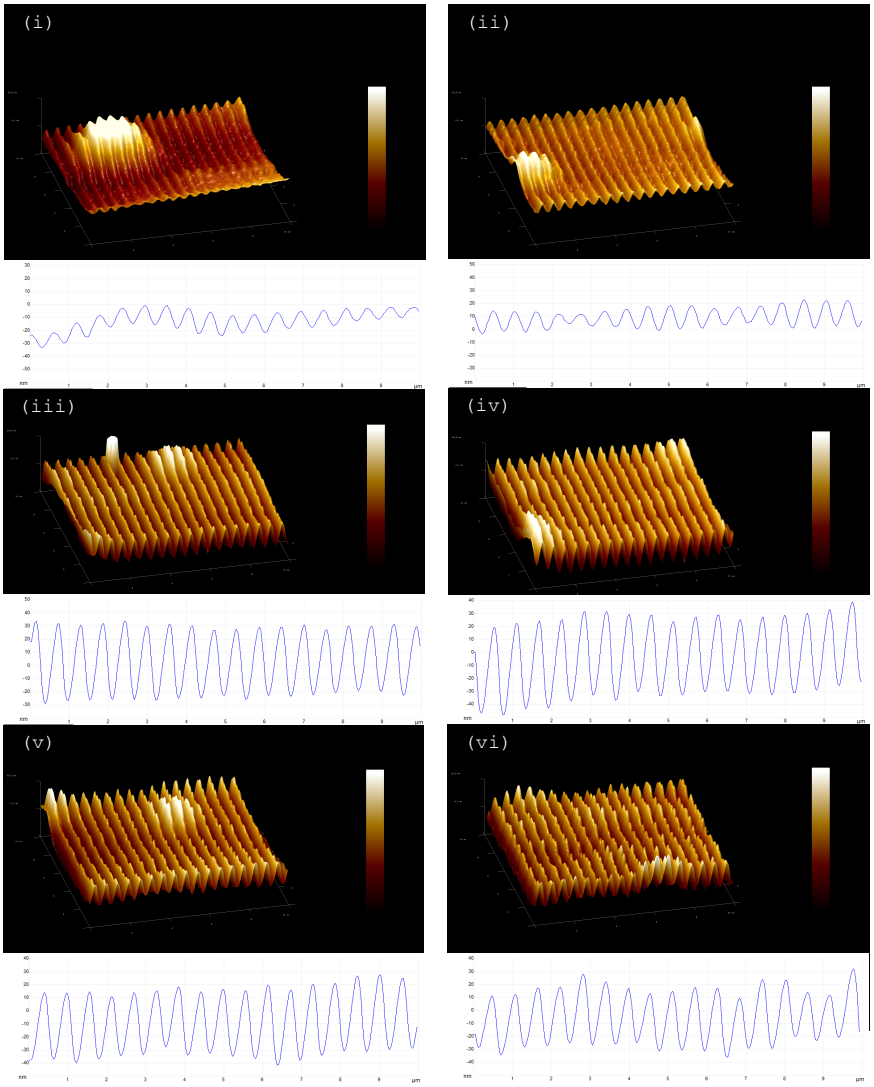

Figure .4: Sequence of AFM surface scans ($10\mu m$x$10\mu m$) of a CG inscribed with 488nm wavelength laser light. The scans were taken along a single ray with inscreasing distances from the center: (i)$2500\mu m$, (ii)$3000\mu m$, (iii)$3500\mu m$, (iv)$4000\mu m$, (v) $4500\mu m$, (vi)$5000\mu m$. Note: All graphs share common colour and axis scales

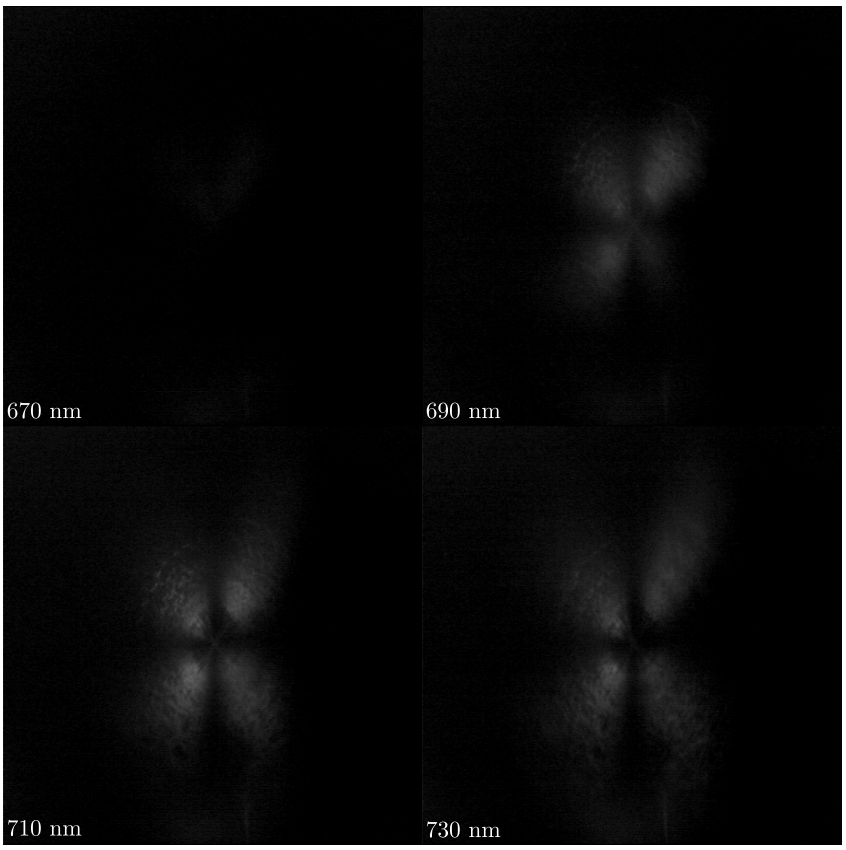

Figure .5: Transmission images of a 668nm pitch CG with varying spectrum wavelength peaks and bandwidths. Wavelength peaks denoted in the bottom left of each image